The System Test of the ZEUS Microvertex Detector: Calibration and Digitisation of the Detector Signals

Diploma Thesis

Institut für Experimentalphysik
Universität Hamburg

Volker Adler

Eichendorffstraße 9
D-21354 Bleckede

Hamburg, February 2002

Abstract

During the shut-down of the electron-proton collider HERA at DESY in Hamburg in the years 2000/2001, the new silicon strip vertex detector MVD has been installed into the ZEUS experiment to achieve a higher quality in the reconstruction of particle tracks. Before its installation, the MVD and all associated hard- and software components have been tested. The objectives of this test – the so-called "system test" – were to investigate the performance of the detector and to check the stability and interplay of all components and the monitoring systems.

In this thesis, the online software to calibrate the detector signals and to store and monitor the calibration parameters has been developed. Furthermore the stability of the calibration parameters over the system test running period has been investigated. In addition, the simulation of the analog detector signals (digitisation) has been worked out, and the simulated signals have been compared with the real detector response.

After a short introduction into the HERA collider and the ZEUS experiment in Chap. 1, the principles of silicon strip detectors are exposed in Chap. 2. Chap. 3 describes the layout of the MVD in detail, and an overview of the data acquisition system is given. Some results of previous measurements on single silicon strip detectors of the MVD obtained with an electron test beam, which are relevant for this thesis, are summarised. The aims and the set-up of the system test are described in Chap. 4. Then results of analyses on the system test data are presented, which have been obtained in parallel to the work of this thesis.

The calibration of the detector signals is described in detail in Chap. 5. After an introduction into the meaning and the calculation of the calibration parameters, the methods to obtain, monitor and store them are explained. Also an analysis is introduced, which studies the stability of the calibration parameters. Overall 98 % of all MVD channels operate reliably. The signal-to-noise ratio is approx. 14.6 for the middle part of the MVD.

The digitisation of the detector signals is described in detail in Chap. 6. The simulation model is introduced and tested with the system test data after customising the signal height. Since the free simulation parameters obtained from the test beam measurements do not describe the data, they are reevaluated from the system test data. The used method is explained, and the simulation is refined by defining a set of new parameters. The new digitisation procedure describes the system test data better for various control distibutions. The simulation reaches a resolution of 26.7 μm in describing a given particle impact position. The simulation model is rather successful, but also some remaining problems are revealed.

Zusammenfassung

Während der Betriebspause des Elektron-Proton-Beschleunigers HERA am DESY in Hamburg in den Jahren 2000/2001 wurde der neue Siliziumstreifen-Vertexdetektor MVD in das ZEUS-Experiment eingebaut, um eine erhöhte Qualität in der Rekonstruktion von Teilchenspuren zu erreichen. Vor seinem Einbau wurde der MVD und alle zugehörigen Hard- und Softwarekomponenten getestet. Dieses Test – der sogenannte „Systemtest“ – waren die Leistung des Detektors und die Stabilität und das Zusammenspiel aller Komponenten und der Überwachungssysteme überprüfen.

Innerhalb dieser Arbeit wurde die Online-Software zur Kalibration der Detektorsignale und zur Speicherung und Überwachung der Kalibrationsparameter entwickelt. Weiterhin wurde die Stabilität der Kalibrationsparameter untersucht. Außerdem wurde die Simulation der analogen Detektorsignale (Digitalisierung) ausgearbeitet, und die simulierten Signale wurden mit der tatsächlichen Detektorausgabe verglichen.

Nach einer kurzen Einführung in den HERA-Beschleuniger und das ZEUS-Experiment in Kap. 1 wird die Funktionsweise von Siliziumstreifendetektoren in Kap. 2 dargelegt. Kap. 3 beschreibt datailliert den Aufbau des MVD, und ein Überblick über das Datenerfassungssystem wird gegeben. Einige Ergebnisse aus vorhergehenden Messungen an an einzelnen Siliziumstreifendetektoren des MVD in einem Elektronen-Teststrahl, die in Beziehung zu dieser Arbeit stehen, werden zusammengefaßt. die Zielsetzung und der Aufbau des Systemtests werden in Kap. 4 beschrieben. Anschließend werden Ergebnisse aus Analysen der Systemtest-Daten vorgestellt, die parallel zu dieser Arbeit gewonnen wurden.

In Kap. 5 wird die Kalibration der Detektorsignale detailliert beschrieben. Nach eine Einführung in die Bedeutung und Berechnung der Kalibrationsparameter werden die Methoden ihrer Gewinnung, Überwachung und Speicherung vorgestellt. Außerdem wird eine Analyse vorgestellt, die die Stabilität der Kalibrationsparameter während der dauer des Systemtests untersucht. Insgesamt 98 % aller MVD-Kanäle erweisen sich dabei als zuverlässig und stabil. Das Signal-Rausch-Verhältnis liegt bei ca. 14.6 für den mittleren Teil des MVD.

Die Digitalisierung der Detektorsignale wird in Kap. 6 im Einzelnen dargestellt. Das Simulationsmodell wird vorgestellt und nach einer Anpassung der Signalhöhe anhand der Systemtest-Daten überprüft. Da die freien Simulationsparameter, die aus den Teststrahlmessungen gewonnen wurden, zur Beschreibung der Systemtest-Daten nicht ausreichen, müssen sie aus den Systemtest-Daten neu gewonnen werde. Die Methode dazu wird vorgestellt und die Simulation durch Definition eines Satzes neuer Parameter weiterentwickelt. Die Beschreibung der Systemtest-Daten wird durch das neue Digitalisierungsverfahren in verschiedenen Kontrollverteilungen verbessert. Die Simulation erreicht eine Auflösung von 26.7 μm in der Beschreibung einer vorgegebenen Position eines Teilchendurchgangs. Damit ist das Simulationsmodell recht erfolgreich, aber einige fortbestehende Probleme werden ebenfalls offen gelegt

Contents

Chapter 1

Introduction

1.1 The ZEUS Experiment

ZEUS is a detector system to observe and analyse collisions of the particle beams at the storage ring HERA[1] at DESY[2] in Hamburg. Fig. 1.1 shows a schematic map of HERA, and Fig. 1.2 shows a sketch of the ZEUS detector.

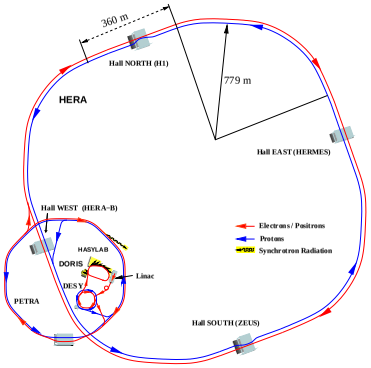

Figure 1.1: **HERA storage ring**
HERA and its pre-accelerator complex. The experiments located at HERA are: H1 (northern hall), HERMES (eastern hall), ZEUS (southern hall), HERA-B (western hall).

In the centre of the ZEUS detector, two beams are brought to collision with a resulting center-of-mass energy[3] of $E_{cms} = 318\,\text{GeV}$. One beam consists of electrons (e^-) resp. positrons (e^+) with an energy of $E_e = 27.5\,\text{GeV}$, the other beam consists of protons (p) with an energy of $E_p = 920\,\text{GeV}$. HERA achieved a maximum luminosity of $20\,\text{mbarn}^{-1}\text{s}^{-1}$ up to now[4]. Inside the inner tracking detectors of ZEUS, the angles of the tracks of the emerging charged particles are measured, and their momenta are

[1] Hadron-Elektron-Ring-Anlage
[2] Deutsches Elektronen-SYnchrotron
[3] All values from [12].
[4] Maximum luminosity in the data taking periods of years 1998-2000, the design value is $15\,\text{mbarn}^{-1}\text{s}^{-1}$.

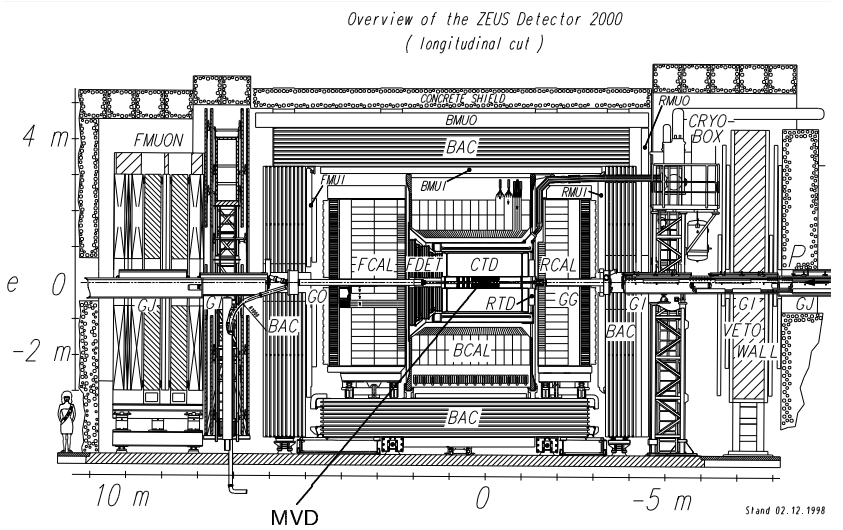

Figure 1.2: **Longitudinal section of the ZEUS detector**
The proton (p) beam enters from the right, the electron (e^-) resp. positron (e^+) beam from the left. Direction specifications (forward, backward) refer to the direction of the p-beam.

computed from the curvature of the tracks in a magnetic field of $B = 1.43\,\text{T}$. In addition, calorimeters measure energies of charged and neutral particles.

The data from the ZEUS experiment is used to do analyses on the following topics:

- measurement of the proton and photon structure,
- studies on the production mechanism of heavy quarks,
- extraction of the coupling constant of the strong interaction α_s and the proton parton densities,
- understanding the phenomenon of diffraction and the production of vector mesons,
- testing of the electro-weak interaction and
- searching for physics beyond the Standard Model.

1.2 Motivation for a Vertex Detector

During the HERA shut-down in 2000/2001, modofications have been made to quintuple the design luminosity of HERA to a value of $70\,\text{mbarn}^{-1}\text{s}^{-1}$. This is achieved with the help of additional focusing magnets close to the interaction point [21]. The increase of the available data leads to a better sensitivity to ep-physics with low cross sections.

Because in many cases it is difficult to distinguish rare events from the dominating background, it is in addition necessary to improve the separation of the signal from the background. A higher quality in e.g. track reconstruction allows to suppress background events more efficiently, and to measure the signal with increased accuracy. The possibility to identify secondary vertices close to the interaction point is most important. This kind of vertices is due to e.g. events with long living particles like mesons containing heavy quarks. In many cases, the possibility to answer a lot of physical questions made accessible by the increase of luminosity only can be exploited with the ZEUS detector upgraded by a vertex detector.

Especially the following fields of research (among others) are significantly improved by the Microvertex Detector (MVD) [23]:

- identification and cross section measurements of mesons containing charm or bottom quarks (secondary vertex!), in both γp-collisions at high energy and deep inelastic scattering (DIS) at large squared momentum transfers (Q^2),
- search for physics beyond the Standard Model, e.g. by:
  - an improved track reconstruction in the forward direction, which leads to a more accurate measurement of the polar angle of the scattered $e^{\pm}$ (This improves the measurement of neutral current events at very high Q^2.),
  - identification of τ-leptons or of mesons containing quarks from the second or third family, which are produced in many models beyond the Standard Model.

Fig. 1.3 gives an example of the expected improvements on purity and efficiency of identifying mesons containing a charm quark in deep inelastic scattering (DIS). With respect to the presently used method, where a D^*-meson is tagged in the central drift chamber, the use of the MVD leads to an increase of the efficiency by about one order of magnitude.

1.3 The Aims of this Thesis

In March 2001, the MVD and associated components have been tested during the "system test". Its objectives were to investigate the stability and the interplay of all detector components and monitoring systems and to check the detector performance. Muons from cosmic radiation produced in the atmosphere are used as traversing particles. Approx. $2.5 \cdot 10^6$ events have been recorded.

Before recording the data from crossing charged particles, the analog signal heights of the MVD sensors have to be calibrated and the noise has to be measured. This is necessary to make "visible" the signals caused by particles. The first main goal of this thesis was to develop a software package, which measures, stores and monitors the calibration parameters. On this basis, an analysis on the stability of the calibration parameters has been performed.

Digitisation is a step of the Monte Carlo simulation of a detector. It simulates the analog signals of a detector component responding to a crossing particle with certain impact parameters. The second main goal of this thesis was to test and to refine an existing digitisation model using the data obtained during the system test as a reference.

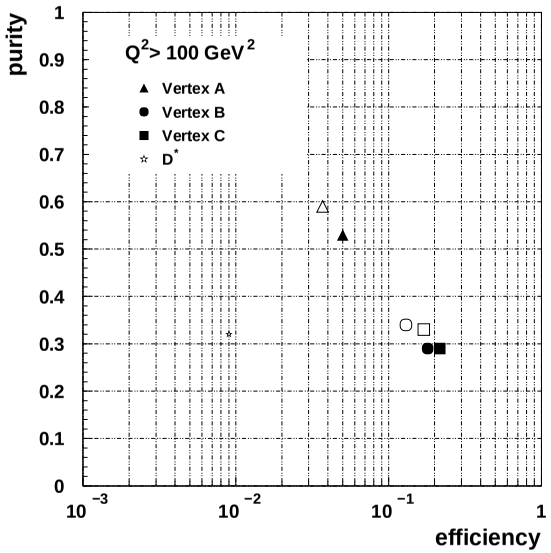

Figure 1.3: **Expected purity vs. efficiency to identify charm** [23]
Purity as a function of efficiency for different possible future MVD selection criteria for charm in DIS with $Q^2 > 100\,\mathrm{GeV}^2$.
Full points show the results from a baseline configuration, open points show the results obtained using only the barrel part of the MVD. Also the efficiency and purity obtained with the present method (tagging of D^*-mesons in the central drift chamber) are shown for $Q^2 > 100\,\mathrm{GeV}^2$.

Chapter 2

Principles of Silicon Strip Detectors

Silicon (semiconductor) detectors can be regarded as solid state ionisation chambers, which measure the total charge of free charge carriers generated e.g. by a traversing particle in the electric field zone of the detector and collected at the electrodes. The electric properties of silicon, which are important for the understanding of the functionality of detectors, are described in section 2.1. The purity of the signal increases with a decreasing number of free charge carriers, which are created without a traversing particle. Therefore, it is advantageous to deplete the detectors by applying a bias voltage, which is described in section 2.2.1. The behaviour of the generated charges is treated in the sections 2.2.2ff.

2.1 The Electric Properties of Silicon

2.1.1 Some Basic Facts

Silicon (Si) is a solid semiconductor with a diamond-like lattice structure. The Si-atoms are surrounded by four equidistant nearest neighbours arranged in a tetrahedral shape. Each of the four valence electrons forms a covalent bond to a valence electron of one of the nearest neighbours. The electric properties of Si are described very well within the band theory [22, Chap. 1]. For Si the width of the band gap E_g, which is the energy difference between the top of the valence band E_V and the bottom of the conduction band E_C, amounts to

$$E_g = E_C - E_V = 1.12\,\text{eV}. \tag{2.1}$$

This value is valid for high-purity material at room temperature and in normal atmosphere. For highly doped material[1], the band gap becomes smaller.

At a temperature of $T = 0\,\text{K}$, silicon behaves like an insulator, because all electrons stay in the valence band. But at room temperature ($kT \approx 26\,\text{meV}$, k is the Boltzmann constant) some electrons populate the conduction band and lead to electrical conduction. In the valence band holes remain from the missing electrons, which also can move and cause electrical conduction. This behaviour defines a semiconductor. For insulators the band gap is so large that the probability of lifting electrons from the valence band to the conduction band by thermal energy is very small. Conductors have either overlapping valence and conduction bands or a partially filled conduction band.

For intrinsic Si at $T = 0\,\text{K}$, *all* valence electrons are covalently bonded to a valence electron from one nearest neighbour in the lattice. In this state the purity is 100 %.

[1] v. section 2.1.2

Every electron lifted to the conduction band leaves a hole in the valence band. This leads to an equality between the density of the electrons in the conduction band n_e and thus of the holes in the valence band n_h (charge carrier densities). They are summarised under the common term of the intrinsic charge carrier density n_i:

$$n_e = n_h = n_i. \tag{2.2}$$

A detailed table of the properties of intrinsic Si at $T = 300\,\text{K}$ can be found in Tbl. A.2.

2.1.2 Doping the Silicon

Doping means to replace some of the Si-atoms in the Si-lattice by elements having three (acceptor) resp. five (donor) valence electrons. The doping changes n_h resp. n_e via the following mechanism:
Acceptors have only three valence electrons to form the four covalent bonds to the Si-lattice. The energy level of the missing electron (acceptor level E_A) resides inside the band gap of the Si very close to the valence band. So for electrons of the valence band the probability to populate the acceptor level is high. When an electron moves from the valence band to the acceptor level[2] to form the missing covalent bond of the acceptor atom to the neighbouring Si-atoms, a hole in the valence band of the Si is created. Therefore acceptors cause an increase of n_h.
Donors have five electrons to form the four covalent bonds to the Si-lattice. The energy level of the redundant electron (donor level E_D) resides inside the band gap of the Si very close to the conduction band. So for electrons of the donor level the probability to populate the conduction band is high. When an electron moves from the donor level to the conduction band[3] an additional electron populates the conduction band of the Si. Therefore donors cause an increase of n_e.
Due to the mass action law, in equilibrium the following relation is always valid:

$$n_e n_h = n_i^2. \tag{2.3}$$

The resistivity ρ resp. the conductivity γ of a doped material depends on its charge carrier densities and their drift mobilities $\mu_{e,h}$:

$$\rho = \frac{1}{\gamma} = \frac{1}{e(\mu_e n_e + \mu_h n_h)}, \tag{2.4}$$

where e is the positive elementary charge.

For materials of different concentrations of donors N_D and acceptors N_A (single doping concentrations) the following name conventions are used:

- $N_D \ll N_A$: The material is called p^+-type.
- $N_D < N_A$: The material is called p-type.
- $N_D > N_A$: The material is called n-type.
- $N_D \gg N_A$: The material is called n^+-type.

[2] The e^- is "accepted" from the valence band.
[3] The e^- is "donated" to the conduction band.

For p-type material the holes are majority carriers and the electrons are minority carriers, v.v. for n-type material.

Often used elements for doping Si are phosphor (P) as donor and boron (B) as acceptor. Because the energy level of a P-atom is very close to the conduction band ($E_C - E_D \approx 45\,\mathrm{meV}$), almost all of them are ionised even for low temperatures with $n_e \approx N_D$. Similarly for B the energy level of an atom is very close to the valence band ($E_A - E_V \approx 44\mathrm{meV}$), so that the B-levels are occupied by electrons from the valence band with resulting $n_h \approx N_A$. Fig. 2.1 shows a diagram of the different energy levels used within the band theory.

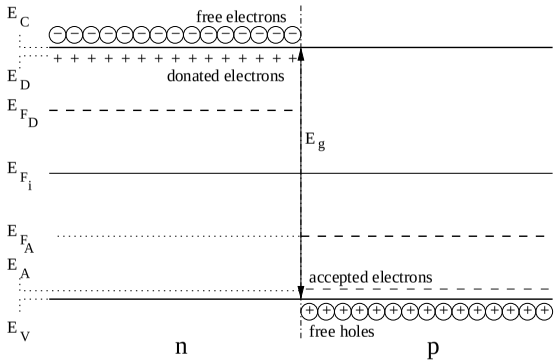

Figure 2.1: **Diagram of energy levels used within the band theory**
The nomenclature follows the one used in the text. The distances between the energy levels are not drawn to scale.

From the single doping concentrations the effective doping concentration N_{eff} can be deduced as

$$N_{eff} = N_D - N_A. \tag{2.5}$$

For p-type material N_{eff} is negative, for n-type material it is positive.

The population of allowed energy states by electrons resp. holes follows from the Fermi-Dirac-statistics with the corresponding distribution function

$$F(E) = \left(1 + \exp\left(\frac{E - E_F}{kT}\right)\right)^{-1}, \tag{2.6}$$

where E_F is the Fermi energy, which is the energy state, that would be half-populated by the electrons. For intrinsic Si at room temperature the Fermi energy is very close to the centre between valence band and conduction band, given by

$$E_{F_i} = \frac{E_C + E_V}{2} + \frac{kT}{2} \cdot \ln\frac{N_V}{N_C} \tag{2.7}$$

with the effective density of states N_V in the valence band resp. N_C in the conduction band. These are related to the charge carrier densities by:

$$n_e = N_C \exp\left(-\frac{E_C - E_F}{kT}\right), \tag{2.8}$$

$$n_h = N_V \exp\left(-\frac{E_F - E_V}{kT}\right), \tag{2.9}$$

$$n_i = \sqrt{N_C N_V} \exp\left(-\frac{E_g}{2kT}\right). \tag{2.10}$$

For n-type Si the Fermi energy is closer to the conduction band:

$$E_{F_n} = E_C - kT \ln\frac{N_C}{N_D}, \tag{2.11}$$
$$n_e \approx N_D;$$

for p-type Si it is closer to the valence band:

$$E_{F_p} = E_V + kT \ln\frac{N_V}{N_A}, \tag{2.12}$$
$$n_h \approx N_A.$$

2.1.3 The p-n-Junction

An abrupt change from n- to p-type material is called a p-n-junction.

When two crystals, one p- and one n-doped, both electrically neutral, in thermal equilibrium and with homogeneously distributed free charge carriers, are brought into contact, free electrons diffuse from the n-region into the p-region and free holes diffuse from the p-region into the n-region to recombine [14, Chap. 3]. This happens, because in the beginning of this process it is more favourable for the electrons to stay in the valence band than in the conduction band. This diffusion creates an excess of negative charge inside the p-region resp. of positive charge inside the n-region, which leads to an electric field, that stops the enhancement of charges by counteraction. Furthermore, the electric field pushes mobile charge carriers away from the boundary region, which becomes a so-called space-charge region (SCR), where mobile charge carriers cannot neutralise the excess of nuclear charges from the doping atoms. The SCR is also known as depletion region. It has the width

$$W = W_n + W_p, \tag{2.13}$$

with the extensions of the SCR into the p- resp. n-type material $W_{p,n}$. Fig. 2.2(a) shows the spatial distributions of charges and charge carriers in a cross section of a p-n-junction. The corresponding electric field is illustrated in Fig. 2.2 (b).

A one dimensional approach can be chosen to understand small depths of the SCR relative to its lateral dimensions within the band theory. On the one hand, at thermal equilibrium the current densities J_e and J_h has to be zero:

$$J_e = J_h = 0. \tag{2.14}$$

On the other hand the current densities depend on the Fermi energy like

$$J_{e,h} = \mp\mu_{e,h} n_{e,h} \frac{dE_F}{dx}, \tag{2.15}$$

which leads together with equation (2.14) to

$$E_F = const. \tag{2.16}$$

within the boundary region. Looking at Fig. 2.1, especially at the location of the Fermi energy relative to E_C and E_{F_i} for the n-region and E_V and E_{F_i} for the p-region, one can deduce that these energy levels cannot stay constant over the SCR. The resulting shifts of E_C and E_V are shown in Fig. 2.2(c).

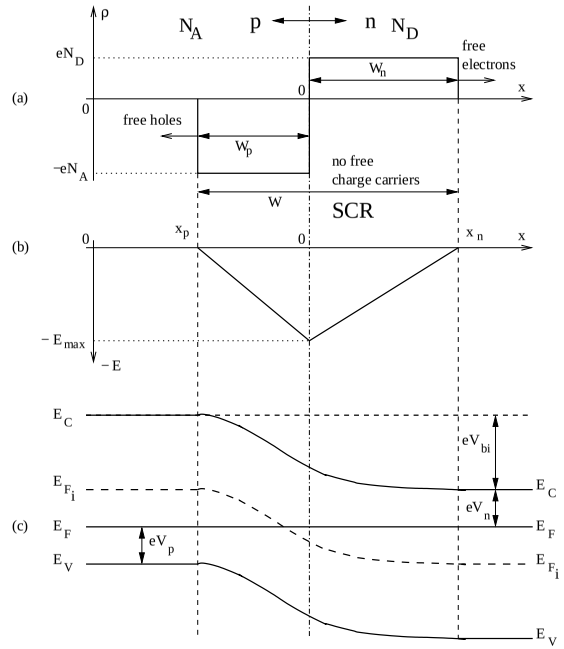

Figure 2.2: **The p-n-junction**
(a) Space-charge distribution $\rho(x)$
The abrupt changes of the space-charge densities are an approximation assuming, that the transition zones are very thin compared with the SCR. This approximation also affects the following calculations of the electric field and the resulting potentials.
(b) Electric field distribution $E(x)$.
(c) Energy band diagram.

These shifts, especially that of E_C, cause a potential between the two undepleted regions, which is called the built-in potential V_{bi}:

$$V_{bi} = \frac{\Delta E_C}{e} = \frac{1}{2} E_{max} W \tag{2.17}$$

$$= \frac{kT}{e} \ln \frac{N_A N_D}{n_i^2}, \tag{2.18}$$

where ΔE_C is the shift of E_C and E_{max} is the maximum of the electric field at $x = 0$. This is

$$\epsilon_0 \epsilon_r E_{max} = eN_A x_p = eN_D x_n, \tag{2.19}$$

with the permittivity in vacuum ϵ_0 and the dielectric constant ϵ_r of Si. The widths of the single parts of the depletion region are

$$W_p = \sqrt{\frac{2\epsilon_0 \epsilon_r}{e} \cdot \frac{N_D}{N_A (N_A + N_D)} V_{bi}}, \tag{2.20}$$

$$W_n = \sqrt{\frac{2\epsilon_0 \epsilon_r}{e} \cdot \frac{N_A}{N_D (N_A + N_D)} V_{bi}}. \tag{2.21}$$

2.2 The Functionality of Silicon Strip Detectors

The operation of a silicon detector is based on the formation of a semiconductor junction. This junction can be a p^+-n-diode from n-doped silicon with a p^+-doped implantation, which is narrow compared with the n-Si. Their connection is a p^+-n-junction with $N_A \gg N_{eff}$, where the donor concentration N_D of the n-material is substituted by a positive N_{eff}, because in this case the doping consists of donors *and* acceptors. In this case the single widths of the depletion region change from equations (2.20) and (2.21) to

$$W_p = \sqrt{\frac{2\epsilon_0 \epsilon_r}{e} \cdot \frac{N_{eff}}{N_A^2} V_{bi}} \approx 0, \tag{2.22}$$

$$W_n = \sqrt{\frac{2\epsilon_0 \epsilon_r}{e} \cdot \frac{1}{N_{eff}} V_{bi}}, \tag{2.23}$$

which leads to

$$W \approx W_n = \sqrt{\frac{2\epsilon_0 \epsilon_r}{eN_{eff}} V_{bi}}. \tag{2.24}$$

The depletion region extends almost completely into the n-material.

2.2.1 Depletion of the Detector Volume

All reflections made so far refer to thermal equilibrium. From this point of view one can call V_{bi} an equilibrium value of voltage [14, section 3.1.2]. In (2.24) one can substitute V_{bi} by a common voltage V as a difference of V_{bi} and additional voltages V_i, which describe different effects occurring in a p-n-diode:

$$W = \sqrt{\frac{2\epsilon_0 \epsilon_r}{eN_{eff}} V}, \text{ with} \tag{2.25}$$

$$V = V_{bi} - \sum_i V_i. \tag{2.26}$$

One additional voltage results from the consideration of the majority carrier density in addition to the donor concentration, which means that the changes of the space-charge density at x_p and x_n in Fig. 2.2(a) are not really abrupt. This is characterised by the Debye length L_D:

$$L_D = \sqrt{\frac{\epsilon_0 \epsilon_r kT}{e^2 N_B}}, \tag{2.27}$$

where N_B represents the local doping concentrations[4]. The resulting correction is:

$$\frac{kT}{e} = L_D^2 \cdot \frac{eN_B}{\epsilon_0 \epsilon_r} \tag{2.28}$$

for each side. But the most important additional voltage in this context is the external bias voltage V_{bias}. The width W is obtained now as

$$W = \sqrt{\frac{2\epsilon_0 \epsilon_r}{eN_{eff}} \left(V_{bi} - V_{bias} - 2\frac{kT}{e} \right)}. \tag{2.29}$$

[4] N_A or N_{eff} in this case, depending on the considered side of the diode.

For a negative value (reverse bias) the depletion region becomes wider, which can finally lead to a full depletion of the n-material, that forms the detector volume. The behaviour of the single charge carriers during this process is described in section 2.2.3. The bias voltage, that is necessary to reach this goal is called depletion voltage V_{depl}:

$$\begin{aligned} V_{depl} &= -\frac{e}{2\epsilon_0\epsilon_r} N_{eff} d^2, \text{ with} \\ |V_{depl}| &\gg V_{bi} \text{ and } |V_{depl}| \gg 2\frac{kT}{e}, \end{aligned} \tag{2.30}$$

where d is the width of the detector volume. Values of voltage contributions measured for the MVD sensors are found in Tbl. B.4.

Depletion does not mean that there are *absolutely* no free charge carriers inside the depleted region. By effects of thermal generation of free charge carriers, which is described in section 2.2.2, and of the non-abrupt changes of space-charge densities in the transition zone, a low current is created. This so-called leakage current I_{leak} is responsible for a part of the noise measured in the detectors[5]. For $V_{bias} \gtrsim V_{depl}$ it stays relatively constant[6], but at some point, where $V_{bias} \gg V_{depl}$, the electric field becomes that high that I_{leak} increases drastically. This effect is called electrical breakdown, and must be avoided to operate a silicon detector safely.

2.2.2 Energy Loss of Traversing Charged Particles by Ionisation

The mean energy loss of charged particles other than electrons in matter by ionisation is given by the Bethe-Bloch formula:

$$-\frac{dE}{dx} = 4\pi N_A r_e^2 m_e c^2 \frac{Z}{A} \cdot \frac{z^2}{\beta^2} \left(\ln \frac{m_e c^2 \beta^2 \gamma^2 E_{max}}{I^2} - \beta^2 - \frac{\delta}{2} - \frac{C}{Z} \right) \tag{2.31}$$

with the Avogadro constant N_A,
the atomic number of the matter Z,
its atomic weight A,
the charge of the traversing particle z, measured in units of e,
its velocity β, measured in units of c,
$\gamma = \frac{1}{\sqrt{1-\beta^2}}$,
the maximum energy transfer in a single collision between the traversing particle and an electron E_{max},
the effective ionisation potential averaged over all electrons I,
a density correction δ,
and a shell correction C.
It is a function of the particle energy

$$E = \gamma M c^2 \tag{2.32}$$

where M is the mass of the traversing particle. At $M \gg m_e$ the approximation

$$E_{max} \approx 2 m_e c^2 \beta^2 \gamma^2 \tag{2.33}$$

is used. The resulting function is shown in Fig. 2.3 for a muon (μ) ($z^2 = 1$) crossing pure Si.

[5] v. section 5.1.3
[6] A typical value for the MVD is specified in Tbl. B.4.

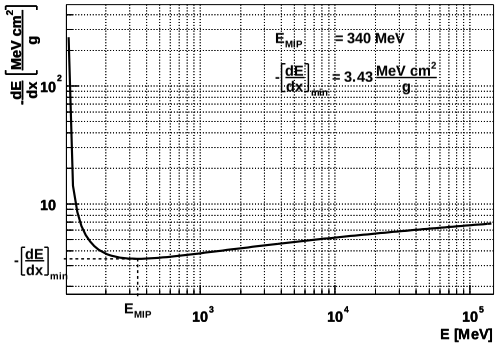

Figure 2.3: **Bethe-Bloch function for a μ traversing pure Si**
Energy loss as a function of the muon energy.
The corrections δ and C are neglected here. The underlying constants described in equation (2.31) are listed in Tbl. A.2.

For low energies the energy loss is inversely proportional to the squared particle velocity, approximately up to the minimum $-\left[\frac{dE}{dx}\right]_{min}$. A particle causing the minimum energy loss E_{MIP} is called a minimum-ionising particle (MIP). This minimum is followed by a relativistic logarithmic rise, which is flattened by the correction term δ. The average energy loss of a particle traversing material of finite thickness can be calculated from equation (2.31) by integration. The statistical fluctuations of this value follow a Gaussian distribution for thick absorbers. For decreasing thickness, the distribution becomes asymmetric. For thin absorbers it becomes a Landau distribution. Only part of the energy loss is used for the creation of electron-hole pairs. Charged particles with high energy with respect to the band gap produce a uniform electron-hole pair distribution within a narrow tube along their path without a significant loss of velocity. The density of the electron-hole pairs is approximately independent of the particle energy and proportional to the square of its charge.

2.2.3 Charge Carrier Transport

Without an external influence, the free charge carriers inside a semiconductor move only driven by their mean thermal kinetic energy $\frac{3}{2}kT$ (diffusion) [14]. In thermal equilibrium the spatial distribution of free charge carriers stays homogeneous.

After an additional local generation of free charge carriers – e.g. by local ionisation – this equilibrium is perturbed. The thermal motion that leads back to equilibrium is called "diffusion".

Another kind of disequilibrium is induced by applying an external electric field, e.g. to deplete the detector. It forces a motion of the free charge carriers into the direction of the electric flux lines. This motion is called "drift". For small fields with resulting changes in drift velocity, which are small with respect to the thermal velocity, a net velocity proportional to the strength of the electric field is obtained:

$$v_{e,h} = \mp \mu_{e,h} E, \tag{2.34}$$

where v is the net velocity, μ is the charge carrier drift mobility[7] of electrons (index e) resp. holes (index h) and E is the electric field strength. The net velocity results from the electrical acceleration superposed by random collisions and thermal motion. For charge carrier energies appreciable larger than their thermal energy, the linearity is not longer valid and a saturation value of velocity is reached.

As in the case of diffusion, the charge carrier drift aspires to reach a new equilibrium, where no net currents flow. For an applied reverse bias voltage this equilibrium is reached after the SCR has become so wide that the resulting electric field sketched in Fig. 2.2(b) compensates the external electric field. Thereby for $V_{bias} > V_{depl}$ the SCR becomes larger than the detector volume, which means that $E(x = d) < 0$ in Fig. 2.2(b). One can extrapolate the electric field to a point $x_n > d$ ($E(x_n) = E(x_p) = 0$ per definition).

A combination of both, local generation of new charge carriers and external electric field, is possible. After perturbing the equilibrium by local generation of (new) free charge carriers in an area, where an external electric field has been applied, the equilibrium is not reconstituted by diffusion, but by drift and afterwards, either by a flowing off of the charge carriers as current, or by weakening of the electric field and recombination of parts of electrons and holes. For flowing off as current, the depleted detector volume behaves like a plate capacitor, what is sketched in Fig. 2.4.

2.2.4 Charge Collection in Silicon Strip Detectors

In silicon strip detectors, the generated charge carriers are not collected on a surface plane of the detector volume, like sketched in Fig. 2.4, but on single strips. This gives information on the position of the charge generation – and thereby on the particle path, like shown in Fig. 2.5.

Caused by diffusion effects in the x-y-plane[8], the generated charge carriers do not only drift to the very next strip, but also to next to next strips and even to strips further apart. One can describe this phenomenon as a "charge cloud", that becomes wider, when it drifts to the strips. This charge cloud is described by a charge distribution in the x- and y-direction, that reaches the detector surface at $z = d$ after drift and diffusion of the generated charge carriers.

For free holes generated in the depth z_0 from the detector surface, from (2.34) one obtains the drift time t [1]:

$$\begin{aligned} t(z_0) &= \int_{z_0}^{d} \frac{dz}{\mu_h E(z)} \\ &= \frac{d^2}{2\mu_h V_{depl}} \cdot ln \frac{V_{bias} + V_{depl}}{V_{bias} - V_{depl}\left(1 - \frac{2z_0}{d}\right)}, \text{ with} \qquad (2.35) \\ E(z) &= \frac{V_{bias} - V_{depl}}{d} + \frac{2V_{depl}}{d^2} \cdot z. \end{aligned}$$

During their drift in the electric field, charge carriers are heated. Their effective

[7] v. Tbl. A.2

[8] The diffusion in z-direction is negligible with respect to the superposition of the dominating net drift in this direction.

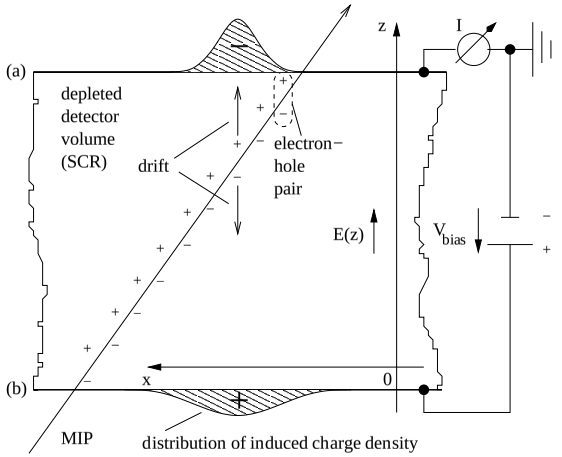

Figure 2.4: **Drift of free charge carriers in a semiconductor under the influence of an electric field**
The detector volume is depleted by the applied $V_{bias} \gtrsim V_{depl}$, causing the electric field $E(z)$.
The traversing MIP generates electron-hole pairs. The electrons drift to the detector plane (b), the holes to the plane (a). Each charge carrier induces an opposite charge density on these planes. Thereby the flowing of this charge onto the planes can be measured as a current. The shape of the distribution of the induced image charge density on a plane depends on the distance between the plane and the free charge carrier in the SCR. The closer to a plane a free charge carrier is located, the narrower the distribution becomes. When the free charge carrier reaches the plane, the image charge density distribution becomes a δ-function. Finally it recombines with the free charge carrier. The integral of the image charge density distribution stays constant and is reversely equal to the charge of the free charge carrier.

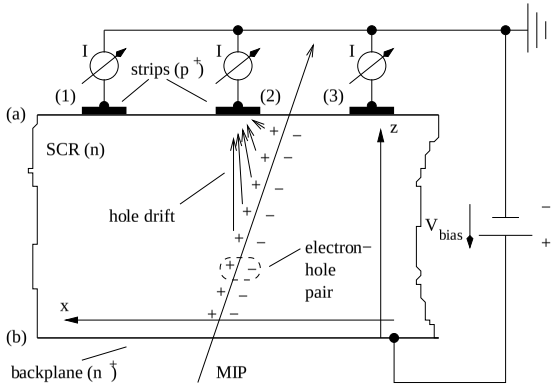

Figure 2.5: **Charge collection in a strip detector**
In this sketch of the principle of the p^+-n-diode coupled with a n^+-backplane, one can see the drift of the holes to the closest strip (2), making possible a position measurement in x-direction.
This sketch illustrates a simplification of the charge carrier motion.

temperature $T(E)$ in weak electric fields[9] is

$$T(E) = \frac{T_0}{2} \cdot \left(1 + \sqrt{1 + \frac{3\pi}{8} \cdot \left(\frac{\mu_h E}{c_{Si}}\right)^2}\right), \tag{2.36}$$

where T_0 is the room temperature, and c_{Si} is the sound speed in Si. This affects the diffusion by a decrease of the drift mobility with increasing temperature:

$$\mu(T(E)) = \mu_0 \sqrt{\frac{T_0}{T(E)}}. \tag{2.37}$$

Finally one obtains a diffusion constant of

$$D(E) = \mu(T(E)) \cdot \frac{kT(E)}{e}, \tag{2.38}$$

with the Boltzmann constant k and the elementary charge e.

The distribution of charge carriers in the x-y-plane $f = f(x, y, t)$ at the time t as a result of diffusion is found by solving the continuity equation

$$\frac{\partial f}{\partial t} = D \cdot \left(\frac{\partial^2 f}{\partial x^2} + \frac{\partial^2 f}{\partial y^2}\right) \tag{2.39}$$

with the initial state

$$f(x = 0, y = 0, t = 0) = \frac{f_0}{d} \cdot \delta(x = 0)\delta(y = 0), \tag{2.40}$$

[9] (2.34) is valid.

where f_0 is the initial charge carrier density at the particle's track and $\delta(x), \delta(y)$ are δ-functions. By solving (2.39) with the requirement (2.40), one finally obtains [1]:

$$f(x, y, t) = \frac{f_0}{2\pi d \cdot l^2(t)} \cdot \exp\left(-\frac{x^2 + y^2}{2 \cdot l^2(t)}\right), \tag{2.41}$$

where

$$l(t) = \sqrt{2 \cdot \int_0^t D(t_1) dt_1} \tag{2.42}$$

has the meaning of the width of a Gaussian distribution of the widths of the charge carrier distributions at the time t with $D(t_1) = D(E(z(t_1)))$. For infinite length of the detector in y-direction, integration of (2.41) over the y-axis gives

$$f(x, t) = \frac{f_0}{\sqrt{2\pi} d \cdot l(t)} \cdot \exp\left(-\frac{x^2}{2 \cdot l^2(t)}\right). \tag{2.43}$$

The diffusion in the x-y-plane described by this charge carrier distribution is superposed by the drift in z-direction. For the distribution at the detector surface $z = d$ of charge carriers generated at the depth z_0 the drift time from (2.35) can be inserted into (2.43).

For a particle crossing the detector under an arbitrary angle θ ($\theta = 0$ means perpendicular crossing) and at an arbitrary position a in x-direction for $z = \frac{d}{2}$, the position of the generation of charge carriers is

$$x_0 = x(z_0, t = 0) = a + \left(z_0 - \frac{d}{2}\right) \cdot \tan\theta. \tag{2.44}$$

If one assumes that all charges, which reach the detector surface, are collected by the closest strip at the position x_{strip}, finally one obtains the amount of collected charges q as an integral over the hole generation depth z_0 and the x-coordinate in the neighbourhood of the strip [1]:

$$q = e \cdot \int_{x_{strip}-p/2}^{x_{strip}+p/2} dx \int_0^d dz_0 \cdot f(x - x_0(z_0), t(z_0)), \tag{2.45}$$

with the strip pitch p.

In general, from a traversing particle one obtains a distribution of signals for several neighbouring strips: the cluster. The shape of the cluster, its width and the total amount of collected charges can be used to calculate the position and the angle of the particle track. Thereby the best possible resolution of the determination increases with a decrease of p [14, section 6.2.3]. If a limitation on the number of signals, which can be read out, and therewith on p is given, additional strips between the readout strips, which are not read out, improve the resolution. Fig. 2.6 shows a sketch of a strip detector with five of such intermediate strips, including a simplified equivalent circuit diagram.

If free charge carriers are generated, the holes drift to one of the strips, the electrons drift to the backplane. During the drift, the charge carriers induce an image charge on the strips via the coupling and the interstrip capacitances, and on the backplane. The correlation of the two signals measured on the readout strips (Fig. 2.6, strips (0) and (6)) can be used to interpolate the impact position of the traversing particle in between. On one hand, the spatial resolution is improved by the better sensitivity of

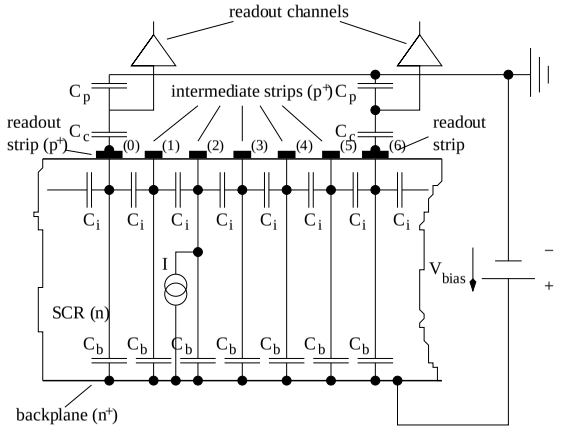

Figure 2.6: **Circuit diagram of a strip detector with five intermediate strips** One can see the formation of the capacitances: interstrip capacitance (C_i), strip-to-backplane capacitance (C_b), charge coupling capacitance (C_c) and preamplifier input capacitance (C_p), with $C_p \gg C_c \gg C_i \gg C_b$. The drifting charge carriers, locally generated by a traversing particle, are symbolised by the current source.

this correlation to impact position variations. On the other hand, a fraction of the signal is lost via the strip-to-backplane capacitances, if the impact position is below an intermediate strip. The absolute number of this fraction depends on layout parameters of the detector, like e.g. number of intermediate strips, strip pitch or readout pitch, and on the internal number of the applied intermediate strip (e.g. strip (2) of five, like in Fig. 2.6).

So it is possible to reach position resolutions, which are much better than the readout strip pitch. Indispensable tools for an optimal hit reconstruction are hit reconstruction algorithms. Some different algorithms for different cluster shapes are introduced in section 3.3.2.

Chapter 3

The ZEUS Microvertex Detector

Besides the available space inside the ZEUS detector, the costs and the time available for the construction, the layout of the MVD primarily is set by the physical goals specified in section 1.2. All these factors lead to the following design specifications [23, section 3]:

- coverage in polar angle: $10° \ldots 170°$,
- at least three spatial measurements, each in two projections,
- intrinsic resolution of each single hit position: $20\,\mu$m,
- resolution of the impact parameter[1]: from the dimension of $100\,\mu$m at 90°, increasing to 1mm at 20°, for momenta $> 2\,$GeV,
- noise fraction[2]: $< 10^{-3}$,
- efficiency of single hit reconstruction: $> 97\%$,
- accuracy in the knowledge of MVD's intrinsic geometry: $20\,\mu$m,
- resolution in separating two tracks: $200\,\mu$m.

3.1 Layout

The MVD is a tracking detector based on the technology of single sided silicon strip detectors, which is described in section 3.1.3.

The MVD's size is predetermined by the space available on the inside of the Central Tracking Detector (CTD). It has a cylindrical shape with a diameter of 319 mm and its length amounts to 2150 mm.

3.1.1 Overview

The MVD is divided into three parts:

1. The forward part[3] (FMVD) consists of four annular detector components (wheels) arranged along and perpendicular to the beam axis. The wheels are positioned at

[1] The impact parameter is the shortest distance between the primary event vertex and a particle track.
[2] The noise fraction is the fraction of pure noise in reconstructed hits.
[3] Forward refers to the direction of the proton beam.

distances of 32, 45, 60 and 75 cm from the nominal interaction point and detect particles in the region of $7.6° < \theta < 22.3°$ from the nominal interaction point. Fig. 3.2(a) shows the schematic layout of a wheel.

2. The barrel part (BMVD) surrounding the interaction point consists of three cylindrical layers (cylinders) of detector components (ladders) arranged parallel to the beam axis. Its length of 622 mm is adapted to the distribution of the z-coordinates of the interaction points. Fig. 3.2(b) shows the arrangement of the ladders within the cylinders.

3. The rear part[4] contains the wiring of the MVD for power, monitoring and readout.

A sketch of the MVD is shown in Fig. 3.1.

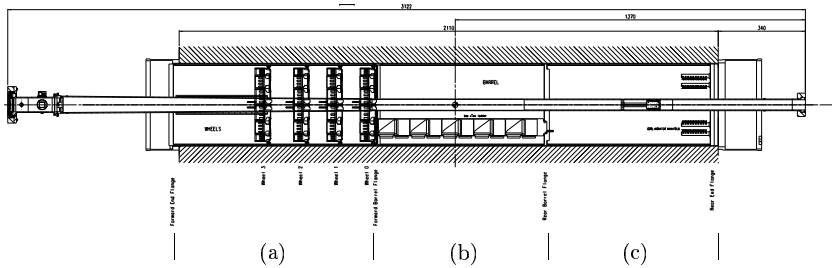

Figure 3.1: **Schematic longitudinal section of the MVD** [13]
Protons enter the detector from the right.
One can see
(a) the FMVD containing the wheels on the left,
(b) the BMVD containing the ladders in the middle and
(c) the rear part of the MVD housing the cables and free from any detector components on the right.
Also the part of the beam pipe housed onthe axis of the MVD can be seen along the horizontal plane in the middle.

Both, wheels and ladders are made of modules. A wheel contains fourteen modules of a trapezoidal shape. The four modules with the same position and numbering within the wheels are called a sector. A ladder consists of five rectangular modules. Though the geometry is different due to the arrangement inside the detector, the principles of construction are the same for both. The location of the FMVD-modules is shown in Fig. 3.2(a). In Fig. 3.3 the modular structure of a ladder can be seen.

In the following, the modules used for the BMVD are described. If not mentioned explicitly, these descriptions are valid for the FMVD-modules also, if one considers the special geometry.

3.1.2 The BMVD-Modules

The module represents the basic detector element of the MVD. One module is the smallest unit of the MVD carrying all components necessary for a complete data taking. In principle, all larger detector elements are nothing else than series of several modules.

[4]Rear refers to the direction of the $e^{\pm}$-beam.

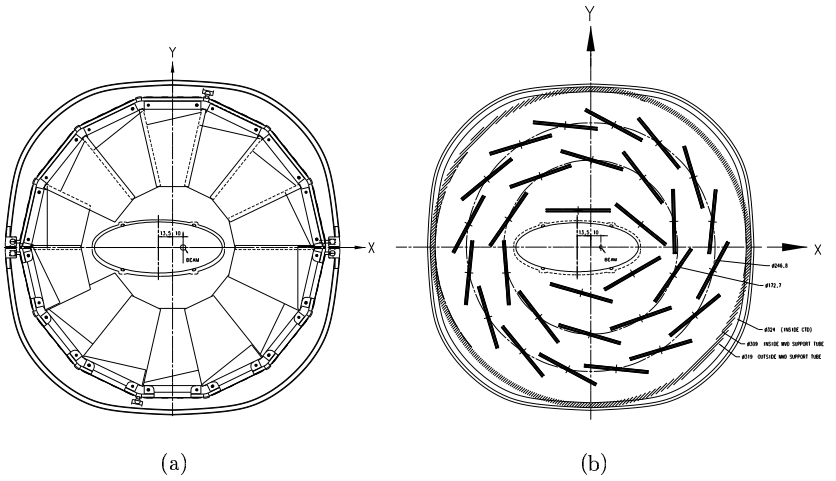

Figure 3.2: **Cross sections of the MVD** [26]
One looks into the backwards directions of the MVD.
(a) Cross section of the FMVD: One can see one of the wheels with segments from the single detector elements (modules) and the beam pipe (elliptical element in the centre) with the interaction point inside.
(b) Cross section of the BMVD: One can see the arrangement of the ladders (thick double lines) and the beam pipe. The cylinders contain (from inner to outer) four, ten and sixteen ladders. The inner cylinder is not complete, because the elliptical beam pipe is not concentric to the beam axis to give synchrotron radiation the possibility to escape without hitting material.

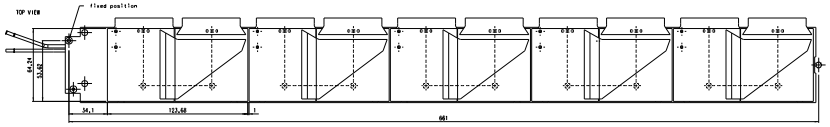

Figure 3.3: **Schematic structure of a ladder** [26]
Side facing the beampipe, the p-beam comes from the left.
The modules are mounted on a support structure. One can see the structure of five modules. The electrical connection from the silicon strips to the readout electronics is shown at the upper side of the ladder. Every module contains two of such connections (one per half-module), which are Kapton®-fanouts.

One module consists of two half-modules, which are glued together. One half-module is composed of two sensors (wheels: only one) and the readout electronics mounted on a so-called hybrid. One of these two sensors is arranged with its strips parallel to the beam directions to determinate the ϕ-coordinate, the other one determines the z-coordinate by strips perpendicular to the beam directions. The r-coordinate is derived from the position of the sensor with regard to the nominal interaction point.

Where the half-modules are glued together, each ϕ-sensor covers a z-sensor or v.v., so together with the known r-coordinate and the position of the module in space a complete determination of the location of a given point defined by one strip of both of the covering sensors is possible.

The readout electronics of one half-module consists of four analog readout chips HELIX128-3.0 with 128 readout channels each, which is described in section 3.1.4. 1024 channels are read out in parallel. This is equal to the number of strips in one module. Because one half-module contains two sensors, one strip of each sensor is read by one channel. This is achieved by an electrical strip-by-strip connection from the ϕ-sensor to the z-sensor via a Kapton®-foil. On the one hand this permits to halve the number of readout channels. On other hand one obtains two possible locations on the module from one signal, the real hit position and a fake hit position (ghost hit) corresponding to the connected strips of the non-hit sensors of the half-modules. The selection of the real hit has to be done by an evaluation algorithm resolving this ambiguity on the bases of all the information in the event, e.g. the track reconstruction. The schematic composition of the module's sensors and the principle of real and ghost hit are shown in Fig. 3.4.

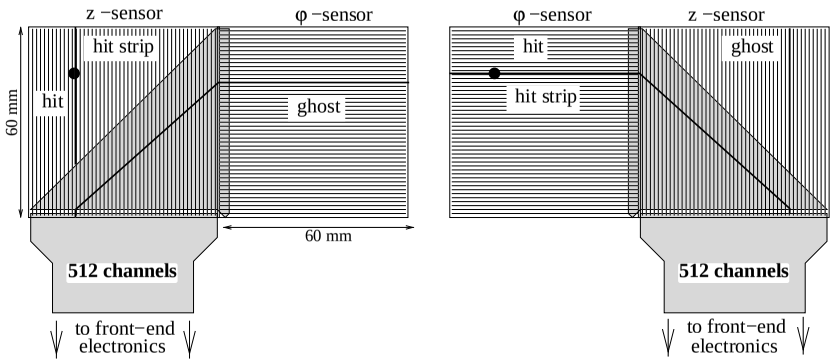

Figure 3.4: **Sensor composition in an BMVD-module**
The figure illustrates the composition of the z- and the ϕ-sensor within a half-module and the position of the sensors of a complete module relative to each other. To form a module, the half-modules are glued together on top of each other.
Two strips – one of each sensor of the half-module – are read out by one readout channel. From the signal one cannot distinguish, which sensor has been hit. So two hit positions are possible. The decision between the two possibilities cannot be made until the particle track is reconstructed.

The wheel-modules do not have this problem, because every readout channel is connected to a single readout strip only. In Fig. 3.5 a FMVD module is sketched.

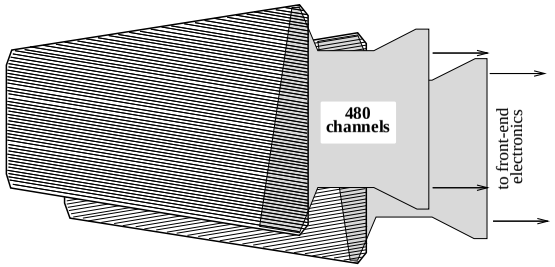

Figure 3.5: **Sensor composition in an FMVD-module**
The FMVD-module consists of two trapezoidal sensors only, which are read out by four readout chips. 32 of the 512 available channels are not active, because an FMVD-sensor only contains 480 readout strips.

3.1.3 The Sensors

The MVD sensors are single sided silicon strip detectors made from high-resistance (5 kΩcm) n-Si wafers. They are approx. 330 μm thick, thereof they have an active region of 300 μm A region of 30 μm n^+-Si, supplemented by an Al-coating at the bottom acts as connection to the bulk. The top side is coated by SiO_2. On its surface p^+-Si implantations with a pitch of 20 μm can be found. Each sixth of them is a readout strip with a width of 14 μm, what leads to a readout pitch of 120 μm. The readout of each readout strip works via an Al-strip, which is connected capacitively via thin Si_3N_4- and SiO_2-coatings. Five of six strips are not read out, but operate as intermediate strips to improve the resolution by the effect of charge sharing, which is described in section 3.3.2. Their width amounts to 12 μm. Fig. 3.6 shows a schematic cross section of a sensor.

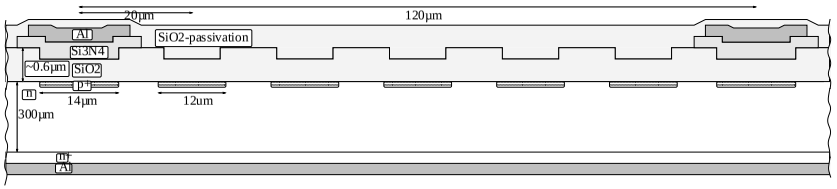

Figure 3.6: **Cross section of an MVD sensor**
One can see a clipping showing two readout strips and the region in between.

Via polysilicon resistors all strips are connected to a bias-ring, which surrounds them. The bias-ring consists of two bias-lines located perpendicular to the strips at their both ends, and of the first and the last strip themselves. Three guard-rings surround the active area. Outside of them on the edge of the sensor a n^+-Si ring allows to contact the backplane from the top. Fig. 3.7 gives an impression of these structures.

As recognizable from Figs. 3.4 and 3.5, the two types of sensors used for the MVD differ in their geometry. The BMVD-sensors are quadratic with a side length of 64.24 mm and an active area of $61.44 \times 62.22\,\mathrm{mm}^2$. The two sensors of a half-module

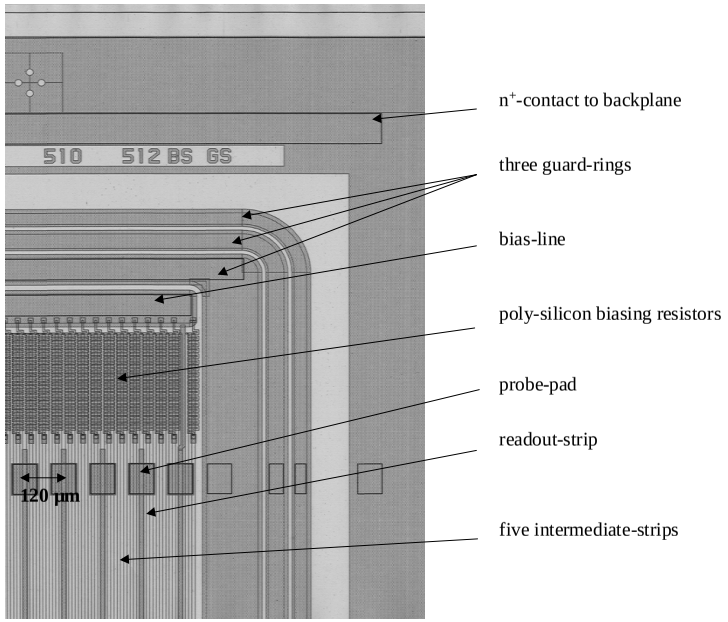

Figure 3.7: **Structures on a BMVD-sensor** [7]
This is a clipping of a corner of a BMVD-sensor including five readout strips.

overlap in a region of 1.26 mm to minimize insensitive (dead) regions. The FMVD-sensors have a trapezoidal shape with strips parallel to one of the tilted sides. So the strips of one module do not cross perpendicularly as in case of the BMVD, but under an angle of 26°. As one can see in Fig. 3.2(a), two types of FMVD-sensors with different lengths exist due to the location of the beampipe. Two neighbouring FMVD-modules overlap to minimize regions with no detector coverage.

3.1.4 The Readout Chip

The HELIX128-3.0 is an analog pipeline-readout chip from the ASIC[5] laboratory in Heidelberg. It integrates 128 readout channels via fast charge sensitive amplifiers and shapers, whose signals are sampled with an external, constant frequency. The measured signal is buffered until either it is read after a trigger signal, or it is overwritten. Because only $\sim 0.1\%$ of all events are expected to be read out, a serial bus is fast enough for the readout. Data taking and readout go on in parallel, what means that the chip is "deadtimeless". For trigger signals following each other closely in time, HELIX128-3.0 is able to store up to eight events in the pipeline, until there is enough time for the serial bus to read them. HELIX128-3.0 can synchronize the data transfer of a group of chips on a single serial output line, using a daisy-chain mechanism. HELIX128-3.0 is

[5] Application Specific Integrated Circuits

additionally equipped with a failsafe token scheme [8], which allows to skip broken chips in a daisy-chain without losing data during the readout. The circuit of one channel of a HELIX128S-2.1, which is conceptional identical to that of version 3.0, is shown in Fig. 3.8. The technical data of HELIX128-3.0 can be found in Tbl. B.5.

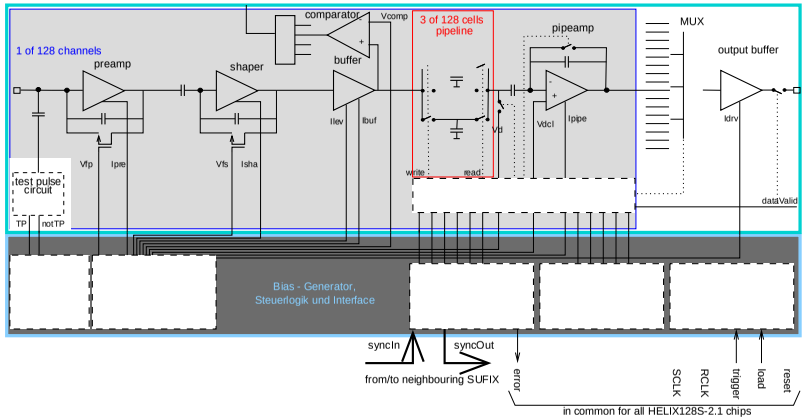

Figure 3.8: **Circuit of one channel of the readout chip HELIX128S-2.1**
This circuit is conceptionally identical to that from version 3.0, which is used for the MVD.
On the left one can identify the structure of the three main elements of the channel: preamplifier, shaper and buffer. In the middle the pipeline is shown including an additional amplifier. On the right one can see the output elements consisting of a multiplexer and the output buffer.
Remark: In analog circuits, buffers do not store data, but amplify signals.

3.2 Data Acquisition

The read out analog signals leave the chips on a hybrid (front-end electronics) via special space saving cables (combo-cable), pass patch-boxes and are sent to further parts of the data acquisition (DAQ) via conventional cables.

analog links amplify the signals and transmit them to the analog-digital-converters (ADC), where they are converted to digital signals, which can be processed by computers. During this process other relevant data like trigger signals or signals indicating errors are combined with the detector signals and added to the data stream, to have a large number of information on every event. Using a fast network (fast Ethernet), all this data are transmitted to the local eventbuilder (EVB) to be written into files, and to DAQ-programs. Essentially, two data streams are used within this submission:

- The EVB data stream contains the information on single strip data. These are the data needed to be recorded for the reconstruction of the event.
- The second-level-trigger (SLT) data stream contains only general information on the clusters. This information is needed for the SLT, where it is processed together with data from the CTD for a first track reconstruction. This information

is sent to the global SLT (GSLT) to come to a trigger decision together with timing information from the calorimeter.

For the analyses described in section 4.3 and in Chaps. 5 and 6, only data from the EVB data stream are used.

Also the trigger signal processing is a real part of the DAQ. For the system test it is described separately in section 4.2.2. A detailed description of processing trigger signals within the ZEUS environment is omitted here. A complete DAQ connection scheme including the Global Tracking Trigger (GTT) is shown in Fig. B.1.

3.3 Test beam Measurements

For the MVD-sensors and half-modules, a test beam program has been set up to characterise the performance of the detectors. The set-up is described in section 3.3.1. Some of the results relevant in the context of this thesis are summarised in sections 3.3.2ff.

3.3.1 Set-up

Fig. 3.9 shows a sketch of the test beam set-up. An e^--beam with an energy of 2 – 6 GeV from the DESY II accelerator is focused onto an optical bench, which carries a detector prototype which is called "device under test" (DUT). The beam defines the z-axis, its position within the x-y-plane is measured by three pairs of reference detectors with a readout pitch of 50 μm and one intermediate strip each. The precision of this position measurement has been measured as 5.4 μm for a e^--beam of 6 GeV. The DUT can be moved laterally, and it can be rotated to measure the effects of different incidence angles of the e^--beam.

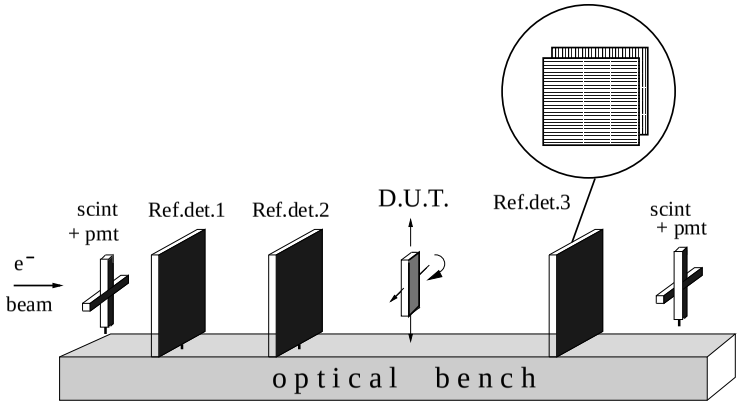

Figure 3.9: **Test beam set-up**

3.3.2 Position Reconstruction

The precision of the position reconstruction of the DUT has been tested for several position reconstruction algorithms under a varying incidence angle. Different models of charge sharing are used for the single algorithms. Charge sharing means that each of two readout strips collects defined fractions of the charge, which is generated in between. Linearity in charge sharing means that the distance of a particle impact between two readout strips to one readout strip is equal to the fraction of charges collected at the other readout strip in units of the readout pitch. The amount of the loss of charge to the sensor bulk does not depend on the impact position.

The tested algorithms are [17]:

- The centre-of-gravity-algorithm:
  All signals S_i of a cluster of the width n read by readout channels with the serial numbers k_i within a sensor are considered to calculate the impact position x_{rec} as:
  $$x_{rec} = p \cdot \frac{\sum_{i=1}^{n} k_i S_i}{\sum_{i=1}^{n} S_i}, \tag{3.1}$$
  where p is the readout pitch. If the charge sharing is linear, this algorithm works well.

- The η-algorithm:
  The highest signal of a cluster and its highest neighbour (S_{left} and S_{right}) are selected to calculate the quantity η by:
  $$\eta = \frac{S_{right}}{S_{right} + S_{left}}. \tag{3.2}$$
  For a linear charge sharing this corresponds to (3.1) with $n = 2$ and $k_1 = 0$. But the measurements show that the distribution of η is not uniform, although the beam profile is uniform over the detector area, as one can observe in Fig. 3.10 [17, Chap. 9].

  These non-linearities can be corrected by the introduction of a probability density function
  $$f(\eta_0) = \frac{1}{N_0} \cdot \int_0^{\eta_0} \frac{dN}{d\eta} d\eta, \tag{3.3}$$
  where $\frac{dN}{d\eta}$ is the parametrised measured distribution function shown in Fig. 3.10, η_0 is the value of η from (3.2) for the considered event and N_0 is the total number of entries in Fig. 3.10. Then the impact position of the particle is given as
  $$x_{rec} = p \cdot f(\eta_0) + x_{left}, \tag{3.4}$$
  where x_{left} is the position of the left strip. Using the η-algorithm, an intrinsic resolution of a single BMVD sensor of $\sigma_{intr} = 7.2 \pm 0.2\,\mu$m is measured for perpendicular incidence. It has been observed that the function $f(\eta)$ describing the non-linear charge sharing depends on where on the sensor the particle hits the strip (y-coordinate) [6]. It is e.g. different on top of the bond pads compared to the rest of a strip. So, this algorithm is hard to use in practice, although its resolution is very precise.

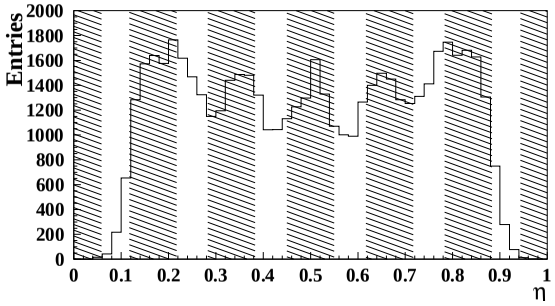

Figure 3.10: **Example of the distribution of η for perpendicular particle impact** [17]
The corresponding distribution of predicted impact positions is uniform.
The striped regions correspond to the area covered by strips.
An enhancement can be observed for values, which correspond to the positions of intermediate strips. Values, which correspond to the positions of readout strips, are suppressed.

- The 3-strip-algorithm:
  Because of a symmetric cross-talk, which is a sensor effect, clusters are wider than two strips in general also for small angles. Therefore using more than two strips can improve the resolution. The highest signal (S_k) and its two neighbouring signals ($S_{k\pm1}$) are used for the 3-strip-algorithm. The two centres of gravity of the highest signal and each of its neighbours $p_{right,left}$ are calculated:

$$p_{right,left} = \frac{kS_k + (k \pm 1)S_{k\pm1}}{S_k + S_{k\pm1}}. \tag{3.5}$$

  The interstrip position $\tilde{p}$ is obtained by

$$\tilde{p} = \mod(p_{rec}, 1), \text{ where } p_{rec} = \frac{p_{left} + p_{right}}{2}. \tag{3.6}$$

  Similar to the η-algorithm, the impact position is given as

$$x_{rec} = p \cdot (f(\tilde{p}) + p_{left}), \tag{3.7}$$

  where $f(\tilde{p})$ is a probability density function. For small angles, the resolution reached by the 3-strip-algorithm is worse than that reached by the η-algorithm, for larger angles the performance of the 3-strip-algorithm is better. But the 3-strip-algorithm is much less sensitive to the effects depending on the y-coordinate than the η-algorithm.

- The head-tail-algorithm:
  For large incidence angles, a cluster becomes wider since the particle crosses several strips. The signal height is distributed almost uniformly over the crossed strips. Variations are dominated by fluctuations in the energy deposition by the traversing particle. So all the information on the impact position is contained in the signals from the edge of the cluster, where the strips are not crossed by the traversing particle, but only "touched". The first (head) and the last (tail) signal of a cluster ($S_{head,tail}$) are selected and the position is calculated as:

$$x_{rec} = \frac{x_{head} + x_{tail}}{2} + p \cdot \frac{S_{tail} - S_{head}}{2\overline{S}}, \tag{3.8}$$

  where $\overline{S}$ is the average signal of all cluster channels.

Fig. 3.11 compares the resolutions of these algorithms as functions of the incidence angle, measured on half-modules.

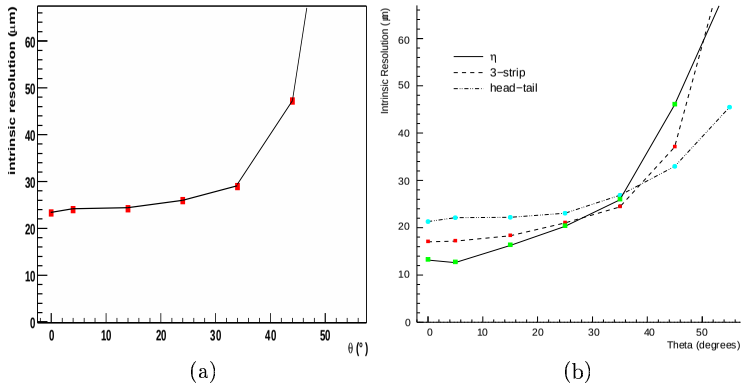

(a) (b)

Figure 3.11: **Angular dependencies of resolutions by different position reconstruction algorithms**
Resolutions as a function of the incidence angle.
Four position reconstruction algorithms are compared for measurements on half-modules:
(a) the centre-of-gravity-algorithm (data kindly provided by E. Carrara), for three strips (highest signal plus neighbours),
(b) the η-algorithm, the 3-strip-algorithm and the head-tail-algorithm [5].

For small angles, the η-algorithm yields the best resolution. For perpendicular incidence, the η- and the 3-strip-algorithm reach the goal of an intrinsic hit resolution of $< 20\,\mu$m. For large angles ($\gtrsim 35°$ in this case), which corresponds to clusters wider than these algorithms consider, the resolution of centre-of-gravity-, η- and 3-strip-algorithm deteriorates drastically. The centre-of-gravity-algorithm yields the worst resolution.

3.3.3 Simulation of Cluster Shapes

The simulation of the cluster shapes aims to reproduce the detailed charge deposition and the corresponding signals at the readout channels caused by a particle crossing the detector. The complete model of this simulation is introduced later[6]. Only a few remarks on the improvements needed to get a good simulation of the test beam data are made here.

[6] v. section 6.1

In a first approximation, the cluster simulation uses a simple model of a strip detector with intermediate strips. It is represented by the equivalent circuit diagram in Fig. 2.6. There only directly neighboured strips are coupled capacitively. Previous measurements have shown that this model oversimplifies and does not describe the position resolution measurements of the test beam well. This is probably due to the fact that it neglects the capacitive coupling of one strip to many other strips in its neighbourhood. In fact a detailed simulation based on PSpice®, where all strips were connected to all others by a capacitance, leads to a much better description of the reconstructed position [16]. Since such a simulation is too time consuming for practical purposes, the simulation of the capacitive charge division is replaced by a parametrisation of the charge sharing obtained from the data. This empirical method is based on transfer coefficients describing the fractions of the charge collected on a strip n, which is transfered to the readout strips. These fractions depend on the distances of the considered readout strips to the strip n. Also symmetric cross-talk is taken into account this way. The transfer coefficient with the ID i is valid for a readout strip with the ID[7] $n \pm i$. An example illustrating the principle how to use the transfer coefficients is shown in Fig. 3.12.

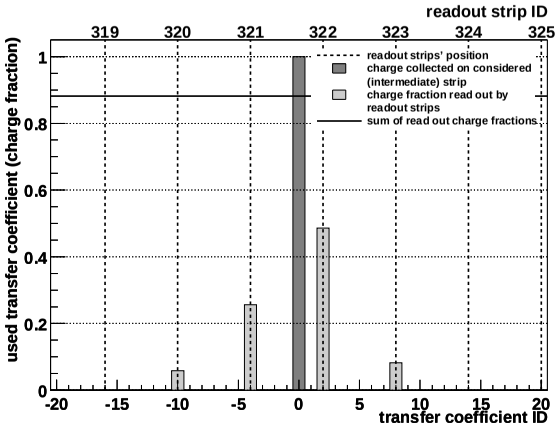

Figure 3.12: **Example of the usage of transfer coefficients**
In this example the total charge is collected on one intermediate strip between the readout strips 321 and 322. The collected charge is normalised to 1. Readout strip 322 has a distance of two strips from the strip collecting the charge. Therefore the transfer coefficient with the ID 2 gives the fraction of the collected charge, which is read at this readout strip. Readout strip 323 has a distance of eight strips from the collecting strip, so the transfer coefficient with ID 8 is used etc. The transfer coefficients are distributed symmetrically, so positive and negative IDs give the same value. The sum of the read out charge is smaller than the collected charge, since a part of the charge is lost to the sensor bulk.
The values of the transfer coefficients used here are taken from Tbl. 3.1.

Tbl. 3.1 lists the transfer coefficients extracted from test beam data [18].

[7] The numbering includes intermediate strips in this scheme.

ID i	transfer coefficient [%]	ID i	transfer coefficient [%]
0	81.0	12	2.1
1	65.5	13	0.0
2	48.6	15	0.0
3	36.3	16	0.0
4	25.6	17	0.0
5	15.8	18	0.0
6	9.0	19	0.0
7	9.0	20	0.0
8	8.2		
9	7.6		
10	5.8		
11	4.1		

Table 3.1: **Transfer coefficients extracted from test beam data** [18]

3.3.4 Further Results

In addition to the results presented in sections 3.3.2f., the following statements are made [17]:

- A hit efficiency of 99.96% is exceeded, which is a very good result.
- The signal-to-noise ratio is $S/N_{testbeam} \approx 21$ for a single BMVD sensor read out via a HELIX128-2.2 readout chip. The noise is distributed uniformly over the strips.
- The variations in gain within individual readout chips are of the order of 2%.

Chapter 4

The MVD System Test

The system test of the MVD has taken place in March 2001 for three weeks in an experimentation hall on the DESY site.

What is called the "system" of the MVD, comprehends several parts. Obviously the main part is the MVD itself as the central (hardware) device. But besides, all the hard- and software of the trigger signal processing and the readout chain (DAQ) and supplying subsystems, like e.g. the cooling or the power supply, belong to the system. So the system test is a test not only of the detector device itself, but of all components, which are added to the ZEUS environment in connection with the MVD.

For the system test, muons (μ) produced by cosmic radiation in the atmosphere are used as traversing particles. At sea level, they carry a mean energy of $\approx 4\,\mathrm{GeV}$ [3, section 4.1]. For this energy, the mean energy loss of the μ in Si amounts to

$$-\frac{dE}{dx} \approx 4.63\,\mathrm{MeV\,cm^2 g^{-1}}$$

without considering the density correction δ. This corresponds to 135 % of the energy loss of a MIP[1]. If the δ is included, this value decreases. Therefore it can be assumed that the behaviour of the μs in the system test does not differ significantly from thus of MIPs.

4.1 Intentions

After tests of single detector elements in parallel to the production, the test beam measurements and the assembly of the MVD and the connected devices, the functioning of the single components, like e.g. the cooling, the DAQ, the power supply etc., and their interplay had to be tested as a stand-alone system before the installation of the MVD into ZEUS could take place. The primary objectives of the system test are:

- testing hard- and software and monitoring systems of
  - slow control (SC),
  - run control (RC),
  - trigger signal processing and
  - data acquisition (DAQ).
- testing the MVD's performance on the basis of

[1] v. Fig. 2.3

  - signal-to-noise ratio (S/N),
  - efficiency,
  - resolution,
  - gain and
  - timing.

4.2 Set-up

For the system test, the MVD has been placed inside a support frame. All connections to power supplies, the cooling and the monitoring and the readout system have been mounted the same way as it has to be done within the ZEUS environment, including the final cables and tubes.

In contrast to the ZEUS environment, an additional trigger system has been installed, which is described in section 4.2.1, and the DAQ has a little different structure due to the fact that it has to work as a stand-alone system here, what is described in section 4.2.2.

4.2.1 Scintillator Trigger

To trigger on the atmospheric μs from cosmic radiation, a trigger system has been installed, which is based on plastic scintillators and a preamplification of the signal by photomultipliers [3]. Two layers of ten scintillators are placed above resp. below the MVD. They are separated by a layer of iron in between to filter other particles[2] than μs with an energy of $> 200\,\mathrm{GeV}$. These two layers (top/down layer) are supplemented by two side panels and two forward panels of scintillators to cover all directions, where μs with reasonable tracks can come from. A cross section of the system test scintillator trigger can be found in Fig. 4.1.

The signals coming from the single scintillators are transmitted to the trigger signal processing part of the DAQ[3].

4.2.2 Data Acquisition

Fig. 4.2 sketches the DAQ connection scheme including the trigger system for the system test.

After a μ has passed one or several scintillators, the scintillator data, which contains the numbering of the activated scintillators, is sent to a NIM logic to verify the signals' coincidence[4]. If another particle than a μ has caused a signal on the top layer of scintillators, no coincidence can be determined, because there is only a signal from one scintillator. It is ensured this way that only μ-events are recorded. But in the case of a coincidence a signal is sent to a next NIM logic, which verifies the coincidence with the clock signal. This is generated as a simulation of the HERA machine clock by the clock and control (C/C) unit. At coincidence, the trigger signal is sent back to the C/C, which gives it to the HELIX driver. Now the trigger signal is sent via the patch-boxes to the HELIX readout chips to start the readout described in section 3.2.

[2] v. section 4.2.2, p. 40, → *coincidence*

[3] v. Fig. 4.2

[4] A typical value for the coincidence window is $\sim 30\,\mathrm{ns}$, used for the bias voltage setting `stable2`

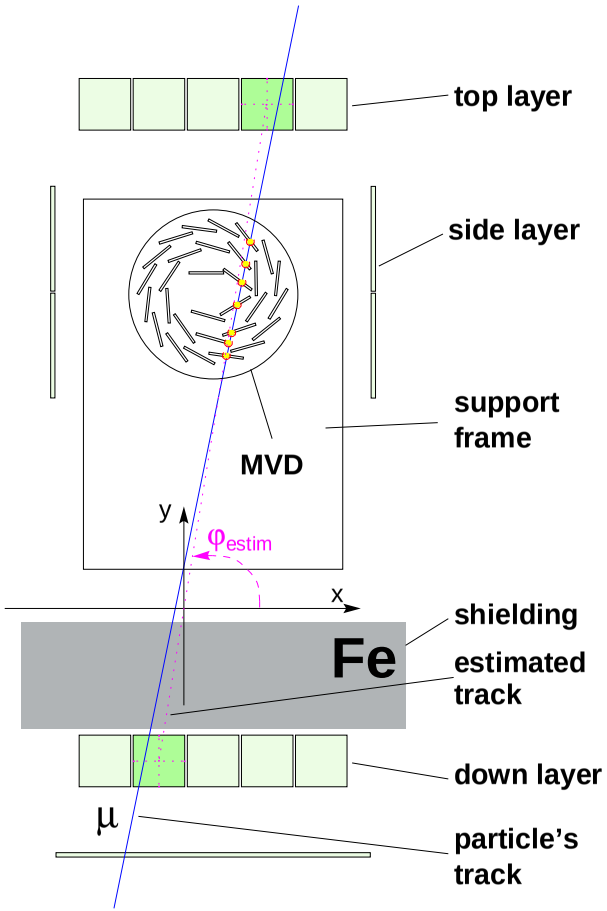

Figure 4.1: **Cross section of the system test scintillator trigger** [3]
This sketch shows the schematic set-up of the scintillator trigger viewed along the proton beam axis. Top, down and side scintillators can be identified, as well as the iron shielding. The forward scintillators are not visible here. Like it is shown for the x-y-plane, the information on the scintillators, which provide the trigger signal, can be used to estimate the particle track coordinates. Thereby the particle track is estimated by the connection line between the centres of the triggering scintillators. The errors of this estimation amount to: $\sim 2°$ in the x-y-plane, and $\sim 9°$ in the x-z-plane.

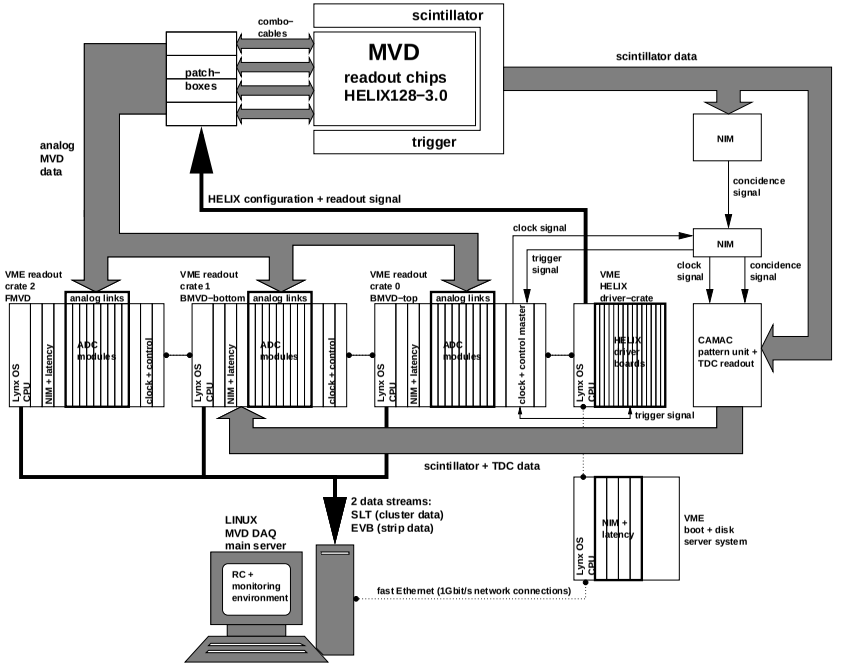

Figure 4.2: **The MVD DAQ connection scheme for the system test**
Both signals from the scintillator trigger and from MVD itself are computed with the DAQ components outlined here.

4.3 Present Results

After some improvements, the subsystems operated by the slow control (SC), like e.g cooling or power supply, performed stable. This was also the case for the DAQ. Only for three modules and one half-module the readout did not work, what corresponds to $\sim 1.7\,\%$ of all MVD-channels. They all belong to the outer cylinder of the BMVD (cylinder 2). These modules can be identified in Tbl. C.1.

In total $\sim 2.5 \cdot 10^6$ events have been recorded.

Some more analyses on the system test data has been performed in parallel to the work at this thesis. Results, which are related to the objectives of this thesis, are summarised in the following.

4.3.1 Efficiency

The analysis of efficiencies needs the particle tracks for the extraction of the required results. This is done by track reconstruction using the underlying geometry of the MVD (track fit) [15].

The efficiency of a sensor is determined as the ratio of the number of reconstructed hits vs. the number of expected hits, where the number of expected hits is the number of tracks crossing the sensor. Fig. 4.3 gives an example of a distribution of this ratio

for the sensors of the BMVD.

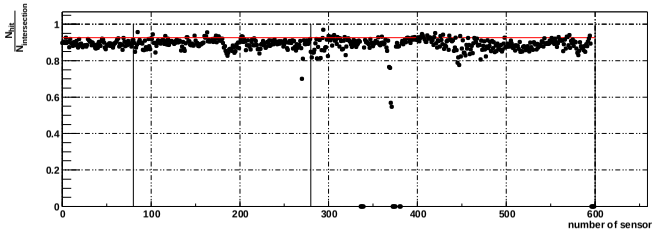

Figure 4.3: **Ratio of reconstructed hits in the BMVD sensors** [24]
Ratio of reconstructed hits vs. expected hits as a function of the serial numbering of the BMVD sensor.
The bright line at $\frac{N_{hit}}{N_{intersection}} = 0.93$ gives the upper limit of the ratio, due to the fraction of active area within a sensor. The sensors with a ratio of zero are switched off.
About 15000 tracks from run 5475 are included.

A mean ratio of $\sim 90\,\%$ has been achieved, including the efficiency of the underlying reconstruction algorithms. The maximum possible ratio amounts to 93 %, corresponding to the fraction of active area in the sensor volume. Since the efficiency is calculated from a fraction of expected hits of 100 %, all values have to be normalised. Therewith the mean ratio leads to a mean efficiency $eff_{BMVD,mean}$ of

$$eff_{BMVD,mean} \approx 97\,\%. \tag{4.1}$$

So the required efficiency of the single hit reconstruction has been achieved roughly. Considering future improvements in the reconstruction algorithms and in the MVD geometry description[5], this is a satisfying result.

4.3.2 Timing and Gain

Timing studies serve the purpose to find the point of time relative to the trigger signal, that gives the highest signal, i.e. the optimum of gain. As described in section 2.2.4, the recorded charge depends on time. One can observe this effect in Fig. 4.4, where the gain as a function of the time distance between simulated HERA clock and trigger signal (TDC time) is shown.

The time points of the best gain in BMVD resp. FMVD differ only by 0.9 ± 0.35 ns. Given the period between interactions at HERA (HERA clock) of 96 ns, this time difference is very small ($\sim 1\,\%$). Therefore it has been verified successfully that the two different detector components have a consistent timing.

The gain describes the relative heights of hit signals in single detector elements. Of course the value of the gain depends on the underlying definition of "signal height". The analysis reported here uses the sum of the signals in a cluster containing the strip with the highest signal and its two neighbours, without consideration of the intrinsic number of recorded channels of a hit. In addition, the highest signal has to exceed a threshold of $5 \cdot \overline{\sigma}$, where $\overline{\sigma}$ is the mean value of the noise of the studied detector part

[5] This result has been obtained without any alignment corrections.

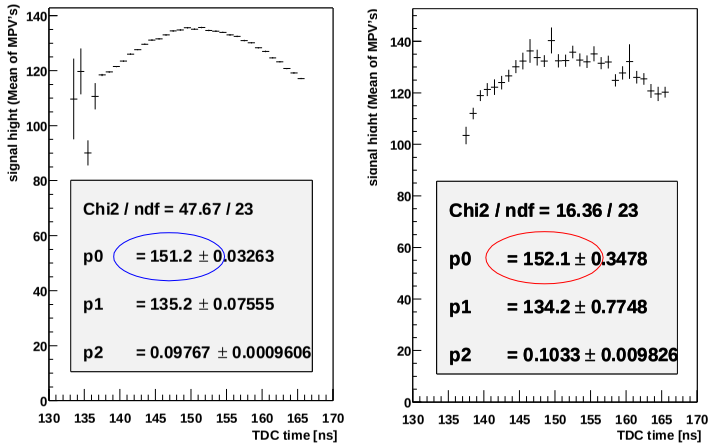

(a) (b)

Figure 4.4: **Timing-dependent gain of BMVD and FMVD** [3, section 7.2.2]
Gain as a function of TDC time for
(a) the BMVD and
(b) the FMVD.
The effect of TDC time dependence in gain is seen clearly.
The distributions are fitted with functions of the form of $y = p_2(x - p_0)^2 + p_1$, with $y_{max} = y(p_0)$.

(BMVD or FMVD). These values are obtained as the means of Gaussian fits to the distributions of the noise values of all single channels belonging to the studied detector part[6]. Since the signal height varies with the incidence angle, all values have been normalised to an estimated value for perpendicular incidence [3, section 7.2.3]. The underlying incidence angles have been extracted from the information on the direction of a particle track yielded from an estimation, which is based on the trigger information, and illustrated in Fig. 4.1. The gain is identified as the most probable value (MPV) of the signal heights Landau distribution for a detector element. For the half-modules of the BMVD, the distribution of gains is shown in Fig. 4.5.

The σ of the Gaussian distribution in Fig. 4.5 (b) (Sigma) amounts to $\sim 3\,\%$ of the mean value (Maximum). Since the distribution is rather narrow, one can state that the gain of the half-modules is quite constant and the signals of the BMVD half-modules are at the same level. An additional important meaning of the gain is its contribution to the calculation of the signal-to-noise ratio, which is carried out in section 5.4.

[6] v. section 5.1.3

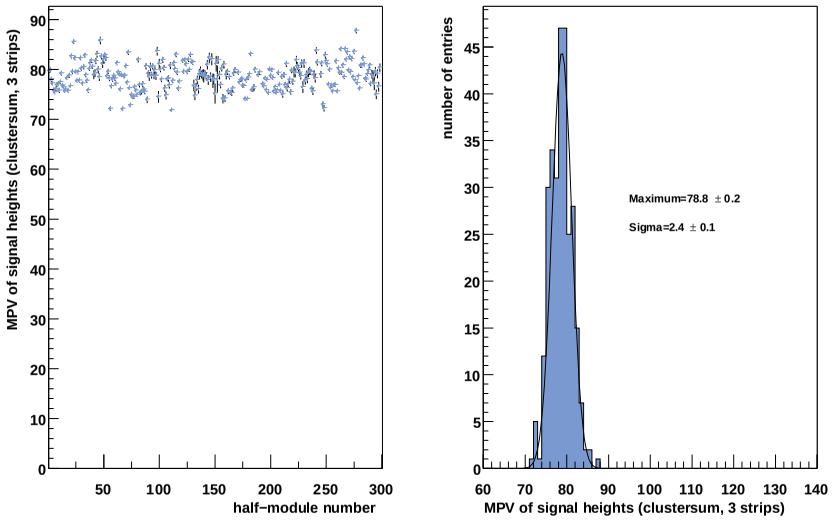

(a) (b)

Figure 4.5: **Gain of BMVD half-modules** [3, section 7.2.4]
(a) MPV of the signal height as a function of the serial number of the half-module inside the BMVD,
(b) distribution of MPV's for the BMVD.
Only hits with an estimated incidence angle of $\leq 45°$ are considered. Half-modules with known problems are skipped.

Chapter 5

Calibration of Detector Signals

The basic calibration of the detector signals is performed using randomly triggered raw signals. In the overwhelming majority of these signals are pure noise signals of the detector and the read-out electronics, i.e. no particles crossed the detector. Raw signals are Gaussian distributed for all channels in one readout chip within one single event, as shown in Fig. 5.1(a)[1]. In general the mean value of the Gaussian distribution is not zero, and it is so wide that signals from particles crossing the detector ("hit signals") usually are hidden inside the distribution, what is demonstrated in Fig. 5.1(b).

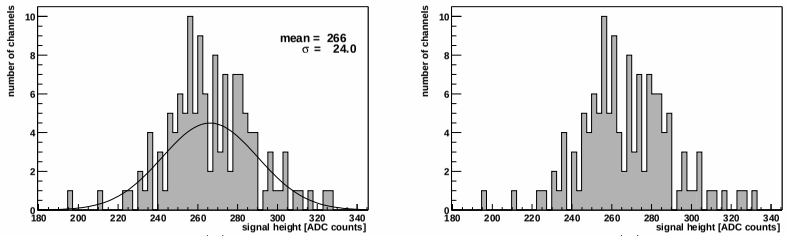

(a) (b)

Figure 5.1: **Raw signal distributions for all channels in one chip and one event:**
(a) containing no hit, fitted with a Gaussian, and
(b) containing one hit.
The signals of the hit strips cannot be identified only from (b) itself. They are hidden inside the distribution.

The same is true for the raw signals of one channel distributed over many events, what is shown in Fig. 5.2.

The widths of the distributions are caused by several disturbing signals, which can be divided into background and noise signals. Signal calibration performs the task to measure these signals and to derive calibration parameters, which make the hit signals "visible".

[1]The Figs. 5.1 - 5.13 are obtained from run 5457 (219 events), C1 L3 M2 H1 X0 CHN57 resp. event 219. (For the numbering scheme: v. section B.1.) The hit is added by hand.

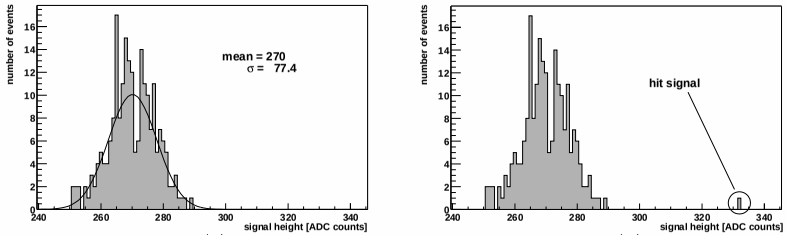

(a) (b)

Figure 5.2: **Raw signal distributions for all events in one channel:**
(a) containing no hit, fitted with a Gaussian, and
(b) containing one hit.
The signal of the hit event can be identified from (b), but its intrinsic height cannot be extracted.

5.1 Parameters of Signal Calibration

Background calibration parameters are subtracted during data taking. Thereby the widths of the signal distributions decrease and their means are set to zero. Noise calibration parameters define the minimum value for a signal to be identified as a hit signals.

One distinguishes between calibration parameters obtained during data taking, and such obtained before the data taking by means of special runs. The latter are stored in files, initialised for event processing before and applied during data taking.

5.1.1 Common Mode

The common mode is a background calibration parameter obtained during data taking. It represents a systematic shift of the raw signals of *all* channels read out by *one* readout chip, and is valid only for *one* event. This means that it has to be computed for *every* event. Thereby the common mode $CM(k)$ represents the average of the raw signals $ADC_i(k)$ of all n_{Chip} operating channels i of one chip within one event k:

$$CM(k) = \frac{\sum_{i=0}^{n_{Chip}} ADC_i(k)}{n_{Chip}}. \tag{5.1}$$

This is illustrated in Fig. 5.3(a).

The common mode of a single chip follows a Gaussian distribution over the events. This distribution and the change of the common mode as a function of the event number are shown in Fig. 5.4.

$CM(k)$ of one chip within event k is subtracted from $ADC_i(k)$ of *all* channels i belonging to this chip. One obtains new signals:

$$CADC_i(k) = ADC_i(k) - CM(k), \tag{5.2}$$

whose average is zero for every event. At the same time, the width of the signals' distribution over many events has decreased for every channel, as shown in Fig. 5.3(b) ($CADC_i(k)$ at $i = const.$).

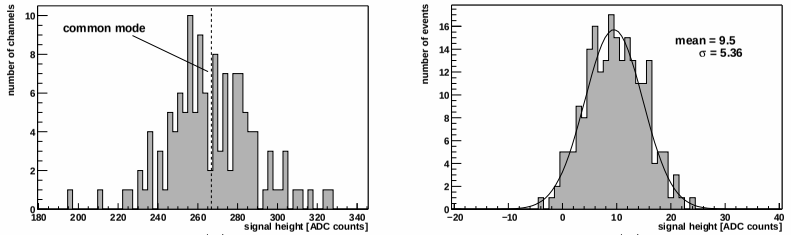

(a) (b)

Figure 5.3: **Calculation of common mode and the effect of its subtraction**
(a) Raw signal distribution for all channels in one chip and one event with resulting common mode, and
(b) signal distribution after common mode subtraction for all events in one channel, fitted with a Gaussian.
The σ of the Gaussian has decreased after common mode subtraction with respect to the distribution in Fig. 5.2(a).

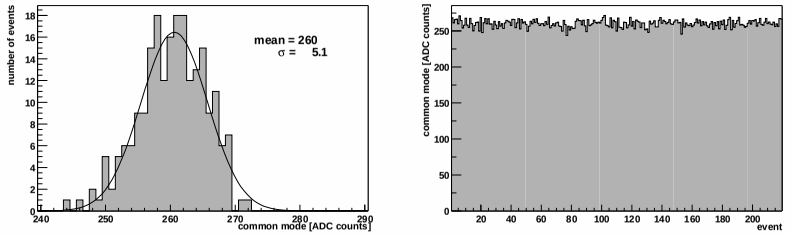

(a) (b)

Figure 5.4: **Common mode for one chip:**
(a) distribution over events, fitted with a Gaussian, and
(b) common mode as a function of the event number.

5.1.2 Pedestal

The pedestal is a background calibration parameter obtained before data taking. It represents a systematic shift of the raw signals of *one* channel, and is valid for *many* events. The pedestal P_i is the average of the signals $CADC_i(k)$ of *one* channel i for N events k:

$$P_i = \frac{\sum_{k=0}^{N} CADC_i(k)}{N}, \tag{5.3}$$

as shown in Fig 5.5(a).

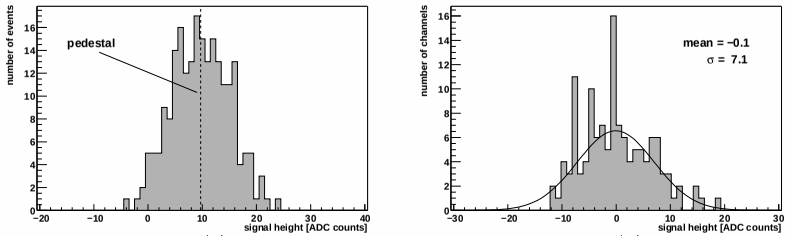

(a) (b)

Figure 5.5: **Calculation of pedestal and the effect of its subtraction**
(a) Signal distribution after common mode subtraction for all events in one channel with resulting pedestal, and
(b) signal distribution after common mode and pedestal subtraction for all channels in one chip and one event, fitted with a Gaussian.
The σ of the Gaussian has decreased after pedestal subtraction with respect to the distribution in Fig. 5.1(a).

The pedestals follow a Gaussian distribution over the channels. This distribution and the change of the pedestal as a function of the channel number are shown in Fig. 5.6.

During data taking, P_i of channel i is subtracted from $CADC_i(k)$ for every event k. One obtains new signals

$$PCADC_i(k) = CADC_i(k) - P_i(k), \tag{5.4}$$

whose average is zero for every channel. At the same time, the width of the signals' distribution over all channels decreases for every event.

Now the goal has been reached to set the mean values of the signal distributions to zero, and to decrease their widths: hit signals can be identified easier.

For the improvement of the signal distributions, it does not make any difference, which of both, common mode or pedestal, is computed and subtracted first. The order as described here corresponds to that used in the MVD DAQ software and was chosen for technical reasons, which are described in section 5.2.4.

5.1.3 Threshold

The threshold is a noise calibration parameter obtained before data taking. It is used to distinguish a hit signal from a pure noise signal. By choosing a specific value,

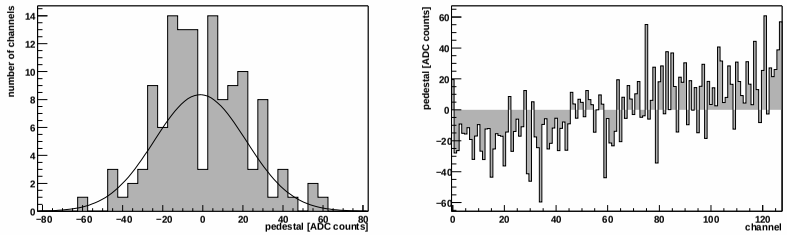

(a) (b)

Figure 5.6: **Pedestal for one chip:**
(a) distribution over all channels, fitted with a Gaussian, and
(b) pedestal as a function of the channel number.
Dependent on the channel number, a bias can be observed in (b). This is a known effect of a drop of the chip bias voltage, which is no problem, because this effect stays constant over time.

the efficiency and purity of the signal reconstruction can be adjusted. The threshold is deduced directly from the channel's noise, which is represented by the σ_i of the Gaussian signal distribution after common mode and pedestal subtraction of channel i:

$$f(PCADC_i(k)) = \frac{1}{\sqrt{2\pi}\sigma_i} \exp\left(-\frac{PCADC_i(k)^2}{2\sigma_i^2}\right). \tag{5.5}$$

This signal distribution together with the evolution of the signals over the events is shown in Fig. 5.7.

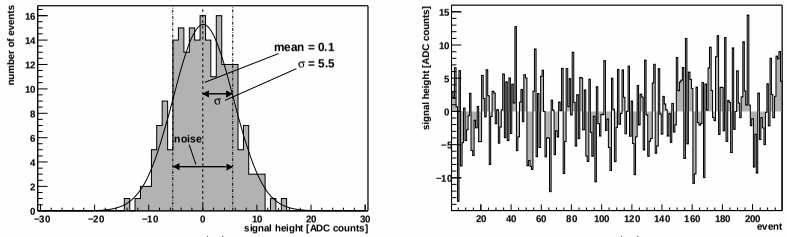

(a) (b)

Figure 5.7: **Signal after subtraction of common mode and pedestal for one channel:**
(a) distribution over all events, fitted with a Gaussian, and
(b) signal as a function of the event number.

The noise is calculated from N events as:

$$\sigma_i = \sqrt{\frac{\sum_{k=0}^{N} PCADC_i(k)^2}{N}}. \tag{5.6}$$

The noise values of one chip are Gaussian distributed. This distribution and the change of the noise as a function of the channel number are shown in Fig. 5.8.

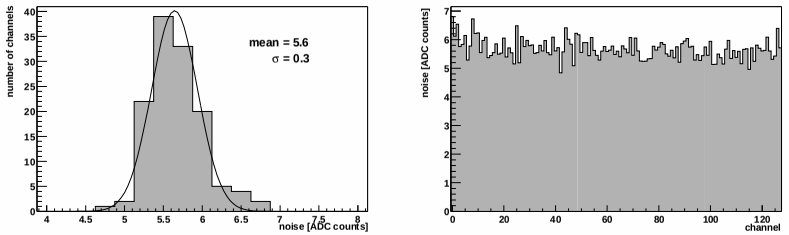

(a) (b)

Figure 5.8: **Noise for one chip:**
(a) distribution over all channels, fitted with a Gaussian, and
(b) noise as a function of the channel number.

If one demands a hit signal to be higher than $1\sigma_i$ only, more than 15% of the non-hit signals due to pure noise are identified as hit signals wrongly. The purity of such a sample would not be high enough, e.g. to identify correctly the track of a particle crossing the detector. To increase the purity, the threshold the hit signal has to exceed, must be higher. Tbl. 5.1 sets examples of thresholds and the corresponding fraction of Gaussian distributed non-hit signals expected above.

Threshold	Fraction of non-hit signals
$PCADC_i(k) \geq 1\sigma_i$	15.87%
$PCADC_i(k) \geq 2\sigma_i$	2.28%
$PCADC_i(k) \geq 3\sigma_i$	0.14%

Table 5.1: **Fractions of Gaussian distributions above a threshold** [2, p.112]

Usually the level of the threshold T_i is given in units of σ_i. So its absolute value is directly proportional to σ_i, which is an individual value for a channel:

$$T_i = sr_{min}\sigma_i \tag{5.7}$$

with the so-called signal-to-noise threshold sr_{min}. If sr_{min} is set to a value, which is too high, smaller hit signals are excluded and therefore the efficiency drops. One can formulate the rule:

> The higher the signal-to-noise threshold, the higher the purity, and the lower the efficiency.

It is important to find a compromise for the best possible relation between a high purity and a high efficiency. For the system test of the MVD, this threshold has been set to [4]:

$$sr_{min} = 2.$$

For an identification of a signal as hit signal,

$$PCADC_i(k) \geq T_i = sr_{min}\sigma_i \tag{5.8}$$

must be fulfilled. Note that there is still a certain probability for misidentifying a signal not caused by a passing particle for a given channel. In practice there are additional

requirements for hit signals. For instance, channels in their neighbourhood are merged to a so-called "cluster". The cluster is required to have a minimum number of channels above threshold or the sum of all signal heights has to exceed a certain value. Since it is very unlikely for random signals to fulfill these requirements, a high purity is ensured. These additional requirements are verified by a cluster algorithm, which is a part of the DAQ system.

Fig. 5.9 sketches the signal distribution of *one* channel for *many* events after common mode subtraction ($CADC_i(k)$ at $i = const.$), containing one hit signal and some misidentified non-hit signals.

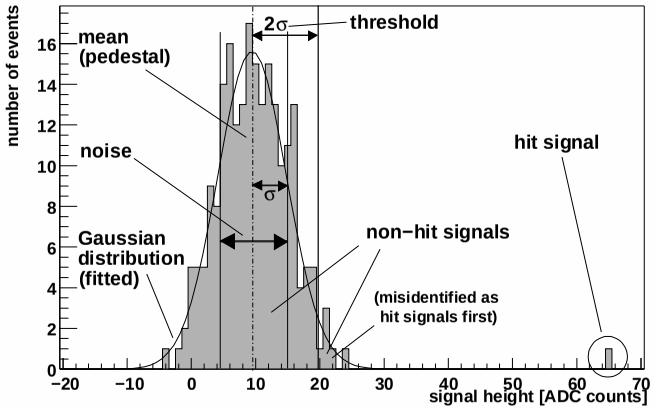

Figure 5.9: **Signal after subtraction of common mode for one channel, containing one hit**
Distribution containing one hit signal, fitted with a Gaussian.
The resulting values of pedestal and threshold, hit signal and misidentified non-hit signals are indicated. Pedestal subtraction shifts the zero of the signal scale to the pedestal.

5.2 Computing of Calibration Parameters

For the MVD a process is needed, which directly computes the calibration parameters from the MVD data and stores them for later use. Four primary tasks are required:

1. reading and interpreting the signal data coming either directly from the online data stream, or from the eventbuilder (EVB) files,

2. computing the calibration parameters,

3. generating online histograms to monitor the calibration parameters,

4. storing the calibration parameters into calibration files.

5.2.1 Reading and Interpreting the Data

In principle, the data structure delivered by the ADC is equal for both, the online data stream and the EVB. Only the type of access differs. The data are organised in events, these are subdivided into tables, which contain 32-bit words. Inside the words the bitwise formation differs depending on the type of the table and the word's position within the table. All tables start with a word giving the size of the table, followed by an identifier, which tells, what kind of data can be found in the table. The intrinsic data follow this header. The scheme of the bitwise formation of the data words containing the signal data is described in Tbl. 5.2.

Bit	Information
0-9	signal height
10-16	channel number within a chip
17-18	chip number within a half-module
19	*free*
20	number of the half-module within a module
21-23	number of the module within a ladder resp. number of he wheel
24-27	number of the ladder within a cylinder resp. number of the module (sector) within a wheel
28-29	number of the cylinder within BMVD resp. *free* for FMVD
30	`0` for BMVD resp. `1` for FMVD
31	*free*

Table 5.2: **Bitwise formation of data words**
Alternatively, one can interpret the bits 10-18 as the number of the channel within a half-module.
Bit 20 can be used as a boolean information, if one changes from the number of the half-module to: "inner" half-module `true/false`. Obviously, the same procedure is valid for bit 30 as: FMVD `true/false`.

5.2.2 Computing the Calibration Parameters

The computing of the calibration parameters follows the principles introduced in section 5.1. For every event, first the common mode is calculated[2] and subtracted[3]. Fig. 5.10 compares the data before (a) and after (b) the subtraction of the common mode.

Then the resulting signals are used to calculate the pedestals[4] for every single channel. This procedure is repeated for every event and the current pedestal is updated. With an increasing number of events, the pedestal becomes stabler and stabler. The value of noise is calculated in parallel[5]. This evolutions can be reconstructed in Fig. 5.11(a), where the signal after subtracting the common mode and the evolution of the pedestal and noise value are shown for *one* channel over 200 events. Fig. 5.12 illustrates the smoothing of the signal distribution by considering the pedestals. It shows the signals from Fig. 5.10(b) before (a) and after (b) the subtraction of the individual pedestals.

[2] v. equation (5.1)
[3] v. equation (5.2)
[4] v. equation (5.3)
[5] v. equation (5.6)

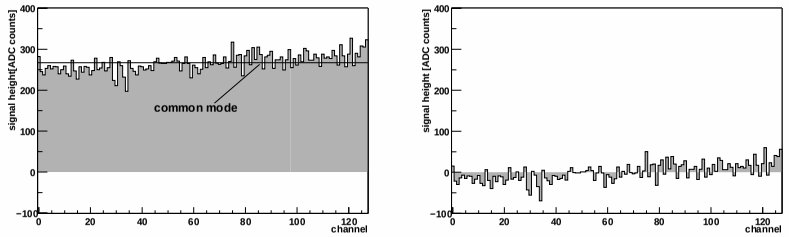

(a) (b)

Figure 5.10: **Subtraction of common mode**
The signal height as a function of the channel number for the data of one event for one chip.
(a) The raw signal. The resulting common mode is drawn in as a line.
(b) The signal after subtraction of the common mode. The average is zero now.

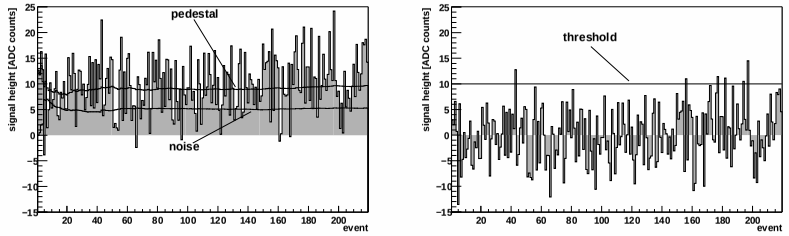

(a) (b)

Figure 5.11: **Calculation of pedestal and noise**
The signal height as a function of the event number for data of one channel over 200 events.
(a) The signal after subtraction of the common mode. The evolution of the pedestal and noise updates is drawn in as lines.
(b) The signal after additional subtraction of the pedestal together with the resulting threshold of 2σ drawn in as a line. One can identify the signals of six events higher than the threshold. These are 3 % of all events, what roughly corresponds to the expected fraction of 2.28 % (v. Tbl. 5.1).
In practice, the content of (b) is not calculated during pedestal and threshold computation.

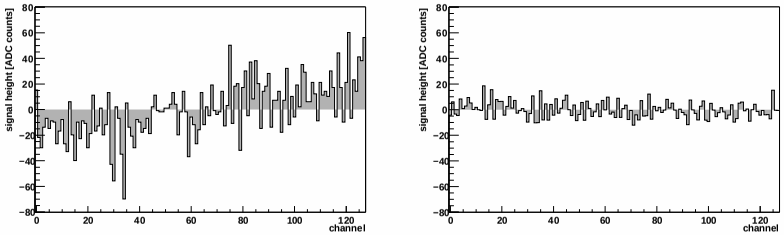

(a) (b)

Figure 5.12: **Subtraction of pedestal**
The signal height as a function of the channel number for the data of one event for one chip.
(a) The signal after subtraction of the common mode. It is the same histogram as in Fig. 5.10(b), shown on a different scale.
(b) The signal after additional subtraction of the pedestals.

The effect of the threshold[6] is demonstrated in Fig. 5.13, where one can compare the signals of a hit event before (a) and after (b) considering the threshold[7]. There remain only some signals higher than the threshold. These will be eliminated by the cluster algorithm.

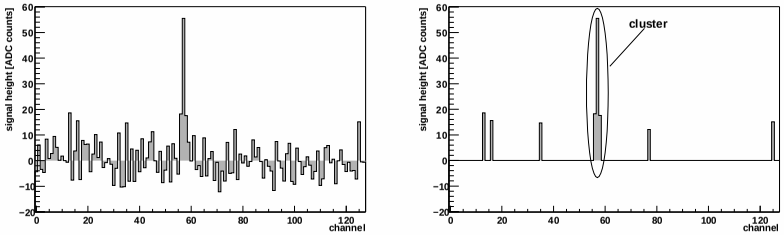

(a) (b)

Figure 5.13: **Using the threshold**
The signal height as a function of the channel number for the data of one event for one chip. The channels 56 - 58 contain the signals of a hit.
(a) The signals after subtraction of common mode and pedestal. One can identify the hit around channel 57, but its width is smeared by the surrounding noise.
(b) The signals above threshold. Besides the hit signal, some signals of other channels are above the threshold accidentally.

Coming back to the initial point of Figs. 5.1(b) and 5.2(b), where one hit from a particle crossing the detector is hidden in the signal distributions. The same signal distributions are shown in Fig. 5.14 after subtraction of common mode and pedestal, but without suppressing signals under thresholds.

[6] v. equation (5.7)
[7] v. equation (5.8)

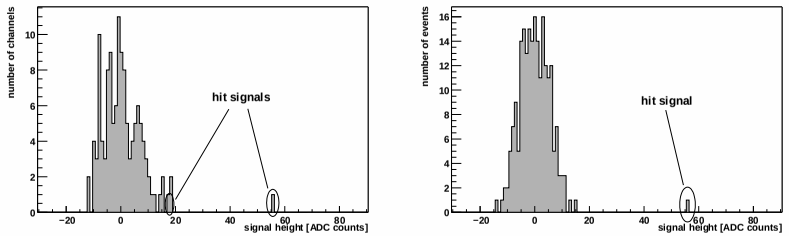

(a) (b)

Figure 5.14: **Signal distributions after subtraction of common mode and pedestal**
(a) Distribution over all channels of one chip in one event, containing hit signals from three channels. The highest hit signal, which is hidden in Fig. 5.1(b), can be identified.
(b) Distribution over all events of one channel, containing one hit signal. Other than in Fig. 5.2(b), the (real) signal height can be estimated as the value on the x-axis. The accuracy of this estimation is equal to the noise of the channel (v. Fig. 5.9).

5.2.3 Online Histograms

To get an overview of the calibration parameters and their correctness, histograms are the optimal tool. They make an immediate diagnose possible by observing their evolution online during the processing of the calibration parameters resp. data taking. Fig. 5.15 gives an example of online-histograms from the MVD RC showing the absolute values of the BMVD pedestals subdivided into single histograms for every ladder.

5.2.4 The Calibration Files

The calibration files are simple ASCII-files containing the calibration parameters of all channels in hexadecimal code, divided into files containing pedestals resp. thresholds. The contained data is initialised to the ADC for data taking to process the incoming data from the MVD, following the principles described in section 5.1. In the threshold files, just the thresholds calculated from equation (5.7) are stored. For the pedestals, the processing is a little more complicated.

5.2.4.1 The Stored Pedestal

The ADC is able to deal with positive values only. If the calculation method described in section 5.1 is used, one can expect negative values for half of the pedestals. To avoid this problem, an additional step is implemented for the pedestal calculation:
The common mode is calculated and subtracted. Then the pedestals are obtained. They can be negative. Chip by chip, which is the calculation unit of the common mode, an offset is added to all the pedestals, so that the lowest value of pedestals is zero. In this way the pedestals are higher than the calculated ones, but they are low enough not to produce negative signals after pedestal subtraction. During data taking processing, the ADC subtracts the pedestals first. The offset mentioned above is compensated during the following common mode calculation, because it is the same for all channels of one chip. A treatment of negative calibration parameters can be avoided in this way.

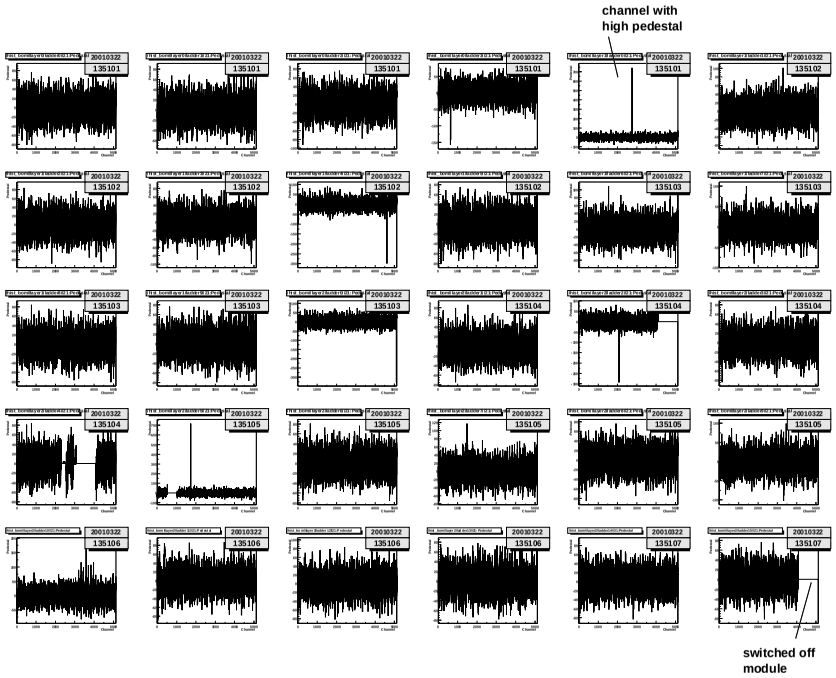

Figure 5.15: **Online-histograms**
Example of histograms for each ladder of the BMVD, giving the absolute values of all channels' pedestals. The histograms are tabulated starting with cylinder 0, ladder 0 (C0L0), continuing with C0L1 and ending up with C2L15. At first sight, one can identify parts switched off (clusters of zeros) and single channels with failures (values higher than normal).

5.2.4.2 "Bad" Channels

The calibration files also have the task to indicate channels, which are faulty because of their values of noise or pedestal ("bad" channels). A channel is called "bad", if either his pedestal, or his noise is too high. The criteria for such a diagnose are [4]:

- absolute value of signal height of pedestal > 200 ADC counts,
- signal height of noise > 20 ADC counts.

If a channel is indicated as bad ("masking"), the ADC should ignore the signal of this channel. As shown in Tbl. 5.2, there are only 10 bits to store the signal height of a channel, which results in a maximum signal height of 1023 ADC counts. This value is stored as the pedestal of bad channels. Then the calculated signal height of a related channel automatically becomes zero, after the ADC has subtracted this high value. Though the signal is ignored, the existence of the channel is not. The calculation of the common mode is still done for all 128 channels of a chip. Usually the resulting discrepancy due to this partly incorrect treatment is much lower than the variation of

the common mode from noise effects. Tbl. 5.3 gives some mean values for the numbers of bad channels.

Bias setting	`70V`		`stable2`	
Parameter	pedestal	noise	pedestal	noise
BMVD	12	45	11	37
FMVD	1	18	0	19
complete MVD	12	64	11	56

Table 5.3: **Numbers of channels with bad calibration parameters**
All numbers are mean values over all runs belonging to the specified bias voltage setting. Discrepancies between the sum of the numbers belonging to detector parts and the numbers belonging to the complete MVD are caused by rounding errors from the mean value calculation.
The bias voltage setting `70V` contains nine runs, the bias voltage setting `stable2` four. A list of the underlying calibration runs and bias voltage settings can be found in Tbl. C.1.

5.2.4.3 Distributions of Calibration Parameters

Typical distributions of calibration parameters for the complete MVD are shown in Fig. 5.16[8].

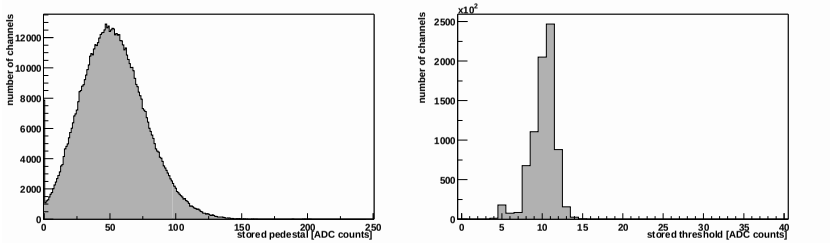

(a) (b)

Figure 5.16: **Distributions of calibration parameters for the complete MVD**
Distribution of (a) pedestals and (b) thresholds, from calibration runs with bias voltage setting `stable2`.
Values, which cause masking, and values from switched off or faulty modules are excluded.
In (a) the peak at zero is a consequence of shifting all pedestals to positive values with a zero at least once per chip (v. section 5.2.4.1).

If the calibration parameters are drawn as functions of the channel number within the MVD, one can observe that the calibration parameters are not distributed consistently. One can distinguish three classes of distributions of calibration parameters, called "class" henceforth. An example is given in Fig. 5.17. For a better visibility, not the individual calibration parameters of each channel are shown, but the averages over all channels processed by one chip.

[8] The number of channels, which are excluded by switched off or faulty modules amounts to 4608 (2.2 % of all). This number stays valid for the whole Chap. 5.

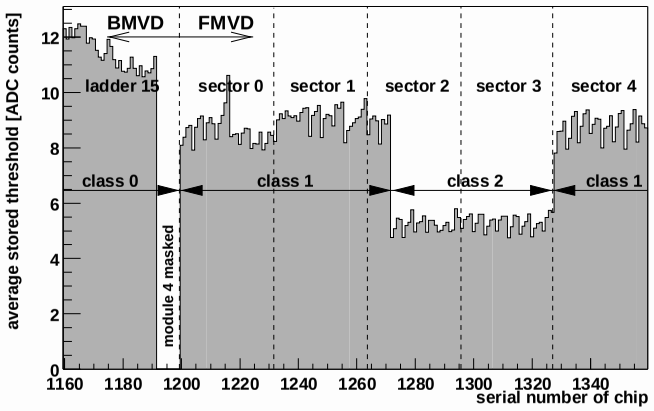

Figure 5.17: **Classes of distributions of calibration parameters**
Averages of chips' thresholds as a function of the serial number of the chip from calibration run 5467.
One can see a clipping, that shows all three classes.

Different classes are identified as:

- class 0: BMVD,
- class 1: FMVD, without class 2,
- class 2: sector 2, wheels 1 - 3, and sector 3 (complete)

Within the classes, the calibration parameters are Gaussian distributed. Fig. 5.18 shows the distributions of calibration parameters for the bias voltage setting `stable2`.

From the threshold distributions one can extract mean values of the noise within the classes, which are presented in Tbl. 5.4.

Detector class	noise mean	noise σ
0	5.40	0.45
1	4.35	0.40
2	2.65	0.25

Table 5.4: **Noise values for classes within the MVD**
Mean resp. σ are the mean value resp. the standard error of the Gaussian fitted to the noise distribution. All values are given in ADC counts.

5.3 Stability of Calibration Parameters

Due to statistical fluctuations, the calibration parameters can vary from calibration run to calibration run. These fluctuations should be small not to influence the data significantly. For channels with large fluctuations in the calibration parameters, one

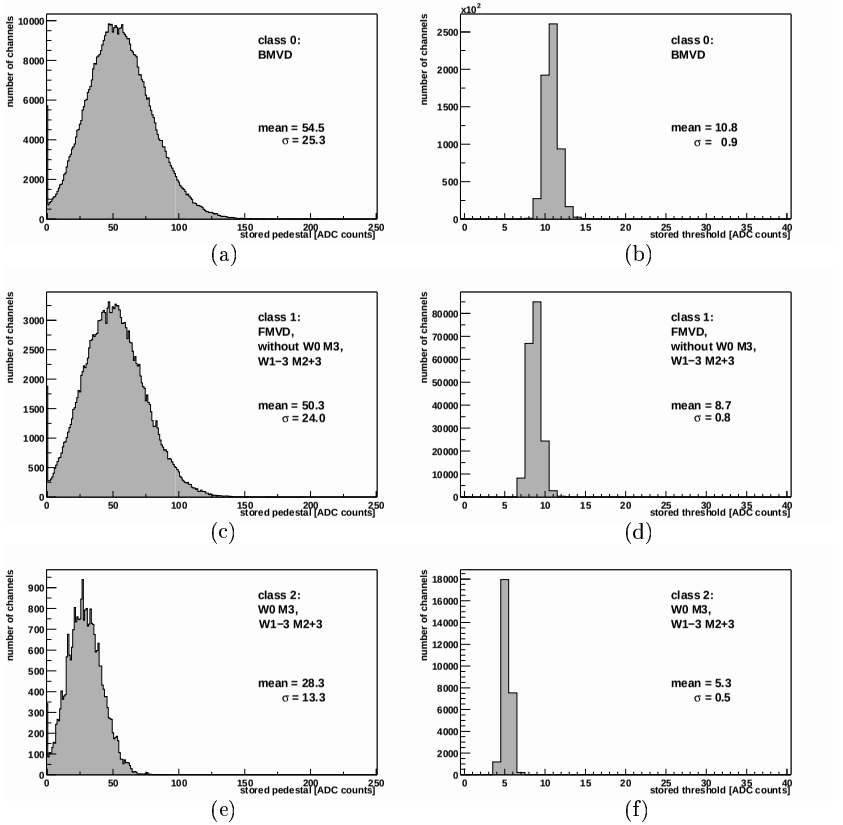

Figure 5.18: **Distributions of calibration parameters for classes within the MVD**
Distribution of (a) pedestals and (b) thresholds in class 0,
distribution of (c) pedestals and (d) thresholds in class 1 and
distribution of (e) pedestals and (f) thresholds in class 2
from calibration runs with bias voltage setting `stable2`.
Values, which cause masking, and values from switched off or faulty modules are excluded.
The reason for the peaks at zero in the pedestal distributions is the same as in Fig. 5.16.

can doubt whether these channels should be used for physics analysis, because large fluctuations are an indicator of an error or a damage in the detector or the readout chain. Therefore channels, which are unstable in calibration parameters, should be disabled for data processing.

In this section the method to find channels with unstable calibration parameters (called "unstable channels" henceforth) is described and the results of the search are presented.

5.3.1 Criteria of Instability

In sections 5.2.4.1 and 5.2.4.2 it is described, which limits are imposed on the calibration parameters, and how bad channels are masked. This masking can be used to distinguish between stable and unstable channels. The criterion is:

> An unstable channel can be identified as a channel with an unstable masking performance.

A channel is unstable, if it is masked in some calibration files, and not masked in some others. Masking a channel means that the masking value occurs for the pedestal. Unstable channels can be found by analysing only the stability of the pedestal.

The reasons for masking can be reconstructed only partially, because the original pedestal values are not stored in the pedestal files, but only the modified values resp. the masking value of 1023 ADC counts. So one can state that masking *at least* is due to a too high noise, if the noise masking value of 20 ADC counts is exceeded, or masking is due to a too high pedestal, if the noise masking value is not exceeded. But one cannot state that masking is due to a too high noise, because the pedestal cannot be reconstructed. For this analysis, channels with an unstable pedestal are investigated first. Then it is verified that the threshold and therewith the noise performance is unstable. A list of the underlying calibration files with bias voltage setting `stable2` is given in Tbl. C.1.

To quantify the variations of the calibration parameters of single channels, their standard deviation is extracted from the calibration files. It is defined as

$$\sigma_{ped} = \sqrt{\frac{\sum_{i=1}^{n} (x_{ped_i} - \overline{x_{ped}})^2}{n}}, \tag{5.9}$$

$$\sigma_{thr} = \sqrt{\frac{\sum_{i=1}^{n} (x_{thr\,i} - \overline{x_{thr}})^2}{n}}, \tag{5.10}$$

where x_{ped} is the modified pedestal stored in the pedestal files, x_{thr} is the integer threshold stored in the threshold files and n is the number of used calibration files. These standard deviations are computed for every single channel. Fig. 5.19 gives examples of their distributions.

In Fig. 5.19(a) one can observe an accumulation at $\sigma_{ped} \gtrsim 400$. One can suppose that this is caused by unstable channels. For the threshold, this kind of displaced accumulation cannot be observed. This can be explained by the fact that the difference between the masking value (pedestal: 1023, threshold: 40) and the highest allowed value (pedestal: 400, threshold: 40) is much larger for the pedestal than for the threshold.

To identify unstable channels, one has to define a minimum value (valid for both, pedestal and threshold separately), that identifies all channels with a standard deviation of the calibration parameter higher than this value as unstable – the so-called

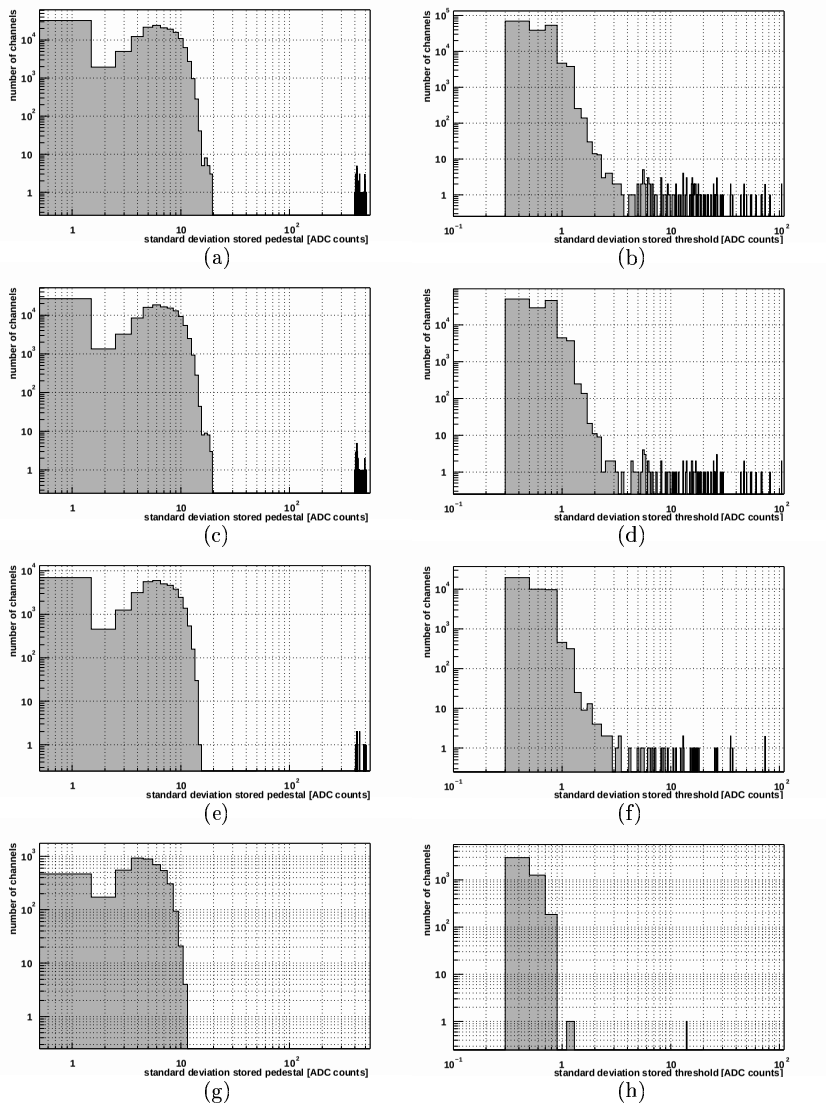

Figure 5.19: **Standard deviations of calibration parameters**
Distribution of standard deviations of
(a) stored pedestal and (b) threshold for complete MVD,
(c) stored pedestal and (b) threshold for class 0,
(e) stored pedestal and (b) threshold for class 1,
(g) stored pedestal and (b) threshold for class 2,
from calibration runs with bias voltage setting `stable2` ($n = 4$). Channels with no deviations of a calibration parameter and channels of switched off or faulty modules are excluded.

"borderline" $B_{ped,thr}$. To find an acceptable estimation for its value, one starts from the case of a constant calibration parameter for a single channel $x_i = x_{const}$ with the exception of one element in the array of n calibration files, which is at that value, when the masking occurs[9] ($x_i = x_{mask}$):

$$\begin{aligned} \sigma &= \sqrt{\frac{\sum_{i=1}^{n}(x_i - \overline{x})^2}{n}} \\ &= \frac{\sqrt{n-1}}{n} \cdot |x_{mask} - x_{const}|, \text{ with} \qquad (5.11) \\ \overline{x} &= \frac{(n-1)x_{const} + x_{mask}}{n}; \qquad (5.12) \\ x_i &= \begin{cases} x_{const}, i \neq n; \\ x_{mask}, i = n. \end{cases} \end{aligned}$$

This is valid for both, pedestal and threshold, for a single channel.

Although x_{const} is different for each channel, in a first approximation one can assume a common value for all channels associated to a class of distributions of the calibration parameters. In (5.11) the substitution $x_{const} = x_{mean}$ is made for this purpose. The resulting borderline-functions

$$\begin{aligned} B_j(n) &= \frac{\sqrt{n-1}}{n} \cdot |x_{mask} - x_{mean_j}| \\ &= \frac{\sqrt{n-1}}{n} \cdot (x_{mask} - x_{mean_j}) \qquad (5.13) \end{aligned}$$

with the index of the class j, the values of x_{mean_j} given in Fig. 5.18 and $x_{mask} > x_{mean_j} \forall j$, do not consider the whole calibration parameter distribution, but only the mean, what can be observed clearly for the pedestal deviations in Fig 5.20. There the values of the borderline function are not lower than all values found in the accumulation observed in Fig. 5.19. For channels with a pedestal larger than the mean, the borderline-function yields too high values. Therefore it is not able to distinguish stable from unstable channels.

For a better efficiency to find unstable channels, the distributions of pedestals have to be considered instead of the constant values x_{mean_j}. Treating the σ of a calibration parameter distribution as its error, error propagation yields the error of the borderline-function $\sigma_{B_j(n)}$ as

$$\sigma_{B_j(n)} = \frac{n-1}{n\sqrt{n}} \cdot x_{\sigma_j}, \qquad (5.14)$$

where x_{σ_j} is the σ of the distribution of calibration parameter x for class j from Fig. 5.18. Using a threshold of 2σ, the corrected borderline-function is

$$B_j(n) = \frac{\sqrt{n-1}}{n} \cdot (x_{mask} - x_{mean_j} - 2x_{\sigma_j}). \qquad (5.15)$$

The borderline functions (corrected and uncorrected) and their effects on the distributions of the calibration parameter deviations are shown in Figs. 5.20 and 5.21.

[9] highest allowed value

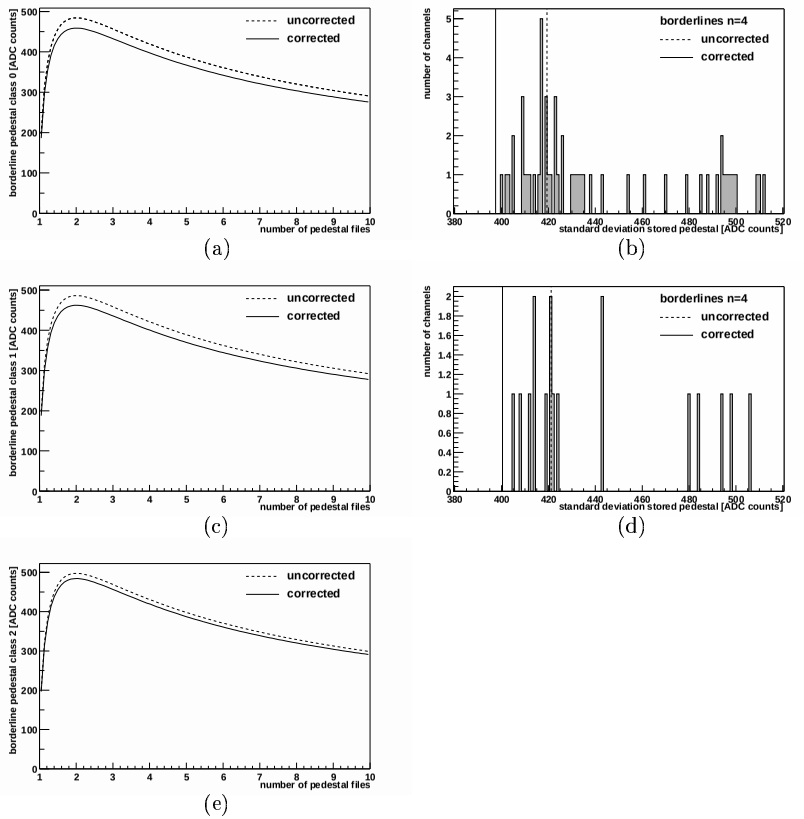

Figure 5.20: **Borderline-functions for the pedestal**
Borderline-function as a function of the pedestal file index (a, c, e) calculated only with the mean pedestal (uncorrected) and considering the standard deviation (corrected), and distribution of the standard deviations of the stored pedestals (b, d) (v. Fig. 5.19(c, e)) for class 0 (a, b), class 1 (c, d) and class 2 (e) from calibration runs with bias voltage setting `stable2`.
For class 2 no channel shows a standard deviation of the pedestal in the range of the borderline-function.

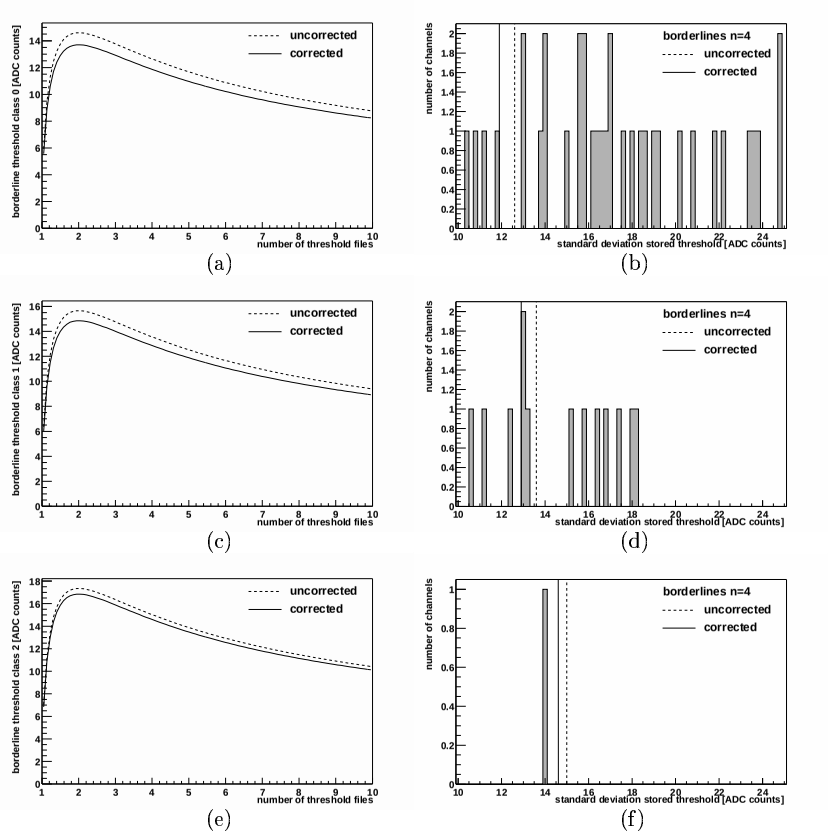

Figure 5.21: **Borderline-functions for the threshold**
Borderline-function as a function of the threshold file index (a, c, e) calculated only with the mean threshold (uncorrected) and considering the standard deviation (corrected), and distribution of the standard deviations of the stored thresholds (b, d, f) (v. Fig. 5.19(d, f, h)) for class 0 (a, b), class 1 (c, d) and class 2 (e, f) from calibration runs with bias voltage setting `stable2`.

5.3.2 Results

The analysis of calibration parameter deviations has been made for various sets of calibration runs with a constant bias voltage setting. A complete list of the analysed calibration runs can be found in Tbl. C.1. The masked modules have not been considered in this analysis, although some of them have not been masked during the whole analysed data taking period. This leads to the numbers of analysed channels shown in Tbl. 5.5.

Detector part	total	analysed	fraction
BMVD	153600	149504	97.3%
FMVD	57344	57344	100.0%
complete MVD	210944	206848	98.1%

Table 5.5: **Numbers of channels analysed for stability of calibration parameters**

Some of the affected channels show a different behaviour, when comparing different bias voltage settings. After the change from constant bias voltages to settings, which are adjusted to the measured depletion voltage for each half-module (called `new`, `stable0`, `stable1` and `stable2`), the number of unstable channels has decreased significantly. The proportion of the channels identified as unstable from bias voltage setting `stable2` to all channels identified as unstable amounts to 55.4% for BMVD, 63.2% for FMVD and 57.8% for the complete MVD. For bias voltage setting `stable2`, only 70 channels of the whole MVD have an unstable behaviour. These are 0.034% of all analysed channels, what is a very satisfying result. Tbl. 5.6 gives the results from analysing both, all data sets and only the data set coming from the optimised bias voltage setting `stable2`. An explicit list of the unstable channels in `stable2` is found in section D.1.1, the complete list including all bias voltage settings and additional comments in [11].

Bias setting	all		`stable2`	
BMVD	83	0.056%	46	0.031%
FMVD	38	0.066%	24	0.042%
complete MVD	121	0.058%	70	0.034%

Table 5.6: **Number of channels with unstable calibration parameters**
The fractions are calculated with respect to the number of analysed channels given in Tbl. 5.5.

Since no channel with unstable pedestal, but stable noise is found, for all channels of the MVD with unstable calibration parameters one can state:

Instability of calibration parameters at least means instability in noise.

5.4 Summary

In this chapter, the importance of a correct and effective signal calibration has been explained and the meaning of the calibration parameters common mode, pedestal and threshold are introduced, and their calculation has been illustrated.

For usage within the MVD DAQ RC, a procedure has been developed to read and interpret the MVD signal data, to compute and to store the calibration parameters

and to generate online monitoring histograms. The developed software has been incorporated successfully into the MVD DAQ RC software and is an inherent part of the present ZEUS RC.

Calibration parameter distributions have been shown in Fig. 5.18. Noise mean values have been presented in Tbl. 5.4. Together with the mean value of the gain[10], one can extract a signal-to-noise ratio of

$$S/N_{BMVD,systemtest} = 14.6 \pm 2.7 \tag{5.16}$$

for the BMVD in the system test, which is rather low compared to the value of $S/N_{testbeam} \approx 21$ for the test beam measurements. The lower signal-to-noise ratio makes it more difficult to keep apart signals from crossing particles and pure noise signals.

An analysis of the stability of the calibration parameters has been performed: 206848 of the 210944 MVD channels (98.1%) have been studied. Thereby a fraction of $\gtrsim$ 99.96% of all analysed channels has been found to show stable calibration parameters under an individually adjusted bias voltage setting. This corresponds to a fraction of $\gtrsim$ 98.0% of all MVD channels. All of the unstable channels at least show instability in noise performance. Additionally for this individually adjusted bias voltage setting an average fraction of $\gtrsim$ 0.03% of all MVD channels show too high calibration parameters, every fifth of them solely a too high pedestal.

Both the number of unstable channels and the number of channels, which show too high calibration parameters, are significantly lower for the individually adjusted bias voltage setting than for bias voltage settings with constant voltage. Therefore it is recommended to operate the MVD with this individually adjusted bias voltage setting in future HERA operations.

[10] v. Fig. 4.5(b)

Chapter 6

Digitisation of Detector Signals

To test physics assumptions and to unfold the detector response in high energy physics (HEP) experiments, the data measured with the detector are compared to data obtained from Monte Carlo (MC) simulations. At ZEUS, the generation of an MC data set consists of four steps [25]:

1. The event generation:
   At this point the underlying physics model is implemented. A complete list of particles produced in *ep*-interactions and their 4-momenta is created. The interface to different event generators at ZEUS is called `AMADEUS`[1].

2. The detector simulation:
   It produces a list of detector signals as response on the particles from the event generation. Here the interaction of each particle with the detector is tracked step-by-step, and the detector response is simulated. At ZEUS the detector simulation is called `MOZART`[2].

3. The trigger simulation:
   It decides, if the signals from `MOZART` lead to a trigger signal and the event is recorded. At ZEUS the trigger simulation is called `CZAR`[3] resp. `ZGANA`[4].

4. The event reconstruction:
   It is used for the reconstruction of real and simulated detector data. At ZEUS it is called `ZEPHYR`[5].

The input files produced by `AMADEUS` are fed into `MOZART`, `CZAR/ZGANA` and `ZEPHYR` by the ZEUS Monte Carlo production facility called `FUNNEL`. Fig. 6.1 shows the relations of all these components in a flow diagram.

The digitisation step is part of the detector simulation. It simulates the signals of a single detector component for given parameters of a crossing particle, like e.g. 4-momentum of the particle, impact position and incidence angles (impact geometry). In case of the MVD, the signals of single strips are simulated for the impact geometry regarding the concerned sensor. The aim of the work presented in this chapter is to compare a simulation tuned to test beam data , which uses single detectors, to the data of the MVD in the final set-up as used in the system test, and to improve it where necessary. The impact geometry parameters used for the simulation are obtained from

[1] "`AMADEUS` is, what comes before `MOZART`."
[2] `MO`nte carlo for `ZEUS` Analysis, Reconstruction and Trigger
[3] Complete `ZGANA` Analysis Routines
[4] `ZEUS` Geant `ANA`lysis
[5] `ZEUS` `PHY`sics events Reconstruction

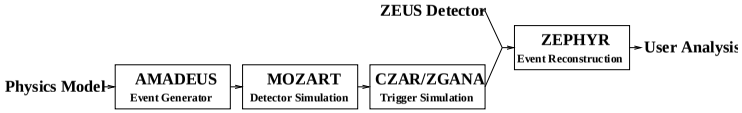

Figure 6.1: **ZEUS MC simulation chain**

the system test data by the MVD track fit program [15], which also delivers information on the cluster signals. Both are needed to compare the simulation to the real data.

A detailed simulation of the charge distribution caused by an energy deposition of a crossing particle has been performed in [16, Chapter 4]. Its approach is based on an electrical model where each strip is charge coupled to all strips on the sensor. The calculation was based on PSpice®. It has been able to reproduce detailed features of the MVD sensors, but the needed processing time is too long for practical applications. A simpler simulation software based on a parametrisation of the data is required to increase the speed of the simulation.

The underlying model of the MVD digitisation is introduced in section 6.1. In section 6.2 the costumising of the simulation parameters to fit the real data obtained from the MVD system test is described. Section 6.3 deals with the analyses of the simulation results and the comparison to an analysis of the real data.

All details given in this chapter refer only to BMVD sensors.

6.1 Simulation Model

The simulation of the response of an individual MVD sensor to a traversing particle consists of four steps:

1. generation of free holes,
2. drift of holes to strips, considering diffusion,
3. charge collection at the readout strips (charge sharing),
4. output of analog signals as the detector response including noise.

It is based on a program introduced in [1] and the improvements described in section 3.3.3.

6.1.1 Charge Carrier Generation

First it is assumed that $25 \cdot 10^3$ free electron-hole pairs are generated by a MIP traversing an MVD sensor of thickness $300\,\mu$m perpendicularly [1, section 2]. This corresponds to an initial charge carrier density[6] of $f_0 \approx 83.3 \cdot 10^3$ free holes per millimeter track-length within Si. The generated electron-hole pairs are distributed uniformly along the particle tracks. Thus the absolute number of generated holes is proportional to the length of the track within the sensor.

[6] introduced in (2.40)

6.1.2 Charge Diffusion during Drift

The simulation of the hole diffusion in the x-y-plane follows the principles introduced in section 2.2.4. Thereby the integrations over the drift-time in (2.42) and the x- and z-coordinate in (2.45) are replaced by sums over small intervals. The numbers of intervals stay constant. For the intervals in the x- and z-coordinate the widths of the intervals stay constant, too. The width of the drift-time intervals varies and depends on the current z-coordinate, the depletion voltage of the sensor and the applied bias voltage. The chosen values of numbers and widths of the intervals and of assumed voltages can be found in Tbl. 6.1.

Finally the simulation of the charge diffusion yields the number of holes collected on every considered strip after their drift to the strips.

6.1.3 Charge Distribution on Readout Strips

The charge read out by the readout strips has to be calculated from the charge collected by all strips. This is done by using transfer coefficients[7].

The transfer coefficient gives the fraction of the charge collected on one strip, which is transfered to the readout strip depending on its distance to the charge collecting strip. Therefore an array of charges, which are picked up from the collecting strips, is assigned to every readout strip.

The described simulation model divides this array into two parts: one for the left and one for the right side (negative and positive transfer coefficient IDs[8]). The charge collected on the considered readout strip is divided by two. The charges of both parts are summed up. At this point the Landau distibution of the energy loss of charged particles in thin absorbers[9] is taken into account. The total charges collected on each side become the MPVs of the energy loss MPV_{Landau}. The width of the Landau distributions $FWHM_{Landau}$ is calculated from the distance s the crossing charged particle has traveled in the Si as described in [1, section 3.3]:

$$FWHM_{Landau} = 0.38 \cdot (e^{-0.009 \cdot s} + 0.92) \cdot MPV_{Landau}. \tag{6.1}$$

This equation is based on a fit to a MC simulation of five points of $FWHM_{Landau}(s)$ given by G. Merzon and V. Sechin (Lebedev Institute of Physics (FIAN), Moscow). From the resulting Landau distributions values are chosen by a random number generator, which give the charges picked up by the considered readout strip from each side. These charges are summed up and give the total charge picked up from all strips by the readout strip.

6.1.4 Detector Response

The simulation of the charge carriers in the sensor is followed by a simulation of the readout electronics, which includes the calculation of the analog signal height, the electronic's noise and the cluster algorithm performed by the ADC.

The generation of the analog signal height is simulated by multiplying the charge by a factor, which has to be adjusted to data. Since it is not known a priori, it can be adjusted definitely in different simulation scenarios, like for e.g. changes in the transfer coefficients array.

[7] v. section 3.3.3
[8] v. Fig. 3.12
[9] v. section 2.2.2

The noise simulation generates a random noise value for every readout channel from the measured Gaussian noise distribution[10]. A noise signal is generated from a Gaussian distribution with the mean value 0 and the noise value as standard error. It is added to the analog signal height to obtain the final analog signal.

To compare measured and simulated data, the final analog signals are filtered by the same cluster algorithm the ADC has performed during the system test [10].

6.1.5 Constants Used in the Digitisation

A set of constant parameters is used in the digitisation, which are presented in Tbl. 6.1.

Constant		Symbol	Value	
assumed depletion voltage		V_{depl}	65 V	
assumed bias voltage		V_{bias}	70 V	
number (width) of intervals	n_x	(dx)	4	$(5\,\mu\text{m})$
	n_z	(dz)	20	$(15\,\mu\text{m})$
	n_t	(dt)	5	(varying)
assumed density of free hole generation along particle track		f_0	$\sim 83.3 \cdot 10^3\,\text{mm}^{-1}$	
noise distribution [ADC counts]:	mean		5.40	
	standard error		0.43	

Table 6.1: **Constants used in the digitisation**
The assumed voltages are obtained from Tbl. B.4. The parameters of the noise distribution are obtained from Tbl. 5.4 (class 0).

6.2 Customising of Simulation Parameters

To obtain a reliable digitisation, various simulation parameters have to be fitted to the data, like e.g. the factor to get a correct signal height[11] (gain) or the transfer coefficients. To reach this goal, first of all a suitable set of measured data and an underlying position reconstruction algorithm have to be selected.

The coordinate system of an MVD sensor is shown in Fig. 6.2.

6.2.1 General Run, Event and Hit Selection Criteria

For tests of the digitisation, only runs with the optimised bias voltage settings `stable1` and `stable2`[12] are used.

Since the underlying geometry of the MVD has been aligned only for the z-coordinate so far[13], but not for the x- and y- resp. for the r- and ϕ-coordinate[14], systematic effects on the position reconstruction have to be studied. Therefore the dependencies of the

[10] v. section 5.2.4.3
[11] v. section 6.1.4
[12] v. Tbl. C.2
[13] This alignment takes into account only the survey measurement done by NIKHEF (Nationaal Instituut voor Kernfysica en Hoge Energie Fysica), Amsterdam, and is not yet based on measurements from particles crossing the detector.
[14] coordinates in the ZEUS coordinate system

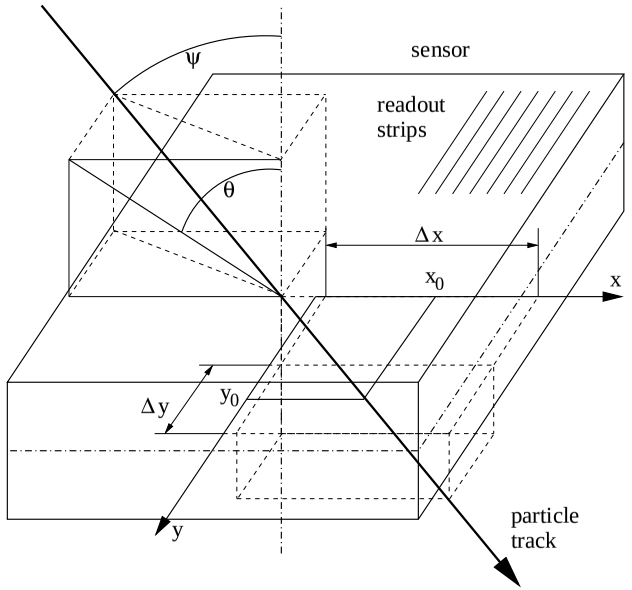

Figure 6.2: **The MVD sensor coordinate system**
The point of origin is located in the centre of the sensor. The track coordinates x_0 and y_0 are given for $z_0 = 0$.
The picture is not drawn to scale.

residual on the particle incidence angle θ and on the calculated cluster position within the sensor are shown in Fig. 6.3. The residual of a cluster is defined as the distance of the calculated cluster position[15] to the calculated position of the particle track[16]. Thereby this particle track is fitted *without* considering this cluster in the track fit. An optimal residual distribution shows *no* dependence on any parameter and a constant mean value of 0 μm.

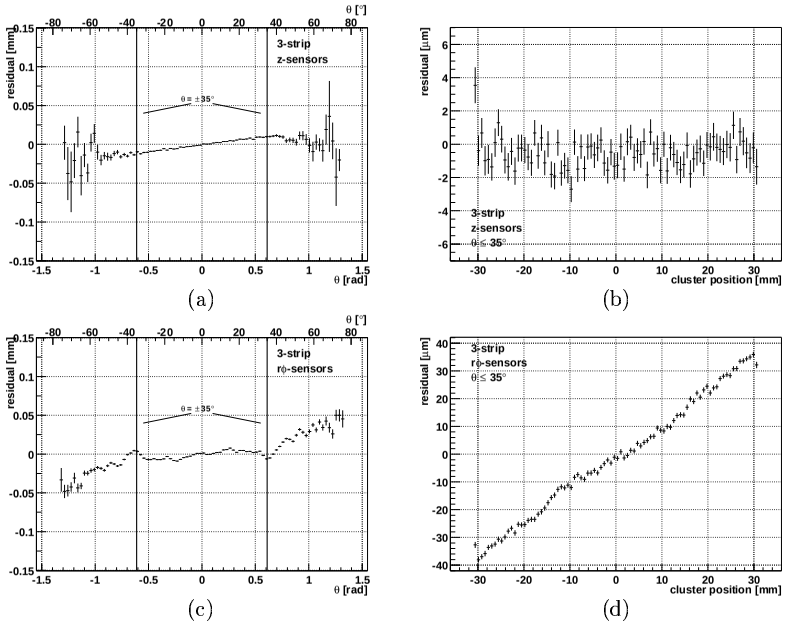

Figure 6.3: **Comparison of residuals measured in the z- and ϕ-sensors (3-strip-algorithm)**
Mean residual as a function of the particle incidence angle θ on the x-y-plane for (a) the z-sensors and (c) the ϕ-sensors and mean residual as a function of the calculated cluster position on the sensor for (b) the z-sensors and (d) the ϕ-sensors. All errors are given by the standard error.
Cluster positions are calculated by the 3-strip-algorithm, the centre-of-gravity-algorithm shows the same behaviour (v. Fig. D.1).

For the z-sensors the residual shows a linear dependence on θ. For perpendicular incidence, the mean of the residuals is approx. 0 μm. This indicates a systematic effect of the track fit algorithm. A deterioration of the resolution, which is indicated by an increase of the errors of the residual distribution, can be observed for $|\theta| > 35°$, as predicted in section 3.3.2. A dependence of the residual on the calculated cluster position within the sensor is not observed for the z-sensors, except a small overall offset of approx. -0.5 μm, which might be due to the accuracy of the description of the MVD geometry, which is limited to 1 μm. For the ϕ-sensors, the dependence of the mean

[15] The cluster position is calculated from the cluster shape.
[16] The track position is calculated from the overall track fit.

residual on θ looks more complicated. The dependence of the mean residual on the calculated cluster position is linear and very strong. Obviously, the MVD geometry is unreliable for the r- and ϕ-coordinate. This is not surprising, since no alignment corrections have been made for this coordinates. Therefore for tests of the digitisation only measured data of the z-sensors are usable for position measurements.

To get an optimal gain, a cut on the trigger time is performed[17]. To get rid of noise, minimum values are defined for the signal of the highest strip in the cluster, the sum of all signals in the cluster and the signal of the single strips in the cluster. To exclude clusters containing signals caused by δ-electrons, signals above a threshold are excluded.

The used selection criteria are summarised in Tbl. 6.2.

Object	Property	Symbol	Min.	Max.
Run	bias voltage setting		`stable2`	
Event	trigger time [ns]		135	165
	number of crossed hits		3	
	number of hits (including ghost hits)			100
Track	*no selection criteria*			
Hit	sensor type		z-sensor	
	particle incidence angle	θ	0°	35°
	signal of highest strip in cluster [ADC counts]		27	82
	sum of signals in cluster [ADC counts]		32	600
	signal of single strip [ADC counts]		11	82

Table 6.2: **General selection criteria used to test the digitisation**
"Crossed hits" are hits in both half-modules of a module (v. Fig. 3.4).

6.2.2 Choice of the Position Reconstruction Algorithm

In section 3.3.2, the properties of different position reconstruction algorithms have been discussed. For small particle incidence angles, the η-algorithm yields the best resolution, but the 3-strip-algorithm is less sensitive to sensor effects, which depend on the y-coordinate of the particle hit on the sensor. Moreover, the 3-strip algorithm needs no a priori knowledge, which has to be obtained from the data beforehand, like e.g. the η-function, to reconstruct the position of the particle incidence point. This also is the case for the centre-of-gravity-algorithm. Since the head-tail-algorithm is useful only for the position reconstruction with large particle incidence angles, the 3-strip- and the centre-of-gravity-algorithm are available as a possible choice to be used for the digitisation.

Fig. 6.4 shows the distribution of the residuals and the correlation of the calculated cluster position to the calculated position of the particle track. The mean of the residual distribution indicates a possible systematic bias introduced by an algorithm. The width of the distribution gives an estimation of the resolution. The relation of the calculated cluster position to the calculated position of the particle track indicates the reliability of the position reconstruction. In the optimal case, both positions approximately coincide.

The residual distributions show no obvious difference. The RMS and the standard

[17] v. Fig. 4.4

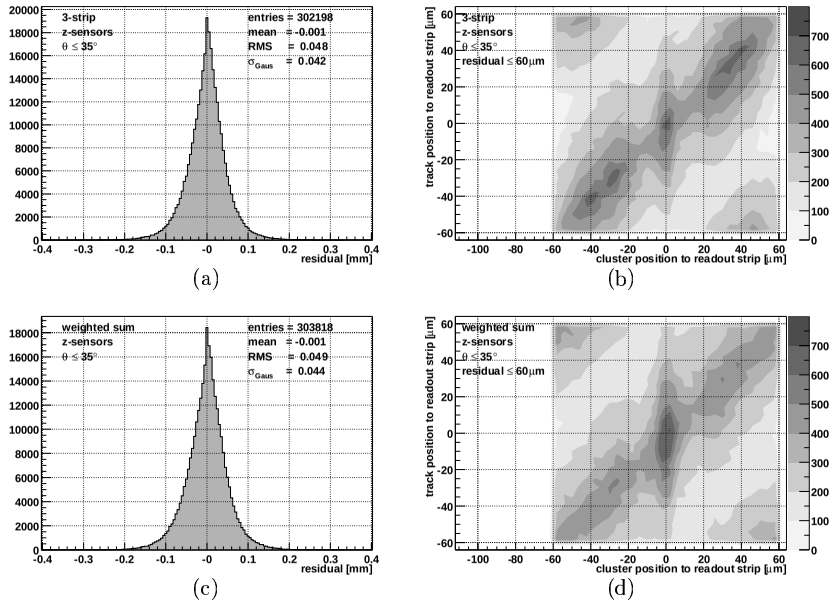

Figure 6.4: **Comparison of the residual distribution and the correlations of the calculated cluster position and track position obtained for 3-strip- and centre-of-gravity-algorithm (z-sensors)**
Distributions of residuals for (a) the 3-strip-algorithm and (c) the centre-of-gravity-algorithm and calculated position of the particle track relative to the next readout strip as a function of the calculated cluster position relative to the next readout strip for (b) the 3-strip-algorithm and (d) the centre-of-gravity-algorithm.
The corresponding figures for the ϕ-sensors are shown in Fig. D.2.

error of a Gaussian fit[18] as characteristic values for the width of a distribution are similar. But the correlation of cluster and track position is better for the 3-strip-algorithm. Therefore this algorithm is chosen to test the digitisation.

6.2.3 Signal Height

As described in section 6.1.4, the simulated analog signal heights have to be adjusted to the measured data. Since the height of the measured analog signal depends on the readout electronics, a difference of the signal height for variations in the electronics can be expected. Indeed the readout electronics has been changed from test beam to system test measurements.

The simulated signal height is adjusted to measured data by adjusting the distribution of the highest signal in the cluster. Fig. 6.5 shows the effect of this procedure on this distribution and the distribution of all signals in the cluster.

[18] The distributions are not really Gaussian, but most publications use this value to characterise the resolution, like e.g. [15]. The values quoted are just given for comparison.

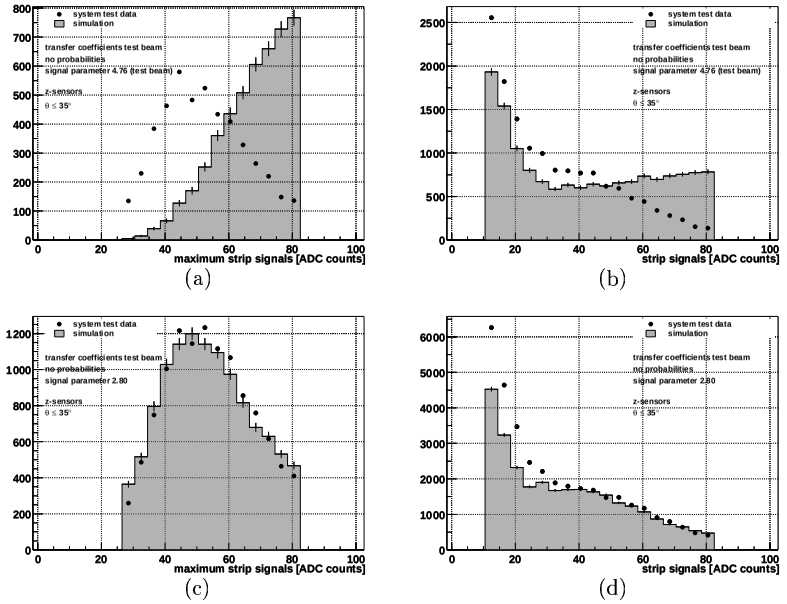

Figure 6.5: **Effects on parameters of the cluster shape by modifying the signal height**
Distributions of (a), (c) maximum signal heights of clusters and (b), (d) of all signal heights. (a), (b) show the signal heights for a simulation adjusted to the test beam data and (c), (d) the signal heights adjusted to the maximum signal as measured in the system test.
The complete sets of control plots for these simulations are shown in Figs. D.7, D.8.

One easily sees that for simulation parameters obtained in the test beam the measured signals are much higher than measured signals in the system test. To describe the distribution of the highest signal in the cluster, the simulated signal height has to be lowered for $\sim 60\,\%$. Nevertheless the distribution of all signals in the cluster shows discrepancies, especially for low signals. Therefore the second free parameter of the simulation has to be adjusted: the array of the transfer coefficients

Since the transfer coefficients describe the charge flowing to the readout strips, also the factor scaling the highest strip signal has to be readjusted, when the transfer coefficients are changed. A final value for the system test and therewith for the ZEUS environment cannot be given at this point.

6.2.4 Transfer Coefficients

The meaning and the usage of the transfer coefficients is explained in section 3.3.3. In this section, the method to obtain them from the system test data is described and the effects of variations of the underlying parameters are shown.

6.2.4.1 Hit Selection Criteria to Determine the Transfer Coefficients

Transfer coefficients are a parametrisation of the charge sharing obtained from the data[19]. The principle is to measure the relative heights of signals as a function of the distance to the point of the signal generation. The point of the signal generation in terms of an MVD sensor means the x-coordinate of the electron-hole-pair generation.

For a particle crossing the sensor with $\theta \neq 0°$, the electron-hole-pairs are not generated at a certain x_0, but within a range of $\left[x_0 - \frac{\Delta x}{2}, x_0 + \frac{\Delta x}{2}\right]$. If both limits of this range have the same closest strip, the charge is generated completely within the region of this strip. Since the transfer coefficients are not calculated for a certain distance in x, but for certain distances in strip numbers, such a particle track can be used for the calculation, because it can be allocated to a certain strip. To verify, if a track can be used, a "road" is defined, which must contain the track completely, what depends on x_0 and θ. The road is illustrated in Fig. 6.6. For practicle purposes, it is defined closer than the whole strip region to avoid the diffusion of significant parts of the drifting charge to a neighboured strip.

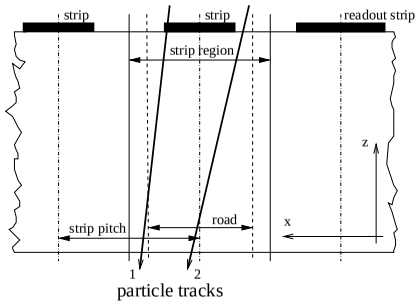

Figure 6.6: **Definition of the road for the transfer coefficients specification**
Particle track 1 leaves the road, particle track 2 stays inside the road.
The picture is not drawn to scale.

The signal height depends on the track length. Therefore the track length has to be limited by restricting the particle incidence angle ψ. Furthermore the residual and the cluster size are used to reject clusters, which seem not to be reasonable. All measured data are used. Limits on signal heights or are not applied. The selection criteria used to determine the transfer coefficients are summarised in Tbl. 6.3.

6.2.4.2 Binning of Fitted Histograms and Fitting Range

To calculate the transfer coefficients, all signals in the clusters are normalised to a scaling signal first. This scaling signal is obtained from clusters, which match the selection criteria[20], and where the strip hit by the crossing particle is a readout strip. The signals of this strip and its two neighbours, even if their signal is 0 ADC counts resp. not measured, are summed. The sum is filled into a histogram. The histogram is fitted by a Landau distribution, and the MPV gives the scaling signal. Since the scaling signal is only a proportionality factor, whose effect on the simulation can be

[19] v. section 3.3.3
[20] v. section 6.2.4.1

Property	Symbol	Value
width of the strip region (= strip pitch)		20 μm
width of the road		15 μm
particle incidence angle	ψ	$< 5°$
residual		$\leq 60\,\mu$m
number of strips in the cluster		≥ 2
sensor type		z-sensor
bias voltage setting		`stable2`

Table 6.3: **Selection criteria for the transfer coefficients determination**

changed by adjusting the signal height[21], and which depends on other parameters of the transfer coefficient calculation, it needs not to be considered as free parameter in the following.

The normalised signals are filled into histograms. Each histogram contains the signals of readout strips with a certain distance to that strip, where the particle has crossed the sensor and the primary charge has been generated. The histograms are fitted by Landau distributions, and the MPVs of this distributions are the transfer coefficients with respect to the distance to the particle track.

A fit to a histogram is not unique. Besides the used algorithm, the fit result usually also depends on the chosen histogram layout. Two parameters, which influence the fitting results, are the binning and the fit range. For testing the digitisation, two settings of each of these parameters have been considered:

- the binning of the histograms:
  - fine binning:
    Every bin contains only *one* possible signal height, e.g. one bin contains all signals of 11 ADC counts, the next contains all signals of 12 ADC counts, etc.
  - coarse binning:
    Every bin contains *four* possible signal heights, e.g. one bin contains all signal of 3, 4, 5 and 6 ADC counts, the next contains all signals of 7, 8, 9 and 10 ADC counts, etc.

  For every binning the low edge of one bin must be 11 ADC counts and the upper edge of another bin must be 82 ADC counts.

- the fit range:
  - fit including noise:
    All signals $>$ 0 ADC counts and $\leq$ 82 ADC counts are fitted.
  - fit excluding noise:
    All signals $\geq$ 11 ADC counts and $\leq$ 82 ADC counts are fitted.

The used edges resp. limits refer to the values given for the signals of a single strip in Tbl. 6.2. All given values can be transfered to the normalised signal scale.

For testing the digitisation, a fit to histograms with coarse binning excluding noise is chosen. It is shown in Fig. 6.7. The fine binning increases the influence of statistical

[21] v. section 6.2.3

fluctuations of the signal distributions[22]. A fit including noise cannot be justified on physical grounds, because noise is not generated by the charge sharing, but by the readout electronics, and therefore it should be simulated separately from the charge distribution.

The problem of obtaining transfer coefficients from the system test data is seen clearly: Because of the low signal-to-noise ratio (14.6 compared to 21 during the test beam measurements), for transfer coefficients with $ID \gtrsim 8$ the signals from crossing particles cannot be distinguished from the noise background, because the noise fraction in the measured data increases drastically, while the signal height decreases for high transfer coefficients. The Landau fit is unreliable in this region. Since for lower IDs the Landau fit appears to be reliable, it is reasonable to perform the simulation using the transfer coefficients obtained from this fit. The negative effects caused by the unreliable determination of the transfer coefficients have to be studied in the following.

To control the quality of the transfer coefficients, one can inspect the gradient of the energy loss between the two centred readout strips of the cluster, which are the strips in the neighbourhood of the track position. This is done by summing up their attached transfer coefficients. For particles hitting a readout strip, the transfer coefficients 0 and 6 are summed, for the next intermediate strip, the transfer coefficients 1 and 5 are summed, etc.[23]. Transfer coefficient 3 is simply doubled. The resulting sums are attached to the considered transfer coefficients to obtain a symmetric distribution for the transfer coefficients $0-6$. A monotonous decrease from the edges to the middle is expected as described in [16, section 4.6.3]. Fig. 6.8 shows the transfer coefficients from a fit with coarse binning (a) including and (b) excluding[24] noise and their gradient of the energy loss compared to the results of the test beam measurements, (c) compares both fits directly.

For the fit including noise, the transfer coefficients have values, which are similar to the ones obtained from the test beam data. This is expected, because, the transfer coefficients from the test beam data also are extracted by including noise. The MPV of the Landau fit for transfer coefficient 13 is negative, so all transfer coefficients with $ID \geq 13$ are set to 0 in the cluster simulation, even if there are MPVs of the Landau fit of positive values for $ID > 13$ ($ID = 18$ in this case). The fit excluding noise gives significantly larger transfer coefficients than the test beam measurements for $ID \gtrsim 5$, thus yet for transfer coefficients from a reliable fit. One can conclude that useful transfer coefficients are larger than those from the test beam measurements for $ID \gtrsim 5$ generally, even if this statement is supported only by four reliable values. An additional indicator for the higher reliability of the method excluding noise is the fact that the energy loss gradient is close to what is expected. This is not the casde for the fit including noise.

6.2.4.3 Transfer Probabilities

The high values of transfer coefficients for strips further apart from the particle track are expected to increase the contribution of these strips to the distributions of the signal height for the simulation. Fig. 6.9(a) shows the distribution of all signals in a cluster for a simulation using the transfer coefficients extracted from the fit with coarse binning excluding noise[25]. Compared to the system test data, the signals of small heights, which are dominated by the strips further apart, occur too often. This

[22] v. example in Fig. D.4
[23] v. Fig. 3.12
[24] v. Fig. 6.7
[25] v. Fig. 6.7

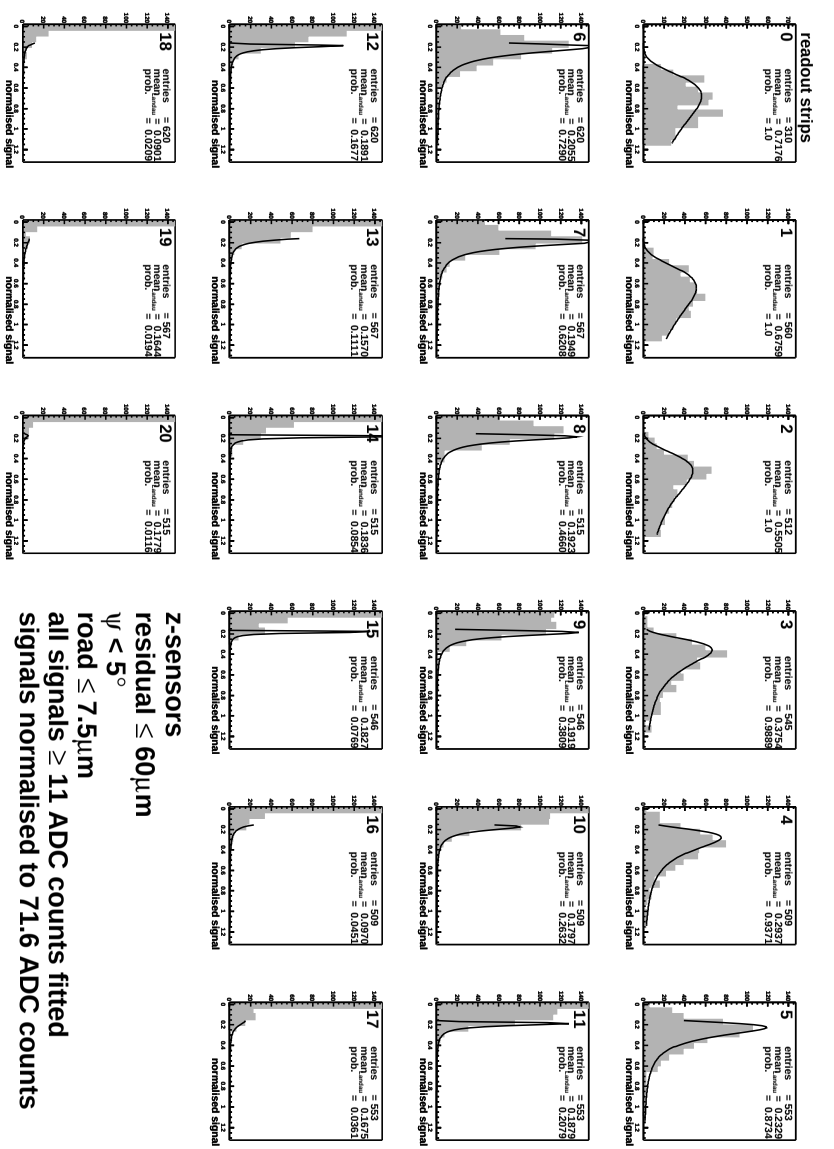

Figure 6.7: **Example of the normalised signal distributions, from which the transfer coefficients are obtained**
Distributions of normalised signal heights on readout strips without noise suppression for different calculated positions of the particle track with respect to the readout strip. For histogram 0, the particle track crosses the readout strip itself, for histogram 1 the next intermediate strip etc.
In this example, a fit to histograms with a coarse binning excluding noise is shown. Further figures of fitting the transfer coefficients with a different binning or/and fit range are shown in Figs. D.3 - D.4.

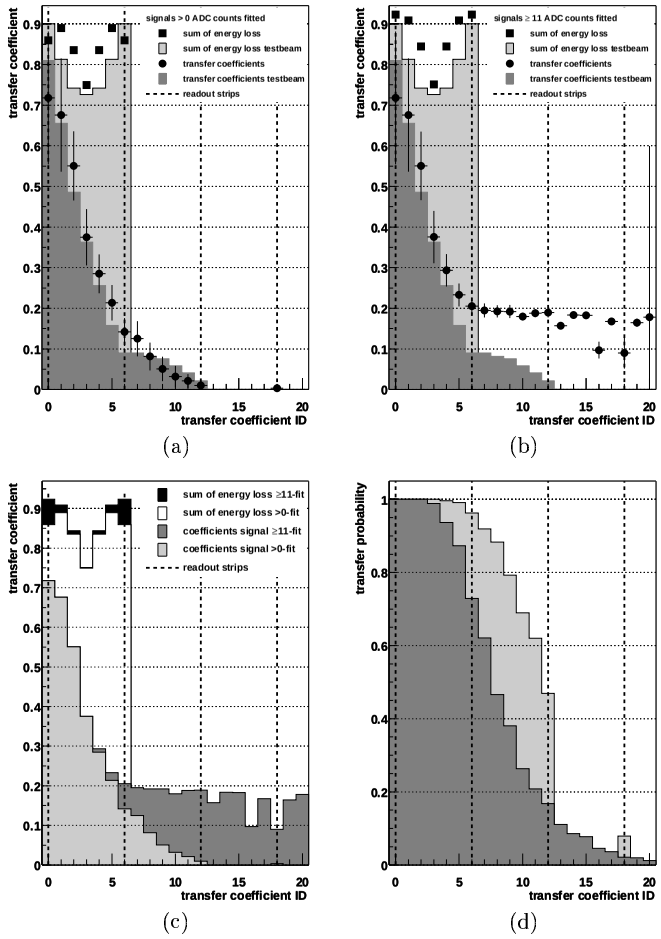

Figure 6.8: **Example of resulting transfer coefficients**
(a), (b) Transfer coefficients and their sum for the readout strips next to the calculated position of the particle track on both sides (energy loss) for a fit (a) including noise and (b) excluding noise. Both are compared to the results from test beam measurements.
(c) Comparison of (a) and (b).
(d) Comparison of corresponding transfer probabilities.
In this example, transfer coefficients and probabilities shown in Figs. 6.7 and D.3 (fits to histograms with coarse binning) are compared. A further figure comparing transfer coefficients and probabilities shown in Figs. D.4 and D.5 (fits to histograms with fine binning) can be found in Fig. D.6.

also effects the distribution of the sum of all signals in the cluster in Fig. 6.9(c) and the distribution of the cluster size in Fig. 6.9(e).

Since the fits to extract the transfer coefficients only treat certain fractions of all measured signals as signals from crossing particles, one also has to take these fractions into account for the simulation to solve this problem. This is done by using "transfer probabilities" in the simulation. They describe the probability to obtain a signal on a strip with a certain distance to the particle track as a function of the ID. The transfer probability $prob(ID)$ is defined as

$$prob(ID) = \frac{n_{fit}(ID)}{n_{entries}(ID)}, \tag{6.2}$$

where $n_{entries}(ID)$ is the number of entries in the fitted histogram and $n_{fit}(ID)$ is the number of these entries within the fit range.

In the simulation, the transfer coefficient ID is used with the probability $prob(ID)$, 0 otherwise. In Fig. 6.7, the related transfer probabilities are given within the histograms. Fig. 6.8(d) compares the probabilities of a fit including noise and a fit excluding noise. In connection with Fig. 6.8(c) one can observe that smaller transfer coefficients go together with larger probabilities. This is expected, because including noise into the fit lowers the transfer coefficient, but includes a larger fraction of signals into the fit. The result of using the transfer probabilities is shown in Fig. 6.9(b), (d) and (f).

Compared to the simulation neglecting the probabilities, the signal distributions match the system test data much better. A lack of small signals is observed in the distribution of all signals in the cluster, which effects the distribution of the sum of all signals in the cluster not that much than the distribution of the cluster size. This might be caused by the uncertainties in the transfer parameters (coefficients and probabilities) of higher IDs. Despite all difficulties, the usage of the transfer probabilities seems to be the correct method to handle the transfer coefficients.

Comparing the distribution of all signals in the cluster in the Figs. 6.9(b) and 6.5(d), one can see a noticeable improvement in the region of 20 – 40 ADC counts for the simulation using transfer parameters obtained from system test data. But the important fact is that the noise simulation and the simulation of the charge sharing are separated clearly in this simulation scenario.

6.3 Analyses of Simulated Cluster Data

This section deals with a closer look on a simulation done with transfer coefficients *and* probabilities from a fit with coarse binning excluding noise[26] to verify the quality of the simulation.

6.3.1 The Cluster Shape

The simulation of the cluster shape can be verified by looking individually to the distribution of all signal heights in the cluster subdivided by the distance to the calculated cluster position. This is shown in Fig. 6.10.

If the readout strip closest to the calculated cluster position is identical with that closest to the track position, what is the case for $\sim 95\,\%$ of all clusters, each histogram can be related to a certain subset of transfer parameters. These relations are listed in Tbl. 6.4.

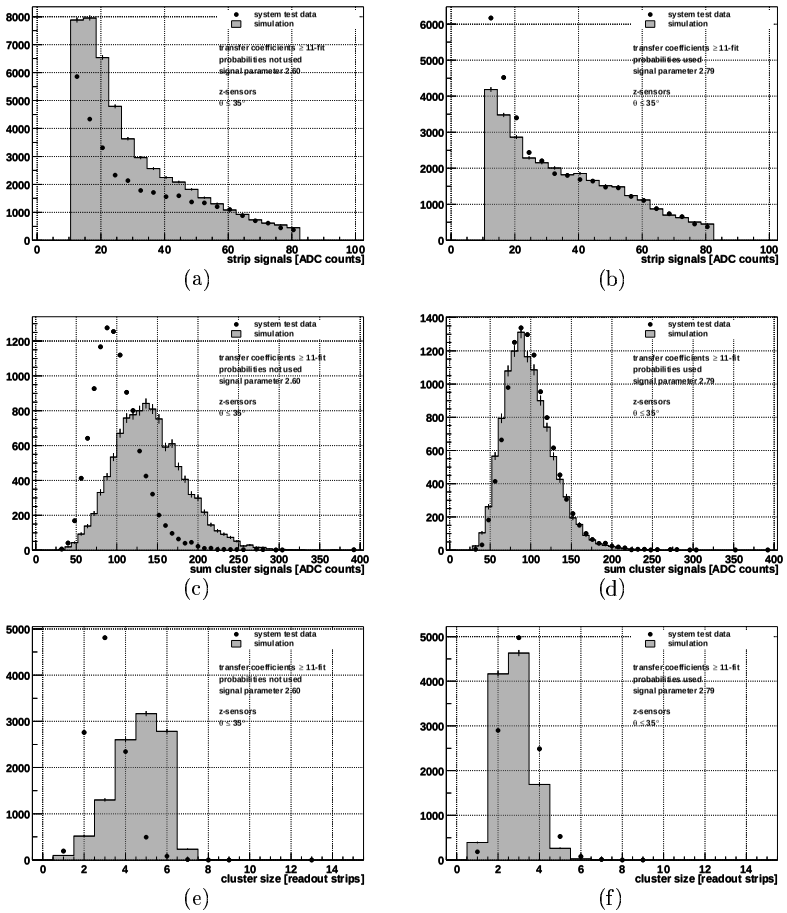

Figure 6.9: **Effects of the transfer probabilities on the cluster shapes**
Distributions of (a), (b) all signal heights, (c), (d) the sum of signal heights in clusters and (e), (f) cluster sizes. For (a), (c), (e) the transfer probabilities are not used, for (b), (d), (f) they are used. The signal heights have been adjusted individually to the maximum signal heights of the clusters for every simulation scenario.
In this example, the transfer coefficients and probabilities from a fit to histograms with coarse binning excluding noise have been used. The complete sets of control plots for these simulations and simulations with other transfer coefficients are shown in Figs. D.9 - D.16.

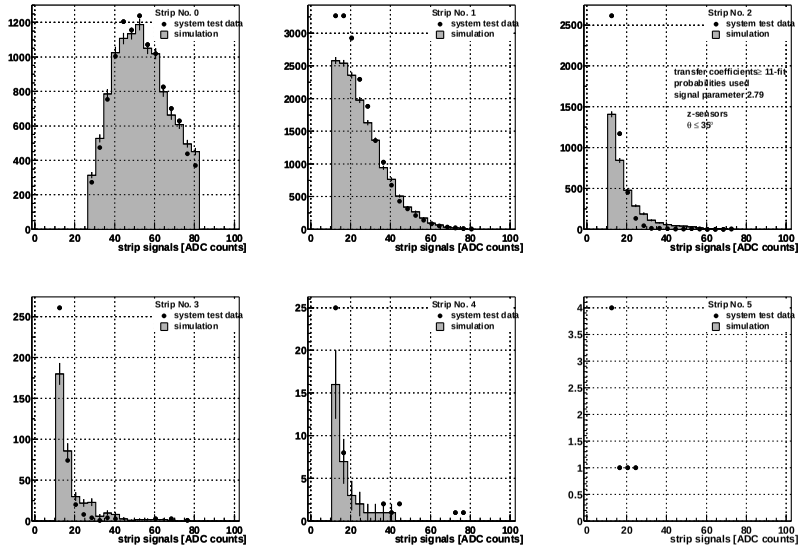

Figure 6.10: **Example of signal heights subdivided by the distance to the calculated cluster position**
Distributions of the signal heights. Strip No. 0 is the readout strip closest to the calculated cluster position, Strip No. 1 are its both next neighbours etc.
In this example, the transfer coefficients and probabilities from a fit to histograms with a coarse binning excluding noise have been used. Corresponding plots from simulations with different simulation scenarios are found in Figs. D.17 - D.19.

Since for strip 0 the simulation fits the data very well, one can assume that the transfer parameters 0 – 3 are reliable. For the strips 2 and 3 the distribution of the simulated signals shows a slight shift to larger signals, but fewer entries. One can conclude that the transfer coefficients are too large for larger IDs, but the probabilities are too small. This means that a fraction of signals caused by passing particles has been excluded by the limited fitting range in Fig. 6.7. Strip 1 shows a mixture of both, reliable and shifted transfer parameters. The occurrence of simulated signals for strip 4, although the related subset of transfer parameters does not exist in this simulation, can be explained by the small contribution of clusters with a wide distance between track and cluster position. Deformations of the shown distributions by wide clusters from large particle incidence angles θ are not expected within the scope of the 3-strip-algorithm ($\theta < 35°$).

6.3.2 Dependencies on the Particle Incidence Angles

For increasing particle incidence angles, crossing particles cover a longer track through the Si. This leads to a higher energy deposition and therewith to larger cluster sums.

[26] v. Fig. 6.9(b), (d), (f)

Strip No.	0	1	2	3	4	5
Transfer Parameter ID	0 – 3	3 – 9	9 – 15	15 – 21	21 – 27	27 – 33

Table 6.4: **Relations of the distance to the cluster position to subsets of transfer parameters**
Transfer parameter IDs > 20 are not used in the cluster simulation.

For increasing θ an increase of the cluster size is expected. This also should effect the distribution of all signals in the cluster such, that the fraction of noise becomes smaller. Fig. 6.11 shows the distributions of the parameters of the cluster shape for varying θ in a range of $0° \leq \theta < 75°$.

Increasing ψ at small θ should show an increase of the maximum signal in a cluster and a shift to higher values for the distribution of all signals in the cluster at a rather constant cluster size distribution. Fig. 6.12 shows the distributions of the parameters of the cluster shape for varying ψ in a range of $0° \leq \psi < 75°$ for $\theta < 35°$.

Both, the dependencies of the parameters of the cluster shape on the particle incidence angles θ and ψ behave as expected, except for the known discrepancies at small signals. The angular dependencies obtained from the system test data are described very well by the simulation. This shows that the approach of using the transfer parameters is successful.

6.3.3 The Resolution of the Digitisation

As described in section 6.2.2, the resolution can be characterised by the standard error of a Gaussian fitted to the residual distribution. For the simulation the residual is replaced by the distance of the simulated calculated cluster position to the "true" position of the particle track. In the simulation this position can be called "true", because the initial values of a simulation are not estimated parameters with errors related to "real" particles, but true parameters of "imaginary" particles. Fig. 6.13 shows the distribution of the position distances and the resulting resolution of the digitisation.

The obtained resolution of 26.7 μm is a good result at the actual point of the digitisation development. It is only 34 % worse than the required intrinsic resolution of the single hit position. One can expect further improvements, when advanced algorithms for the ADC clustering, the position reconstruction and the extraction of the transfer coefficients will be developed.

6.3.4 Summary of the Analyses

The analyses on the simulated cluster data have been done for the example of a simulation using transfer probabilities. The transfer parameters have been obtained from a fit to histograms with a coarse binning excluding noise.

The dependence of the distribution of all signals in the simulated clusters on the distance of the readout strips to the calculated cluster position has been compared to the behaviour of the system test data. For redout strips located close to the hit strip the simulation matches the data. At distances larger than the readout pitch, a significant lack of small signals has been observed. This is caused by a shift of the signal distribution to higher values than in the system test data, which coincides with a lower number of considered strips. At these distances the transfer coefficients are too large, but the transfer probabilities are too small. In this region, the determination of the

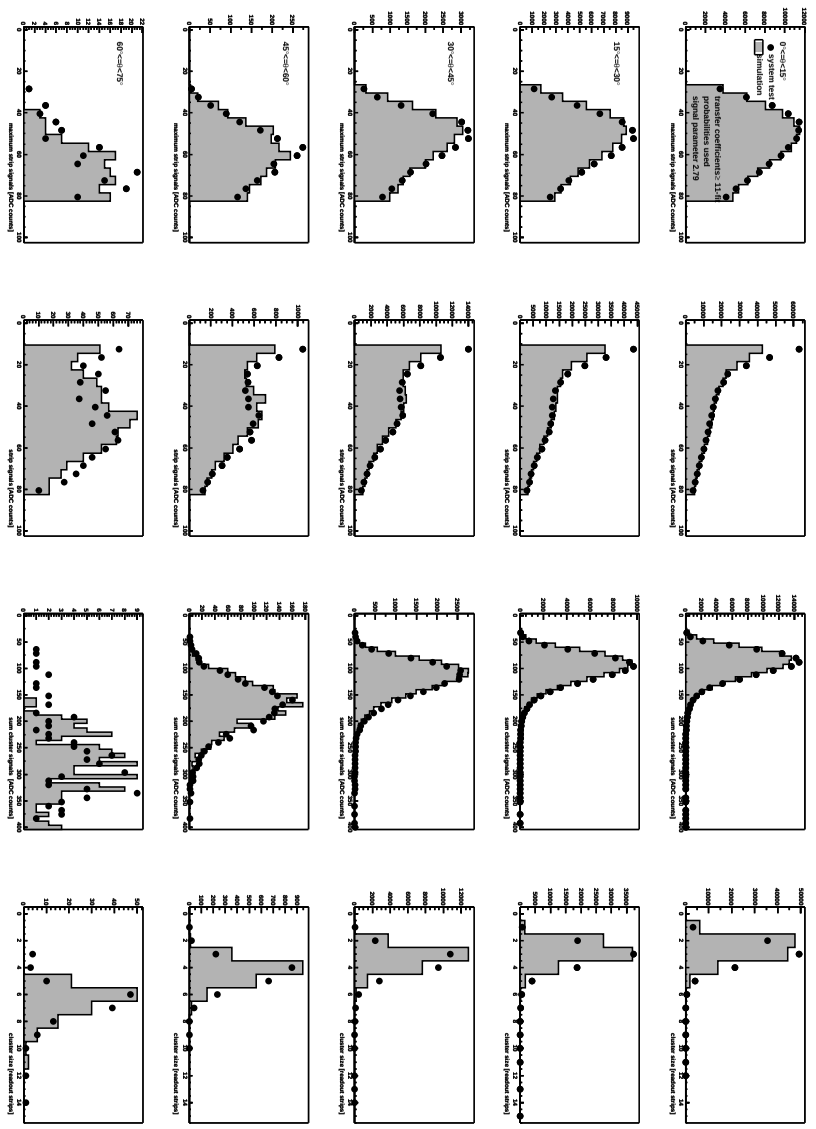

Figure 6.11: **Example of dependencies of the cluster shape parameters on the particle incidence angle θ**
Distributions of maximum signal heights of the clusters, all signal heights, sum of signal heights in the clusters and cluster sizes in a range of $0° \leq \theta < 75°$ using bins of 15°. In this example, the transfer coefficients and probabilities from a fit to histograms with coarse binning excluding noise have been used.

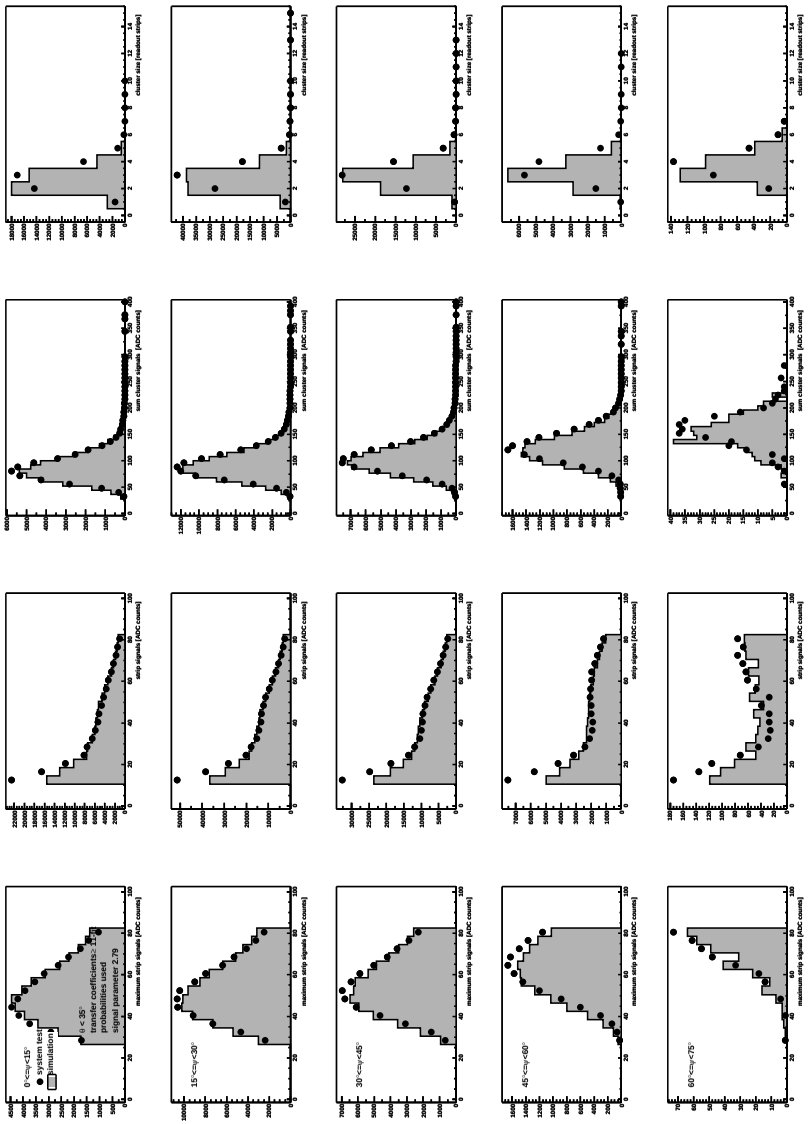

Figure 6.12: **Example of dependencies of the cluster shape parameters on the particle incidence angle ψ**
Distributions of maximum signal heights of the clusters, all signal heights, sum of signal heights in the clusters and cluster sizes in a range of $0° \leq \psi < 75°$ using bins of 15° for $\theta < 35°$.
In this example, the transfer coefficients and probabilities from a fit to histograms with coarse binning excluding noise have been used.

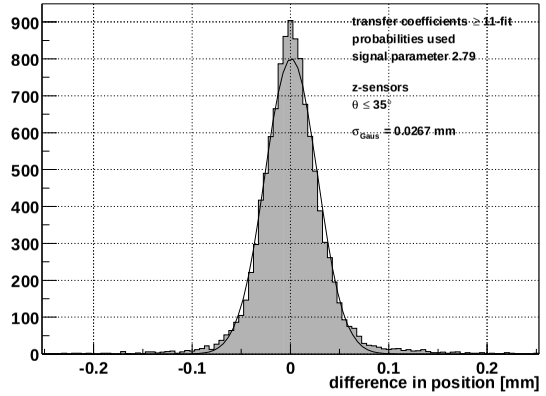

Figure 6.13: **Example of the resolution of the cluster simulation**
Distribution of the distances of the calculated simulated cluster positions to the true position, fitted with a Gaussian. The resolution of the simulation is given by the standard error of the Gaussian σ_{Gaus}.
In this example, the transfer coefficients and probabilities from a fit to histograms with coarse binning excluding noise have been used. Corresponding plots from simulations with other simulation scenarios can be found in Fig. D.20.

transfer parameters from the data is not reliable. Together with the simulation result, one can conclude that the fit used to extract the transfer parameters has excluded an important part of signals, which are caused by crossing particles, but are masked by the noise background.

Furthermore the behaviour of the simulation for different particle incidence angles θ and ψ has been investigated. Here the simulation shows a very good agreement with the system test data.

The resolution achieved with the digitisation reaches 26.7 μm, what is 34 % larger than the required intrinsic resolution on single hit positions. This value is satisfying, if one takes future improvements in diverse underlying algorithms in consideration.

6.4 Summary

In this chapter the simulation model for a digitisation of the MVD detector signals has been introduced, which simulates the charge generation by crossing charged particles in the sensor, the drift of the charge to the charge collecting strips and their coinciding diffusion, the charge sharing of the readout strips and the conversion of the charge to the final analog signals, including a simulation of the influences of the readout electronics.

Analyses on the system test data have shown, which data can be used as a solid basis for testing the digitisation. Because of the missing alignment of the MVD geometry for the r- and the ϕ-coordinate, only clusters from z-sensors can be used. The 3-strip-algorithm has been chosen, since it provides the most reliable position reconstruction.

Starting from the simulation scenario used for the test beam data, the agreement of the simulation with the system test data has been verified on the basis of the distribu-

tions of four cluster shape parameters: the signal of the maximum strip in the cluster, all signals in the cluster, the sum of the signals in the cluster and the cluster size. The overall signal height of the simulation is customised by adjusting the simulated distribution of the maximum strip signal to the system test data. This has shown that this simulation scenario is not able to match the system test data. It has been concluded that one has to take the change of the signal-to-noise ratio to a lower value in the system test into account. Therefore new transfer coefficients are needed to parametrise the charge sharing. They have been extracted from the system test data.

The method of using the transfer coefficients has been refined by excluding noise effects, and the transfer probability has been introduced. It describes the probability with respect to the real data that the charge collected on a strip leads to a signal on a readout strip, depending on the distance between these strips. For signals from the neighbourhood of a particle track, this method describes the real data very well. For signals from readout strips further apart from the track, the transfer coefficients are over-estimated, the probabilities are under-estimated. This is caused by noise masking the small signals from crossing particles. In the distribution of all signals this leads to a significant lack of small signals. Nevertheless the refined method improves the simulation with respect to the simulation scenario obtained from the test beam data. On one hand the distribution of all signals in a cluster matches the data better. On the other hand the noise has lost its influence on the charge distribution in the simulation extensively. This corresponds to the real facts of the detector behaviour.

For a selected simulation scenario, the angular dependence of the simulation has been checked. It behaves exactly like the system test data.

The resolution achieved with the digitisation has reached

$$res_{digitisation} = 26.7\,\mu\text{m}. \tag{6.3}$$

This is only 34 % worse than the required intrinsic resolution of single hit positions, what is satisfying at this point of the digitisation development. The expected improvements in many underlying algorithms, like e.g. the ADC cluster algorithm or the position reconstruction will have positive effects on this value as well as a more accurate extraction algorithm for the transfer parameters.

Chapter 7

Summary and Outlook

The system test of the ZEUS Microvertex Detector (MVD) has been performed successfully. Slow control (SC) and run control (RC) operated stable and reliably. This was also the case for the data acquisition (DAQ). Only three modules and one half-module could not be read out, what corresponds to $\sim 1.7\,\%$ off all readout channels. $2.5 \cdot 10^6$ cosmic ray events have been recorded.

A mean efficiency of the hit reconstruction of $\sim 97\,\%$ for the BMVD sensors has been achieved without any alignment corrections of the MVD geometry description. The timing of the BMVD and the FMVD is consistent. The gain of the BMVD half-modules is quite constant.

A procedure has been developed to compute and store the MVD signal calibration parameters and to generate online monitoring histograms. The developed software has been incorporated successfully into the MVD DAQ RC software, and meanwhile it is an inherent part of the present ZEUS RC.

For the BMVD, a signal-to-noise ratio of

$$S/N_{BMVD,systemtest} = 14.6 \pm 2.7$$

has been measured.

A study of the stability of the calibration parameters for 98.1% of the MVD channels have shown that $\gtrsim 99.96\,\%$ of these channel perform stable. Furthermore only 0.03 % of all MVD-channels have too high calibration parameters permanently. This good results have been achieved by using an individually adjusted bias voltage setting, which is recommended to be used in forthcoming HERA operations.

Measurements on the residuals of single hits from crossing particles with respect to the fitted particle track give an estimation of the reliability of the position reconstruction. This is used to define a position reconstruction algorithm and a certain set of the system test data as the bases to test the simulation of the analog detector signals (digitisation). The combination of the 3-strip-algorithm applied to data from the BMVD-z-sensors for a particle incidence angle of $\theta \leq 35°$ has been chosen.

A simulation using the transfer coefficients obtained from the test beam data has shown that these transfer coefficients are not able to describe the system test data. For this reason, new transfer coefficients have been extracted from the system test data. Thereby the method of the extraction has been refined by avoiding noise effects, and by introducing the transfer probabilities.

A simulation using the new transfer coefficients and the transfer probabilities has shown noticeable improvements in the description of the system test data. Especially

the analog signals generated close to the impact point of the particle are reproduced very well. In contrast to this, the amount of signals generated further apart from the impact point still cannot be simulated correctly. Prbably this is caused by the signal-to-noise ratio, which is worse in the system test with respect to the test beam measurements ($S/N_{testbeam} \approx 21$). A fraction of low signals is masked by noise. This makes the extraction of the transfer parameters (coefficients and probabilities) difficult. For readout strips further apart from the impact point, on the one hand the transfer coefficients are too large, on the other hand the transfer probabilities are too small.

In summary, despite some difficulties in reproducing the detector response for small signals far away from the hit strip correctly, the method using the transfer parameters to describe the charge sharing between the strips on an MVD sensor is successful in the digitisation. A resolution of

$$res_{digitisation} = 26.7\,\mu\text{m}$$

has been reached. To achieve a further improvement, the algorithms of the ADC clustering and the position reconstruction have to be advanced, and the MVD geometry description has to be improved by further alignment corrections. Also the extraction of the transfer parameters has to become more effective in identifying signals from crossing charged particles.

The MVD has been assembled and installed into the ZEUS-Experiment successfully in spring 2001. It has participated in the commissioning of the HERA beams. The physics runs will start with e^+p-runs in spring 2002 and will be continued with e^-p-runs from summer 2002 on.

Appendix A

Physical Units and Constants

A.1 Frequently Used Units and Constants

Constant	Symbol	Value
Angstrøm unit		$1\,\text{Å} = 10^{-10}\,\text{m}$
Electron Volt		$1\,\text{eV} = 1.60218 \cdot 10^{-19}\,\text{J}$
atomic mass unit		$1\,\text{amu} = 1\,\text{g mol}^{-1}$
speed of light in vacuum	c	$2.99792 \cdot 10^{8}\,\text{ms}^{-1}$
elementary charge	e	$1.60218 \cdot 10^{-19}\,\text{C}$
Planck constant	h	$6.62617 \cdot 10^{-34}\,\text{Js}$
reduced Planck constant	$\hbar$	$\frac{h}{2\pi} = 1.05458 \cdot 10^{-34}\,\text{Js}$
Boltzmann constant	k	$1.38066 \cdot 10^{-23}\,\text{JK}^{-1}$
electron rest mass	m_e	$0.511\,\text{MeV}c^{-2} = 0.91095 \cdot 10^{-30}\,\text{kg}$
proton rest mass	m_p	$0.938\,\text{GeV}c^{-2} = 1.67264 \cdot 10^{-27}\,\text{kg}$
Avogadro constant	N_A	$6.02204 \cdot 10^{23}\,\text{mol}^{-1}$
Bohr radius	r_B	$0.52917\,\text{Å}$
classical electron radius	r_e	$2.817 \cdot 10^{-13}\,\text{cm}$
permeability in vacuum	μ_0	$4\pi \cdot 10^{-9}\,\text{Hcm}^{-1} = 1.25663 \cdot 10^{-8}\,\text{Hcm}^{-1}$
permittivity in vacuum	ϵ_0	$\frac{1}{\mu_0 c^2} = 8.85418 \cdot 10^{-14}\,\text{Fcm}^{-1}$
normal atmosphere		$1.01325 \cdot 10^{5}\,\text{Nm}^{-2}$
room temperature		$300\,\text{K}$

Table A.1: **Frequently used physical units and constants**

A.2 Silicon

Constant	Symbol	Value
atom density		$5.0 \cdot 10^{22}\,\text{cm}^{-3}$
atomic number	Z	14
atomic weight	A	$28.09\,\text{amu}$
breakdown field		$\sim 3 \cdot 10^{5}\,\text{Vcm}^{-1}$
lattice structure		Diamond
density	ρ	$2.328\,\text{gcm}^{-3}$
dielectric constant	ϵ_r	11.9
effective density of states in conduction band	N_C	$2.8 \cdot 10^{19}\,\text{cm}^{-3}$
effective density of states in valence band	N_V	$1.04 \cdot 10^{19}\,\text{cm}^{-3}$
drift mobility of holes	μ_h	$450\,\text{cm}^2\text{V}^{-1}\text{s}^{-1}$
drift mobility of electrons	μ_e	$1500\,\text{cm}^2\text{V}^{-1}\text{s}^{-1}$
energy gap	E_g	$1.12\,\text{eV}$
intrinsic charge carrier density	n_i	$1.45 \cdot 10^{10}$
intrinsic resistivity	ρ	$2.3 \cdot 10^{5}\,\Omega\text{cm}$
minimum ionisation energy loss rate (muons)	$\left\lvert\frac{dE}{dx}\right\rvert_{min}$	$1.664\,\text{MeVg}^{-1}\text{cm}^2$
effective ionisation potential (average over all electrons)	I	173 eV
lattice constant	a	5.43095 Å
melting point		$1415\,^{\circ}\text{C}$
sound speed [1]	c_{Si}	$7 \cdot 10^{3}\,\text{m s}^{-1}$

Table A.2: **Constants of Si properties**
Values are valid for intrinsic Si at $T = 300\,\text{K}$ ([19],[22]).

Appendix B

Technical Descriptions and Data

B.1 Numbering of MVD Components

To identify components of the MVD, a numbering scheme is defined, which uses acronyms for the MVD components. The acronyms are listed in Tbl. B.1.

component	acronym
barrel part	BMVD
forward part	FMVD
cylinder	C
ladder	L
wheel	W
module	M
half-module	H
chip	X
channel	CHN

Table B.1: **Acronyms of the MVD numbering scheme**

For the identification of e.g. a special channel, the numbering starts with the cylinder resp. the wheel number. Therewith one can also distinguish between BMVD and FMVD. Each component is counted within the superior component, except the channels, which are counted within the half-modules. All numbers start from 0. So e.g. channel 245 of half-module 0, module 3, ladder 7, cylinder 2, BMVD is identified by

C2 L7 M3 H0 CHN245.

The sensors and strips cannot be identified within the MVD DAQ and do not belong to this numbering scheme.

The numbers of MVD components contained in superior components are given for the BMVD in Tbl. B.2 and for the FMVD in Tbl. B.3.

in	**BMVD**	**C0**	**C1**	**C2**	**L**	**M**	**H**	**X**
cylinders	3	—	—	—	—	—	—	—
ladders	30	4	10	16	—	—	—	—
modules	150	20	50	80	5	—	—	—
half-modules	300	40	100	160	10	2	—	—
chips	1200	160	400	640	40	8	4	—
channels	153600	20480	51200	81920	5120	1024	512	128
sensors	600	80	200	320	20	4	2	—
strips	307200	40960	102400	163840	10240	2048	1024	256

Table B.2: **Numbers of BMVD components**
Sensors and strips do not belong to the MVD numbering scheme.

in	**FMVD**	**W**	**M**	**H**	**X**
wheels	4	—	—	—	—
modules	56	14	—	—	—
half-modules	112	28	2	—	—
chips	448	112	8	4	—
channels	57244	14336	1024	512	128
sensors	112	28	2	1	—
strips	53760	13440	960	480	128(96)

Table B.3: **Numbers of FMVD components**
Sensors and strips do not belong to the MVD numbering scheme.

B.2 Results from Electrical Measurements on MVD Sensors

Measured property	Symbol	Value
built-in potential	V_{bi}	0.7 V
unbiased width of depletion region	$d(V_{bi})$	34 μm
depletion voltage	V_{depl}	65 V
total leakage current	I_{leak}	≤ 100 nA
effective doping concentration of n-material	N_{eff}	$7.9 \cdot 10^{11}$ cm^{-3}
resistivity of n-material	ρ	5.3 kΩcm
effective doping concentration of p^+-material	N_A	$5.8 \cdot 10^{19}$ cm^{-3}
resistance of p^+-strips	$R_{p^+,14\mu m}$	90 kΩcm^{-1}
	$R_{p^+,12\mu m}$	100 kΩcm^{-1}
coupling capacitance	C_c	26.2 pFcm^{-1}
interstrip capacitance	$C_{i,14\mu m}$	1.07 pFcm^{-1}
	$C_{i,12\mu m}$	0.93 pFcm^{-1}
strip-to-backplane capacitance	C_b	0.073 pFcm^{-1}

Table B.4: **Results from electrical measurements on MVD sensors** [7], [16]

B.3 Readout Chip HELIX128-3.0

Property	Value
process	AMS 0.8 μm
radiation hard	400 kRad
channels	128
max. latency	≤ 128
derandomiser	8
deadtimeless	yes
samp. clock	10.4 MHz
R/O clock	≤ 40 MHz
daisy chainable	failsafe
peak mode	yes
deconvolution	no
front-end type	CMOS
signal polarity	both
peaking time	45 ns
fall time	≤ 100 ns
gain	≈ 67 μA fC^{-1}
dyn. range	-40...+40 fC
ENC	$396\,e^- + 39.4\,e^-$ pF^{-1}
program-IF	serial, wo
power cons.	≈ 2 mW channel^{-1}
dimensions $w \times l$	6.4×14 mm^2

Table B.5: **Technical data of the readout chip HELIX128-3.0** [9]

B.4 The MVD DAQ

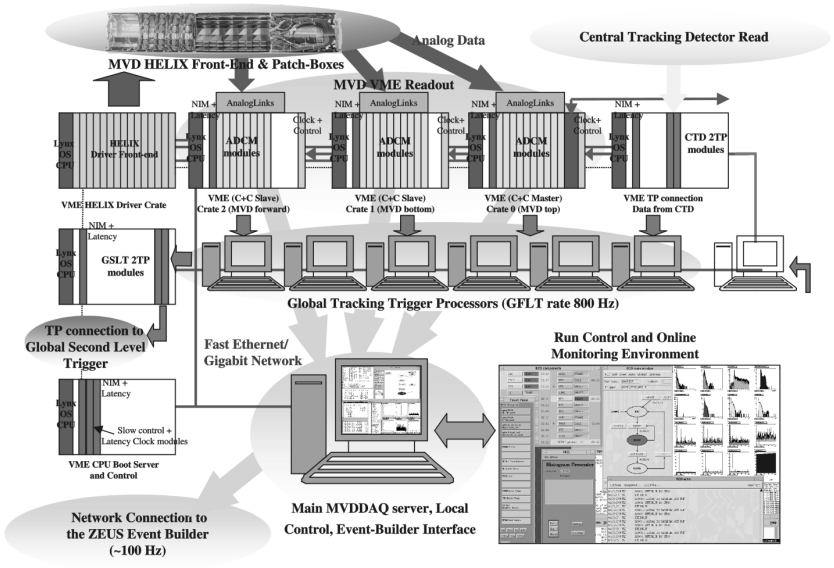

Figure B.1: **The final MVD DAQ connection scheme within the ZEUS environment**
Both signals from the GTT and from MVD itself are computed with the DAQ components portrayed here. (Picture kindly provided by A. Polini.)

Appendix C

File Lists

C.1 System Test Calibration Files

The calibration files are found on the MVD DAQ server `mvddaq.desy.de` in the directory `mvddaq@mvddaq:/conf/Calib/` in subdirectories named like `[run ID].[events]`, where `run ID` represents an internal serial numbering of runs, and `events` is the number of events processed during this run. Inside these subdirectories, the calibration files are found as `ped.load` for the pedestal files, and as `thr.load` for the threshold files, e.g.:

```
mvddaq@mvddaq:/conf/Calib/5285.106/ped.load
```

for the pedestal file created in run 5285 from 106 events. Tbl. C.1 lists all calibration runs used in this analysis.

Run ID	Events	V_{bias}	Date	Time	Masked				
					C0 L3 M0	C2 L2 M4	C2 L4 M3	C2 L5 M0 H1	C2 L15 M4
≥ 5000	≥ 100								
5035	129	70V	07.03.01	00:25		×	×	×	×
5041	115	65V	07.03.01	03:06		×	×	×	×
5044	129	60V	07.03.01	04:05		×	×	×	×
5047	106	55V	07.03.01	04:56		×	×	×	×
5050	104	50V	07.03.01	05:45		×	×	×	×
5053	102	75V	07.03.01	06:35		×	×	×	×
5057	295	70V	07.03.01	08:02		×	×	×	×
5065	230	70V	07.03.01	11:47		×	×	×	×
5159	122	75V	08.03.01	20:33	×	×	×	×	×
5177	220	75V	09.03.01	11:51	×	×	×	×	×
5241	239	70V	10.03.01	07:30	×	×	×	×	×
5246	391	80V	10.03.01	11:15		×	×	×	×
5262	351	70V	11.03.01	08:00		×	×	×	×
5269	225	70V	11.03.01	20:07		×	×	×	×
5273	205	75V	12.03.01	01:01		×	×	×	×
5281	116	75V	12.03.01	08:03		×	×	×	×
5285	106	75V	12.03.01	13:01		×	×	×	
5288	101	50V	12.03.01	15:51		×	×	×	

Run ID	Events	V_{bias}	Date	Time	Masked				
					C0 L3 M0	C2 L2 M4	C2 L4 M3	C2 L5 M0 H1	C2 L15 M4
≥ 5000	≥ 100								
5290	104	55V	12.03.01	16:47		×	×	×	
5292	105	60V	12.03.01	17:40		×	×	×	
5294	250	65V	12.03.01	18:44		×	×	×	
5297	106	70V	12.03.01	20:58		×	×	×	
5301	102	75V	12.03.01	22:07		×	×	×	
5303	192	70V	13.03.01	01:54		×	×	×	
5318	184	70V	13.03.01	22:04		×	×	×	
5372	211	`new`	14.03.01	19:32		×	×	×	
5389	142	`new`	15.03.01	09:35		×	×	×	
5399	271	`new`	15.03.01	15:38		×	×	×	
5412	190	`new`	15.03.01	23:46		×	×	×	×
5422	202	`stable0`	16.03.01	16:01		×	×	×	×
5426	203	`stable0`	16.03.01	22:34		×	×	×	×
5433	193	`stable0`	17.03.01	11:07		×	×	×	×
5435	205	`stable1`	17.03.01	15:38		×	×	×	×
5439	201	`stable1`	17.03.01	20:02		×	×	×	×
5443	286	`stable1`	18.03.01	00:13		×	×	×	×
5452	291	`stable2`	19.03.01	08:23		×	×	×	×
5456	108	`stable2`	19.03.01	16:49		×	×	×	×
5462	187	`stable2`	20.03.01	02:56		×	×	×	×
5467	127	`stable2`	20.03.01	12:36		×	×	×	×

Table C.1: **List of calibration runs**
These are the used runs for the stability analysis described in section 5.3. The output from every run are the two calibration files `ped.load` and `thr.load`.
The entries `new`, `stable0`, `stable1` and `stable2` for V_{bias} describe bias voltage settings, which are adjusted individually to the depletion voltages of the half-modules, where `new` is the first attempt, and `stable2` is the latest and most reliable upgrade of these settings.

C.2 System Test Data Files

The system test data files, which are files of EVB-format, are found on the ZEUS data disk cluster "`doener`" in the directory `/shift/doener/data121/zeus/zsitest/`, then in the subdirectories `fullmvd/`, `fullmvd2/` or `fullmvd3/`. Therein they are named like `MVD.D[date].T00[time].R00[run ID]A.evb`, where `[date]` and `[time]` represent date and time of storage, and `[run ID]` is the numbering of runs, e.g.: `/shift/doener/data121/zeus/zsitest/fullmvd3/MVD.D010322.T001700.R005463A.evb`. Tbl. C.2 lists all cosmic data runs used in this analysis.

Run ID	Events	Date	Calibration Run ID
bias voltage setting: `stable1`			
5434	40026	17.03.01	5426
5438	40000	17.03.01	5435
5442	37053	17.03.01	5439
5444	46272	18.03.01	5443
5445	45xxx	18.03.01	5443
5446	42076	18.03.01	5443
5447	42427	18.03.01	5443
5448	43345	18.03.01	5443
5449	42002	18.03.01	5443
5450	42004	19.03.01	5443
5451	14692	19.03.01	5443
bias voltage setting: `stable2`			
5453	41079	19.03.01	5452
5454	31707	19.03.01	5452
5458	11479	19.03.01	5456
5459	xxxxx	19.03.01	5456
5460	xxxxx	19.03.01	5456
5461	40229	19.03.01	5456
5463	40044	20.03.01	5456
5464	40003	20.03.01	5456
5466	xxxxx	20.03.01	xxxx
5468	37372	20.03.01	5467
5473	40063	20.03.01	5467
5474	xxxxx	20.03.01	5467
Sum:	$\gtrsim 800000$		

Table C.2: **List of cosmic runs under bias voltage settings `stable1` and `stable2`**
These are the underlying runs for the digitisation analysis in section 6.3.

Appendix D

Results of Analyses

D.1 Results of the Analyses of the Calibration Parameters

D.1.1 Unstable Calibration Parameters

The channels with unstable calibration parameters listed here have been found by analysing the calibration runs with the bias voltage setting `stable2`. A more complete list from analysing all calibration runs, comments included, is provided in the MVD data base [11].

Cylinder	Ladder	Module	Half-Module	Chip	Channel
0	0	2	0	2	63
0	1	1	0	0	29
					30
					31
0	3	1	1	3	54
1	0	3	0	2	105
					106
					107
					108
1	1	0	1	1	56
1	1	0	1	2	15
					16
1	3	2	0	3	87
1	4	4	1	0	5
					6
1	6	2	0	2	31
1	7	1	1	1	43
					44
1	7	2	0	2	27
					28
1	7	3	0	1	89
					90
1	8	4	1	1	111
					112

Cylinder	Ladder	Module	Half-Module	Chip	Channel
					113
1	9	4	1	1	126
					127
2	0	1	0	0	114
2	2	0	1	2	13
2	2	1	0	1	79
					80
2	2	2	0	0	29
					30
2	3	0	1	0	69
2	5	2	0	2	7
2	5	4	0	1	23
2	7	0	1	1	27
					28
2	8	3	0	0	71
					72
2	10	3	1	2	103
					104
					105
2	12	3	1	2	31
2	13	0	0	3	54
2	13	2	1	3	41
2	14	1	0	0	74
2	15	1	0	1	86
					87

Table D.1: **List of channels with unstable calibration parameters in BMVD**
This list is based on the runs with the optimised bias voltage setting `stable2`

Wheel	Module	Half-Module	Chip	Channel
0	4	0	1	18
0	8	0	3	14
				15
1	2	0	2	57
1	13	1	0	69
				70
2	0	0	0	89
				90
				91
				92
2	5	0	0	61
				62

Wheel	Module	Half-Module	Chip	Channel
2	11	0	1	89
2	11	1	0	73
				74
3	1	1	0	3
				4
3	4	0	1	116
3	8	0	2	21
				22
				(23)
				24
3	13	0	2	7
				8
				9

Table D.2: **List of channels with unstable calibration parameters in FMVD**
This list is based on the runs with the optimised bias voltage setting `stable2`.

D.2 Results of the Analyses of the System Test Data

D.2.1 Comparison of Sensor Types

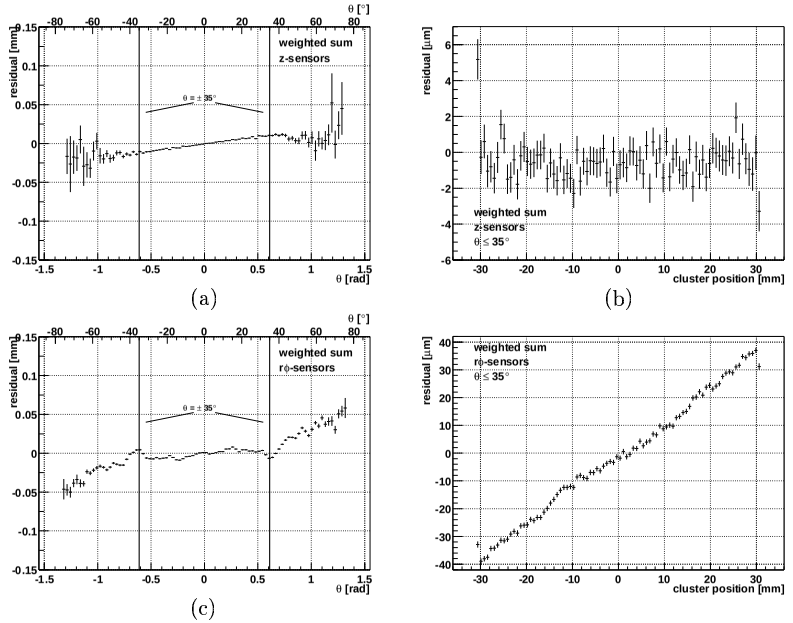

Figure D.1: **Comparison of residuals measured in the z- and ϕ-sensors (centre-of-gravity-algorithm)**
Residual as a function of the incidence angle on the x-z-plane for (a) the z-sensors and (c) the *phi*-sensors and residual as a function of the calculated cluster position on the sensor for (b) the z-sensors and (d) the *phi*-sensors.
Cluster positions are calculated by the centre-of-gravity-algorithm.

D.2.2 Comparison of Position Reconstruction Algorithms

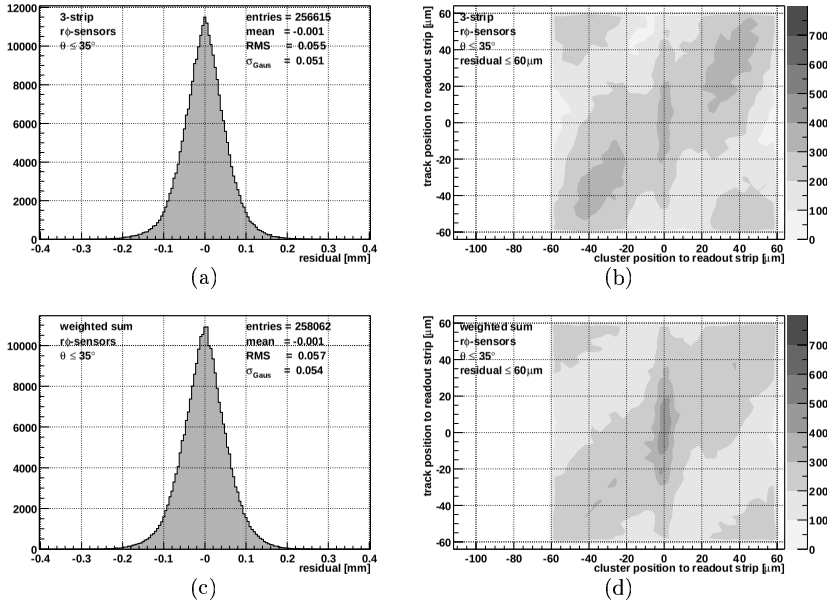

Figure D.2: **Comparison of the residual distribution and the correlations of the calculated cluster position and track position obtained for 3-strip- and centre-of-gravity-algorithm (ϕ-sensors)**
Distributions of residuals for (a) the 3-strip-algorithm and (c) the centre-of-gravity-algorithm and calculated position of the particle track relative to the next readout strip as a function of the calculated cluster position relative to the next readout strip for (b) the 3-strip-algorithm and (d) the centre-of-gravity-algorithm.

D.2.3 Extraction of Transfer Coefficients from System Test Data

The following three figures(Figs. D.3 - D.5) show distributions of normalised signal heights on readout strips without noise suppression for different calculated positions of the particle track with respect to the readout strip. For histogram 0, the particle track crosses the readout strip itself, for histogram 1 the next intermediate strip etc., for histogram 6 the next readout strip etc.

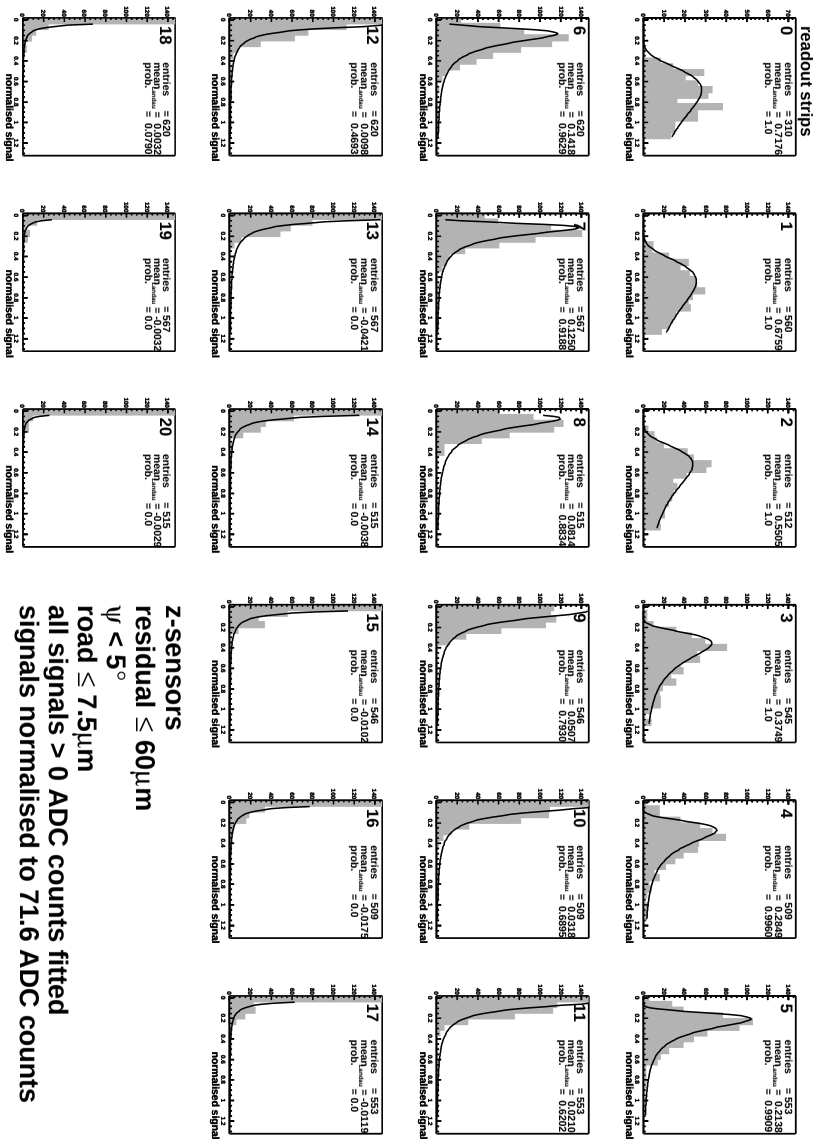

Figure D.3: **Example of the normalised signal distributions, from which the transfer coefficients are obtained (a)**
In this example, a fit to histograms with a coarse binning including noise is shown.

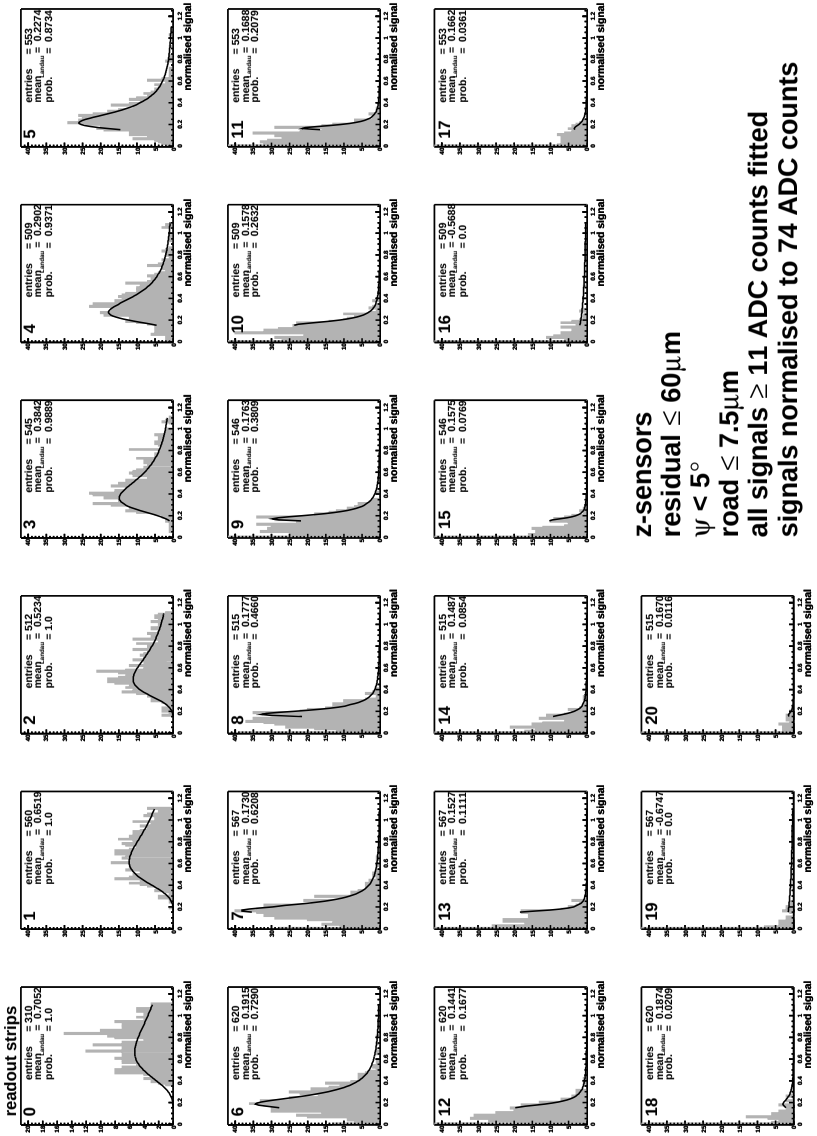

Figure D.4: **Example of the normalised signal distributions, from which the transfer coefficients are obtained (b)**
In this example, a fit to histograms with a fine binning excluding noise is shown.

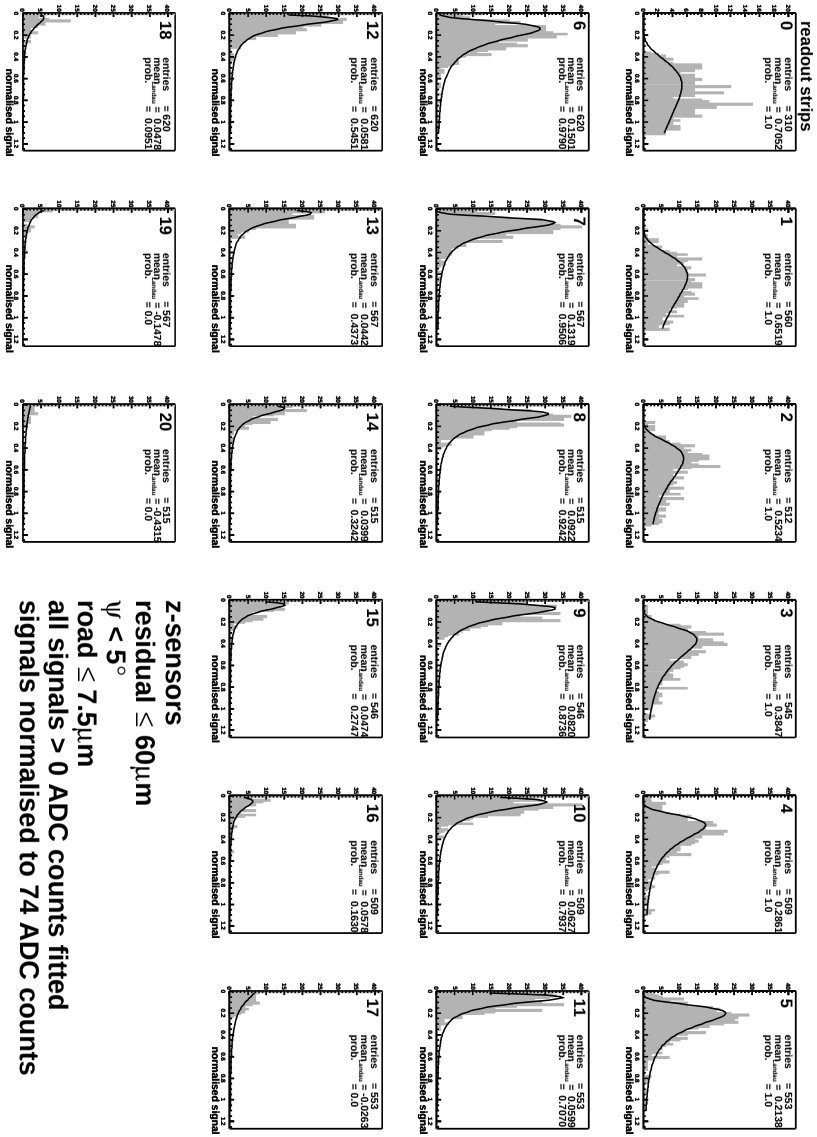

Figure D.5: **Example of the normalised signal distributions, from which the transfer coefficients are obtained (c)**
In this example, a fit to histograms with a fine binning including noise is shown.

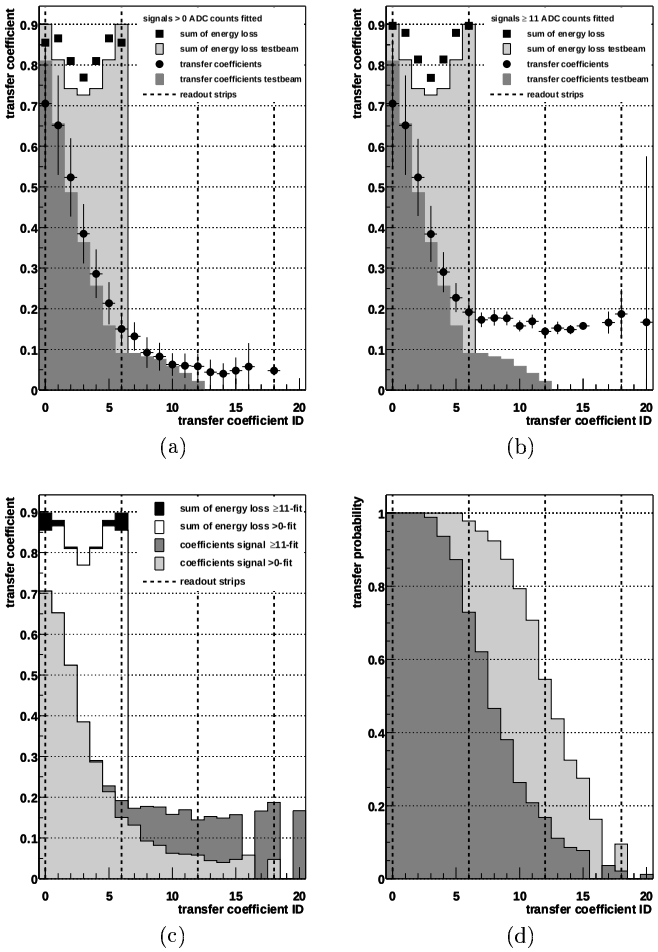

Figure D.6: **Example of resulting transfer coefficients**
(a), (b) Transfer coefficients and their sum for the readout strips next to the calculated position of the particle track on both sides (energy loss) for a fit (a) including noise and (b) excluding noise. Both are compared to the results from test beam measurements.
(c) Comparison of (a) and (b).
(d) Comparison of corresponding transfer probabilities.
In this example, transfer coefficients and probabilities shown in Figs. D.4 and D.5 (fits to histograms with fine binning) are compared.

D.3 Results of the Analyses of the Cluster Simulation

D.3.1 Simulations with Test beam Transfer Coefficients

All figures show distributions of (a) the maximum signal height in the cluster, (b) all signal heights in the cluster, (c) the sum of all signal heights in cluster and (d) the cluster size. Transfer coefficients extracted from test beam data are used for the simulation. Transfer probabilities are not available here.

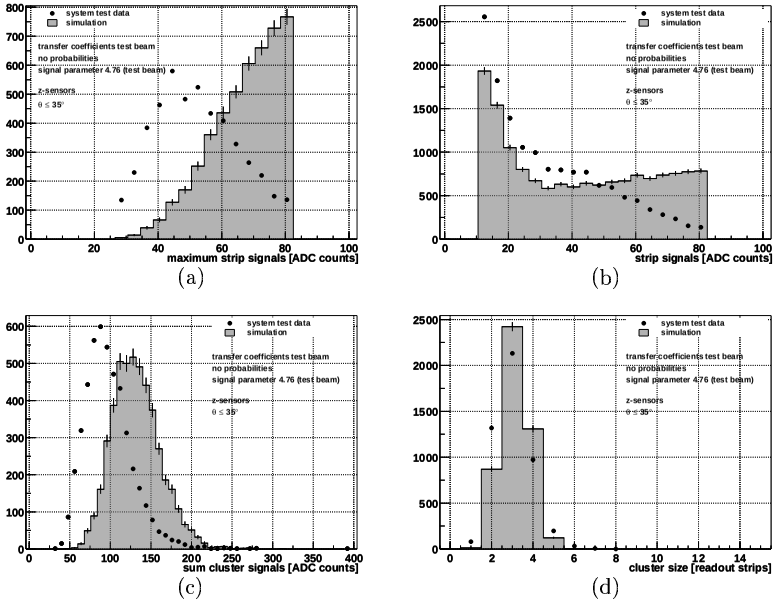

Figure D.7: **Simulated cluster shapes using the test beam simulation scenario**
Here the general signal height extracted from test beam data is used.

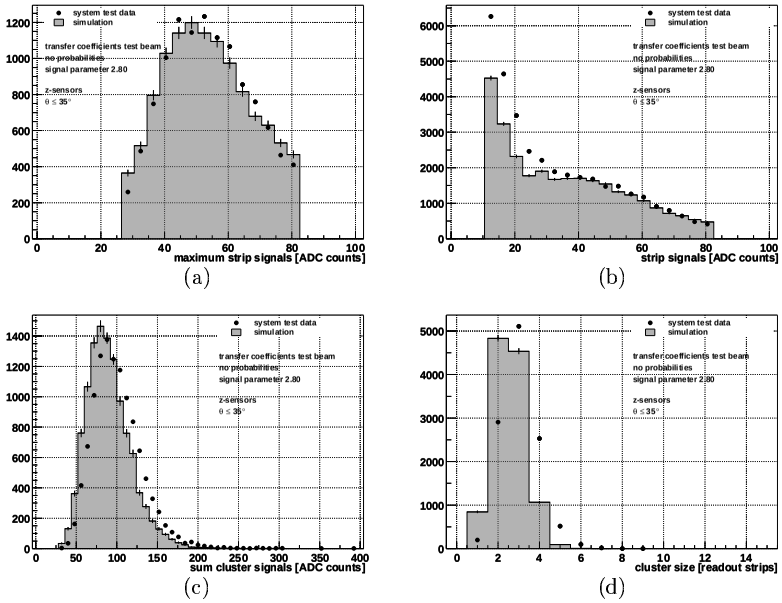

Figure D.8: **Simulated cluster shapes using the test beam simulation scenario, but adjusted signal height**
Here the general signal height has been adjusted to the maximum signal height in the cluster. It amounts to 59% of the general signal height extracted from the test beam data.

D.3.2 Simulations with Different Simulation Scenarios

The different correspond to variations of the binning of the fitted histograms and the fitting range, when extracting the transfer coefficients, and by applying or not applying the extracted transfer probabilities.

D.3.2.1 The Cluster Shapes

All figures show distributions of (a) the maximum signal height in the cluster, (b) all signal heights in the cluster, (c) the sum of the signal heights in cluster and (d) the cluster size.

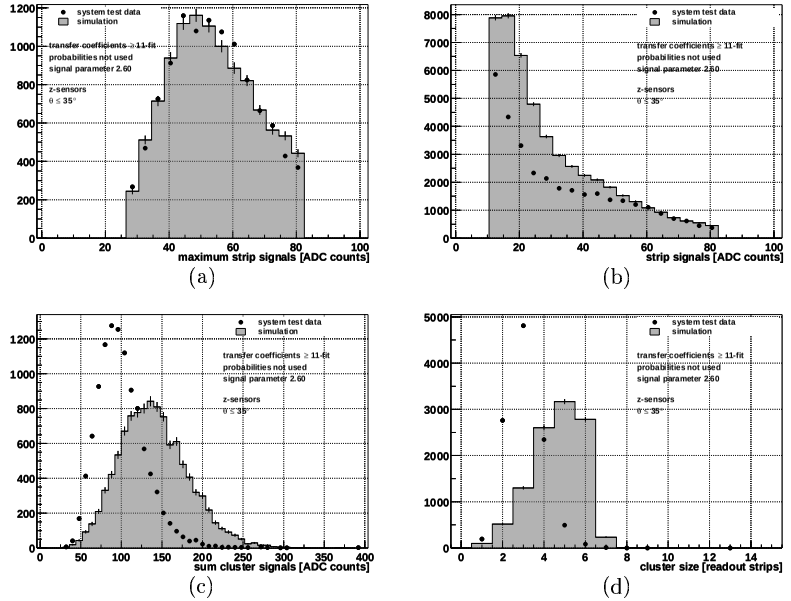

Figure D.9: **Simulated cluster shapes (a)**
In this example, only the transfer coefficients from a fit to histograms with coarse binning excluding noise have been used.

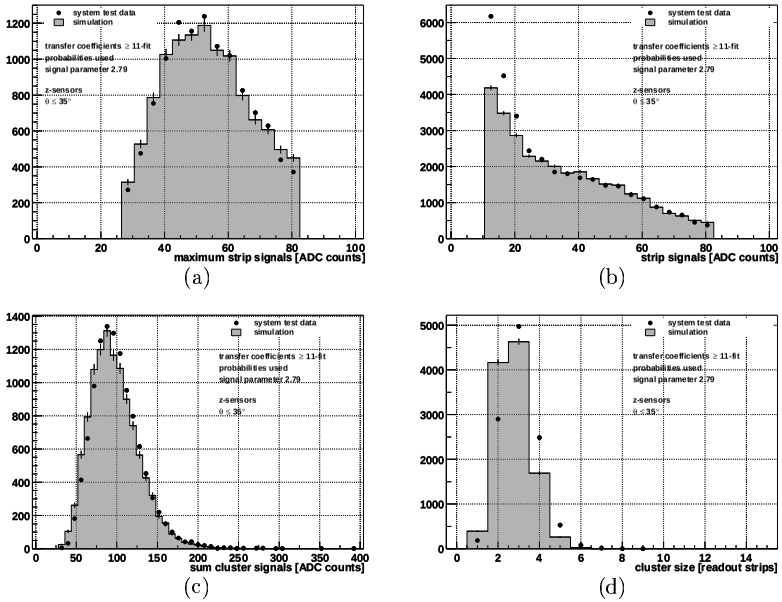

Figure D.10: **Simulated cluster shapes (b)**
In this example, the transfer coefficients and probabilities from a fit to histograms with coarse binning excluding noise have been used.

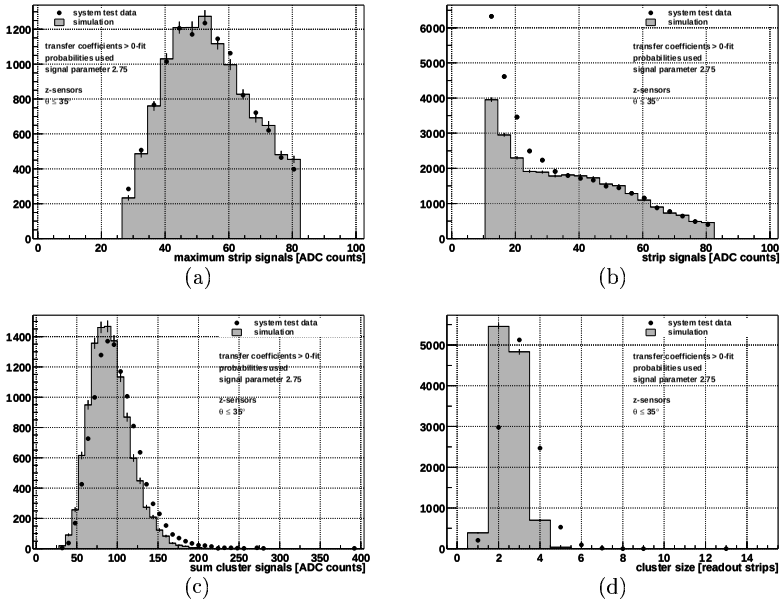

Figure D.11: **Simulated cluster shapes (c)**
In this example, the transfer coefficients and probabilities from a fit to histograms with coarse binning including noise have been used.

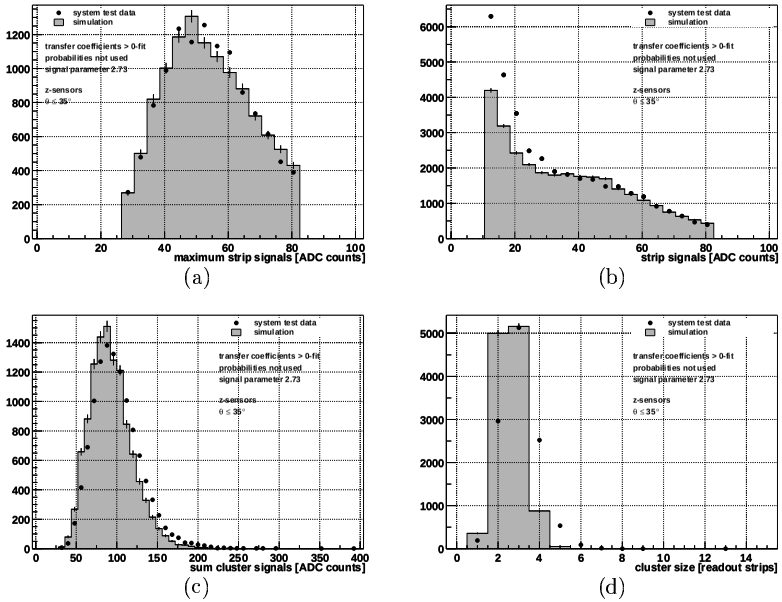

Figure D.12: **Simulated cluster shapes (d)**
In this example, only the transfer coefficients from a fit to histograms with coarse binning including noise have been used.

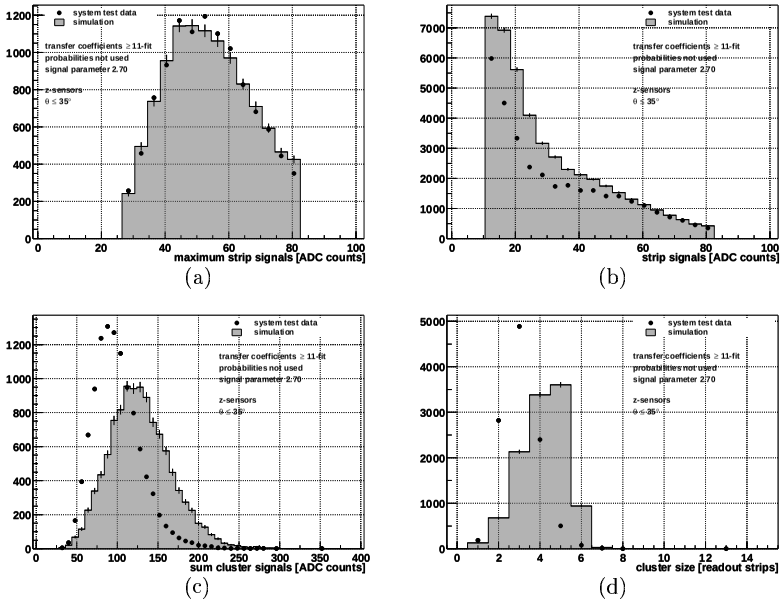

Figure D.13: **Simulated cluster shapes (e)**
In this example, only the transfer coefficients from a fit to histograms with fine binning excluding noise have been used.

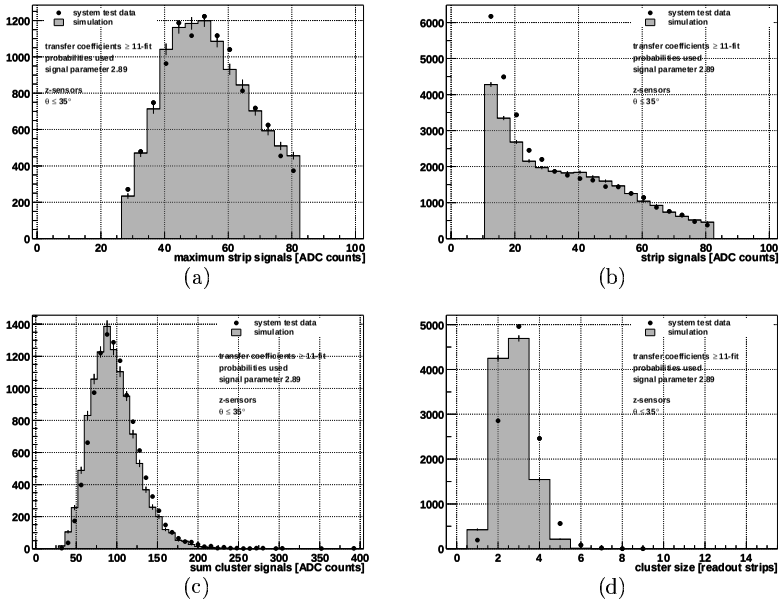

Figure D.14: **Simulated cluster shapes (f)**
In this example, the transfer coefficients and probabilities from a fit to histograms with fine binning excluding noise have been used.

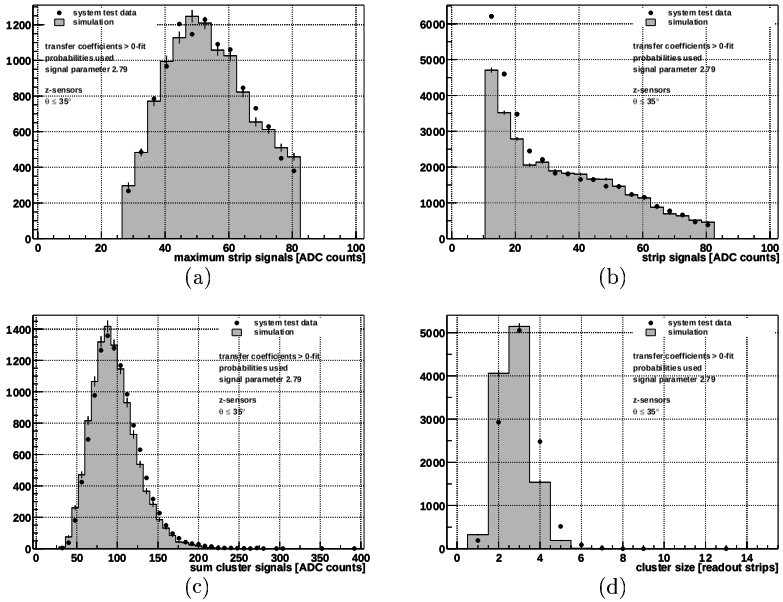

Figure D.15: **Simulated cluster shapes (g)**
In this example, the transfer coefficients and probabilities from a fit to histograms with fine binning including noise have been used.

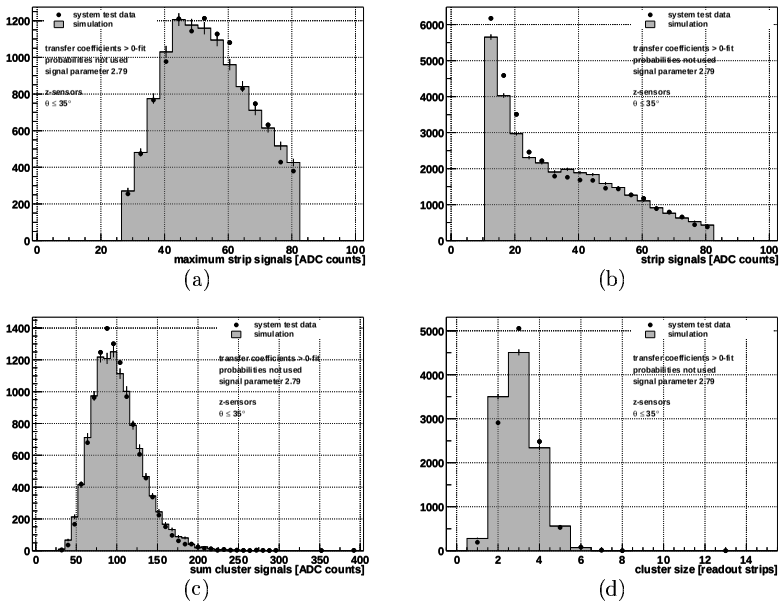

Figure D.16: **Simulated cluster shapes (h)**
In this example, only the transfer coefficients from a fit to histograms with fine binning including noise have been used.

D.3.2.2 Analyses of Simulated Cluster Data

The following three figures (Figs. D.17 - D.19) show distributions of the signal heights. Strip No. 0 is the readout strip closest to the calculated cluster position, Strip No. 1 the next next neighbour etc. The numbering (d, f, h) refers to the related figures in section D.3.2.1.

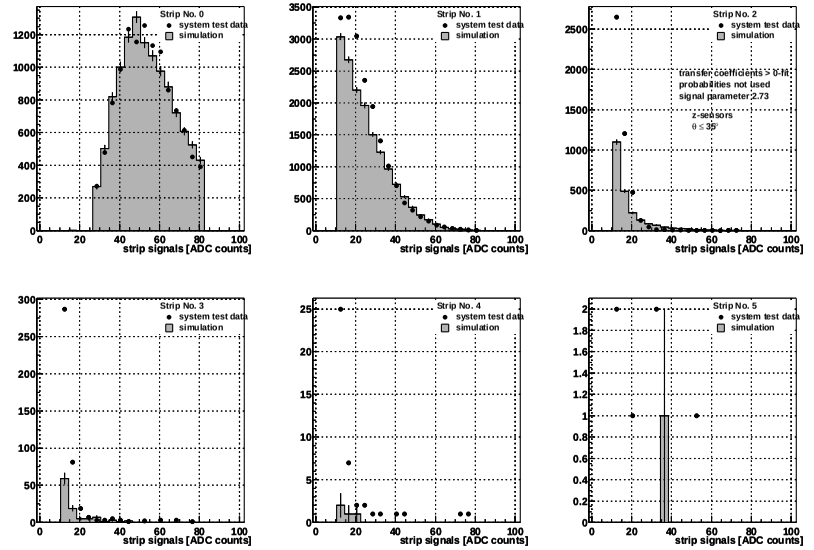

Figure D.17: **Example of signal heights separated by the distance from the calculated cluster position (d)**
In this example, only the transfer coefficients from a fit to histograms with coarse binning including noise have been used (v. Fig. D.12).

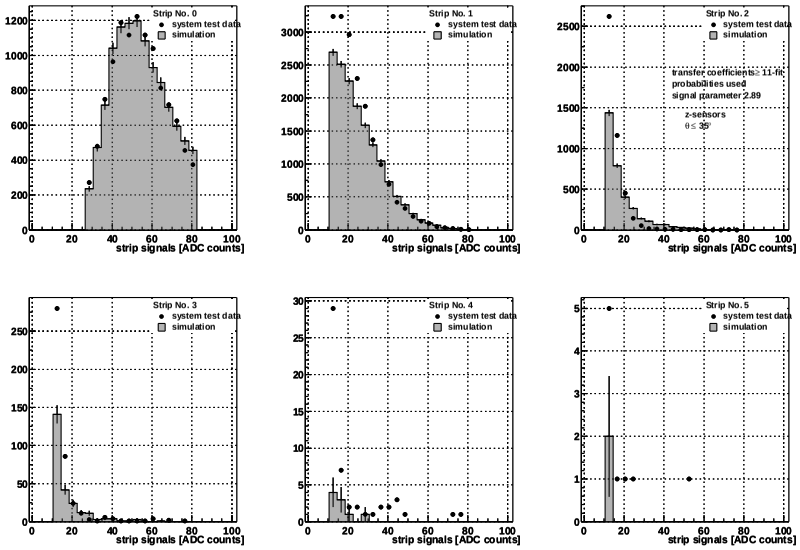

Figure D.18: **Example of signal heights separated by the distance from the calculated cluster position (f)**
In this example, the transfer coefficients and probabilities from a fit to histograms with fine binning excluding noise have been used (v. Fig. D.14).

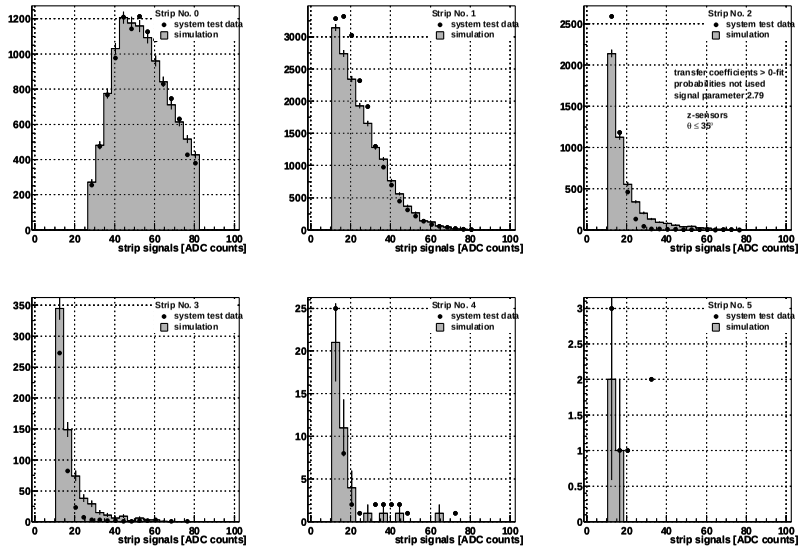

Figure D.19: **Example of signal heights separated by the distance from the calculated cluster position (h);**
In this example, only the transfer coefficients from a fit to histograms with fine binning including noise have been used (v. Fig. D.16).

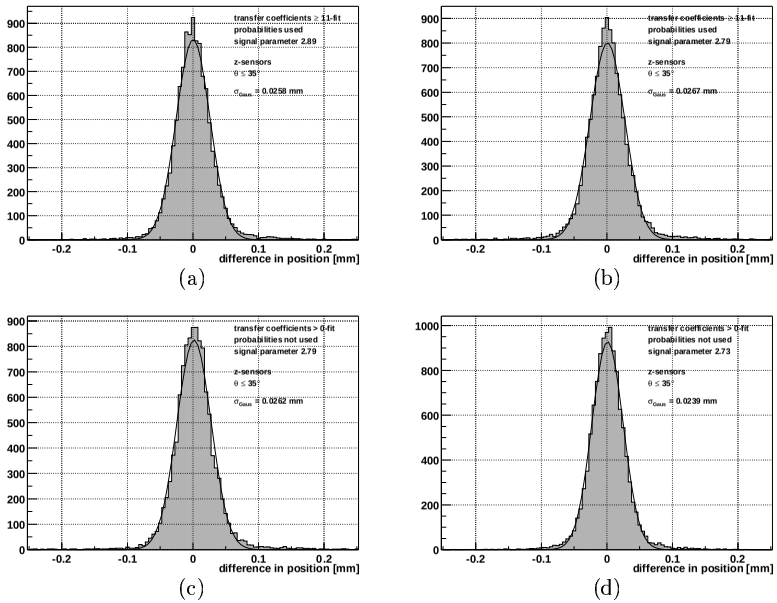

Figure D.20: **Examples of the resolution of the cluster simulation**
Distributions of the distances of the calculated simulated cluster positions from the true position, fitted with a Gaussian. The resolutions of the simulations is given by the standard error of the Gaussians σ_{Gaus}.
In this examples, the transfer coefficients and probabilities from a fit to histograms with (a) coarse and (b) fine binning excluding noise and only the transfer coefficients from a fit to histograms with (a) coarse and (b) fine binning including noise have been used.

List of Figures

List of Tables

Bibliography

[1] G. Bashindzhagyan, N. Korotkova: **Simulation of Silicon Microstrip Detector Resolution for ZEUS Vertex Upgrade**, ZEUS-99-023, Hamburg, 1999.

[2] V. Blobel, E. Lohrmann: **Statistische und numerische Methoden der Datenanalyse**, ISBN 3-519-03243-0, *Teubner*, 1998.

[3] I. Bloch: **The ZEUS Micro-Vertex Detector System Test – Triggering and Data Analysis**, Diploma Thesis, DESY-THESIS-2002-001 Universität Hamburg, 2001.

[4] R. Carlin, private communication, Hamburg, 2001.

[5] V. Chiochia: **The ZEUS Micro Vertex Detector**, proceedings on the 10^{th} International Workshop on Vertex Detectors (VERTEX 2001), Brunnen (CH), September 23^{rd} - 28^{th}, 2001, to be published in *Nucl. Instr. Meth.* A.

[6] V. Chiochia, private communication, Hamburg, 2001.

[7] D. Dannheim: **The Silicon Strip Detectors of the ZEUS Microvertex Detector**, Diploma Thesis, DESY-THESIS-1999-027, Universität Hamburg, 1999.

[8] W. Fallot-Burghardt et al.: **HELIX128-x User Manual, V2.1**, HD-ASIC-33-0697, Heidelberg, 1999.

[9] M. Feuerstack-Raible: **Overview of Microstrip Read-out Chips**, *Nucl. Instr. Meth.* A447(2000)35-43.

[10] T. Fusayasu: **MVD ADCM Cluster Algorithm**, `http://www-zeus.desy.de/components/mvd/electronics.html`, Hamburg, 2001.

[11] E. Gallo (ed.): **MVD Module Database**, `http://www-zeus.desy.de/~gallo/ZEUS/mysql2/output.html`, Hamburg, 2001.

[12] B. Holzer: **HERA Status 99**, presented at the ZEUS Collaboration Meeting, Hamburg, February 21. - 25., 2000.

[13] M.J. Kraan (ed.): **Mechanical Design Vertex Detector**, `http://www.nikhef.nl/pub/departments/mt/projects/zeus/vertex/website.html`, Amsterdam, 2001.

[14] G. Lutz: **Semiconductor Radiation Detectors**, ISBN 3-540-64859-3, *Springer*, 1999.

[15] E. Maddox: **MVD Track Reconstruction Page**, `http://www.nikhef.nl/~h21/reconstruct/` Amsterdam, 2001.

[16] J. Martens: **Simulationen und Qualitätssicherung der Siliziumstreifen-Detektoren des ZEUS-Mikrovertexdetektors**, Diploma Thesis, DESY-THESIS-1999-044, Universität Hamburg, 1999.

[17] M. Milite: **The Internal Structure of Charmed Jets in Photoproduction at HERA and Tests of the ZEUS Microvertex Silicon Sensors**, Ph.D. Thesis, DESY-THESIS-2001-050, Universität Hamburg, 2001.

[18] M. Moritz: **Measurement of the High Q^2 Neutral Current DIS Cross Section at HERA**, Ph.D. Thesis, Universität Hamburg, 2002, to be published.

[19] Particle Data Group: **Review of Particle Physics**, ISSN 1434-6044, *Springer*, 2000.

[20] H. Pernegger: **The Silicon Ministrip Detector of the DELPHI Very Forward Tracker**, Ph.D. Thesis, Technische Universität Wien, 1996.

[21] U. Schneekloth (ed.): **The HERA Luminosity Upgrade**, LUM-ZEUS-1998-0014, Hamburg, 1998.

[22] S. M. Sze: **Physics of Semiconductor Devices**, ISBN 0-471-05661-6, *John Wiley & Sons*, 1981.

[23] ZEUS Collaboration: **A Microvertex Detector for ZEUS**, ZEUS-97-006, Hamburg, 1997.

[24] ZEUS Collaboration: **ZEUS Tracking Software for HERA Phase II**, DESY-PRC software report, Hamburg, October 23^{rd}, 2001.

[25] ZEUS MC Group: **FUNNEL – The ZEUS MC Production Facility**, `http://www-zeus.desy.de/components/funnel/` Hamburg, 2001.

[26] ZEUS MVD Group: **Mechanical Design and Construction of the ZEUS Micro Vertex Detector**, ZEUS-00-028, Hamburg, 2000.

Acknowledgements

I would like to thank:

Prof. R. Klanner for making this thesis possible and for very many valuable hints.
Prof. K. Wick for his attendance to act as additional referee.
Dr. T. Carli as my very engaged tutor for a lot of ideas and explanations, teaching, bolstering and each other kind of support.
Prof. R. Carlin, Dr. E. Fretwurst and Dr. G. Kramberger for revising essential parts of this thesis.
Dr. A. Garfagnini, Dr. A. Geiser, Dr. F. Goebel, Dr. A. Polini, Dr. C. Youngman, V. Chiocha and D. Dannheim for many important explanations concerning the MVD and for their contributions to the software developments.
Dr. M. Melite and Dr. M. Moritz for explanations on the test beam results.
E. Maddox for his great track fit software and together with Dr. E. Koffeman for improving the MVD geometry so quickly on request.
Dr. B. Surrow for his idea to study the stability of the MVD calibration parameters.
The whole ZEUS MVD group for support and fruitful discussions.
I. Bloch for high-producing teamwork and many, many help.
O. Gutsche for computing support.
The whole "Arbeitsbereich Nukleare Messtechnik" for the wonderful working atmosphere, especially P. Verstegen for catering for enough coffee and P. Buhmann for the *non-physical* conversations.
S. Schulz for providing her apartment (and for waiving a rent).
My family and friends for their interest and for keeping me grounded.

Especially I would like to thank my wife Birgit for her affectionate support and patience.

Ganz besonders möchte ich meiner Frau Birgit für ihre liebevolle Unterstützung und Geduld danken.

This diploma thesis is devoted to Lucas, who learned speaking during its becoming.

Diese Diplomarbeit ist Lucas gewidmet, der während ihres Entstehens Sprechen lernte.

Erklärung

Hiermit erkläre ich, die vorliegende Arbeit unter Angabe aller verwendeten Quellen und Hilfsmittel selbstständig angefertigt zu haben.

Hamburg, 12. Februar 2002

(Volker Adler)